Ice Roughness Estimation via Remotely Piloted Aircraft and Photogrammetry

by
James K. Ehrman

A Thesis submitted to the Faculty of Graduate Studies of
The University of Manitoba
in partial fulfillment of the requirements of the degree of

MASTER OF SCIENCE

Department of Civil Engineering
University of Manitoba
Winnipeg

Abstract

Photogrammetry conducted with images obtained via Remotely Piloted Aircraft (RPA) has revolutionized the field of land surface monitoring. It is particularly useful where land surface data collection would otherwise be expensive or dangerous. The monitoring of fluvial ice covers can be time-intensive, dangerous, and costly. Fluvial ice roughness is a sensitive parameter in hydraulic models and is difficult to measure using traditional field methods. This research hypothesizes that the surface roughness of a fluvial ice cover is indicative of subsurface roughness. The hypothesis was tested through a comparison of ice roughness determined through inverse hydraulic modeling and ice roughness determined through statistical analysis of ice surfaces derived through RPA-photogrammetry. Hydraulic and topographic data were collected over two years of field research on the Dauphin River in Manitoba, Canada. Various statistical metrics were used to represent the roughness of the surfaces. Strong correlation was identified in the comparison of ice cover roughness determined through RPA-photogrammetry and roughness calculated via the Nezhikhovskiy equation, as well as ice thickness. Some correlation was observed between ice cover roughness observed through RPA-photogrammetry and ice roughness predicted through inverse hydraulic modeling. The inter-quartile range (IQR) was the most representative roughness metric. The maximum peak value performed better in some cases, but this metric would be heavily influenced by outliers, and was rejected as a representative metric. Three distinct forms of surface ice roughness were noted: rough, smooth, and ridged. Statistical properties of elevation data of fluvial ice covers were calculated, none were found to be normally distributed. K-means clustering analysis was used to group cover into two categories, which were interpreted as rough and smooth ice. The IQR of the rough and smooth categories were 0.07 - 0.12 m and 0.01 - 0.05 m, respectively. RPA-photogrammetry was concluded to be a suitable method for monitoring of fluvial ice covers, but more research is needed to confirm that surface ice cover roughness observed through this method is directly applicable to hydraulic modeling. Other applications of RPA-photogrammetry for the characterization of fluvial ice covers are proposed.

Acknowledgments

The author would like to acknowledge that the majority of the field data was collected on the lands of the Zaaskajiwaning Peoples, the Dauphin River First Nation, under Treaty 2.

Field testing of the methodology described herein was conducted with the greatly appreciated permission of the owners of River's Edge Nursery in La Barriere, Manitoba.

The subsequent research was greatly aided through the technical guidance of Dr. Shawn Clark, Dr. Masoud Asadzadeh, and Dr. Ahmed Shalaby. Field activities were managed and conducted in part by Alex Wall and the author, with the assistance of Dr. Shawn Clark, Dr. Lucas Wazney, Dr. Vincent McFarlane, and Eric Schillberg. Finally, financial support provided by Manitoba Hydro and the National Science and Engineering Research Council was instrumental in acquiring the required instrumentation for this research project.

Table of Contents

List of Tables

List of Figures

1 Introduction

1.1 Motivation

The consequences of ice on the flow regimes of rivers in cold climates can be dramatic, sometimes leading to loss of life and damage to infrastructure. In-stream infrastructure such as bridge piers, hydraulic control structures, and hydro-electric generating stations are subject to immense forces due to river ice, which is a critical factor in the design of such structures. At first consideration, climate change could result in a reduced risk of ice impacts on fluvial infrastructure due to anticipated warming. Yet, what is being observed is unprecedented temperature and precipitation variability (MacDonald et al., 2018), which in some cases can produce multiple fluvial freeze-up and break-up events in a single year (Beltaos, 2002). The flow and temperature conditions during freeze-up greatly impact the final thickness and roughness of a fluvial ice cover and thus the hydraulic consequences. The effects of changes to the expected annual patterns of temperature and precipitation remain to be seen but provides impetus for further study of the hydraulic impacts of ice covers and jams.

Understanding fluvial ice roughness is a critical step in better understanding the evolution and hydraulic impacts of fluvial ice covers. Currently, ice roughness is either estimated through empirical means, such as the Nezhikhovskiy (1964) equation, or through complex and expensive methods, such as physical or numerical hydraulic modeling. Manual measurements can also be made as in Buffin-Belanger et al. (2015); Crance and Frothingham (2008), or roughness can be inferred from a measured velocity profile as in Gerard and Andres (1984). However, these direct measurement methods require personnel to conduct work on ice covers, which are frequently unsafe, and limits the types of ice covers that can be studied.

An obvious solution to studying ice covers in a safe environment is through the use of aerial vehicles. Helicopters, small fixed-wing aircraft, and satellites have long been used for the study of earth surface phenomena. All are prohibitively expensive to be solely dedicated to the study of ice covers, and none can produce images of sufficient resolution for surface roughness studies. Recently, Remotely Piloted Aircraft (RPA) have become much more accessible, inexpensive, and reliable. Coupled with high-resolution image-stabilized digital cameras, they offer the opportunity to document and study otherwise inaccessible areas at a fraction of the cost of any other method.

The following sections seek to introduce the research objectives of this thesis, followed by a relevant summary of the subjects of hydraulic roughness, fluvial ice cover formation, the use of RPAs for the study or surface roughness, and the characterization of roughness parameters.

1.2 Study Location

The Dauphin River drains lake St. Martin into Lake Winnipeg through 52 kilometers (km) of channel. It is located approximately 250 km North of the city of Winnipeg, in Manitoba, Canada, as shown in Figure 1.1. The channel has steep, shallow banks, that range between 110 - 160 meters (m) wide. The surficial geology of the area is composed of glacial till with erratics, boulders, cobbles, and gravels observed throughout the channel. The most upstream 40 km of channel has a mild slope (0.029%) and is meandering, it will henceforth be referred to as the “Upper Dauphin River". The bed composition of the Upper Dauphin River was observed to be primarily silt. The most downstream 12 km of channel transitions into a well-defined riffle-pool system with a relatively higher slope (0.16%). This reach will henceforth be referred to as the “Lower Dauphin River". Riffle sections in the Lower Dauphin River were observed to have a gravel bed with some boulders and erratics. Pool sections were observed to be silt bottomed. A profile of the bed of the Lower Dauphin River is presented in Figure 1.2, along with the locations of the applicable study

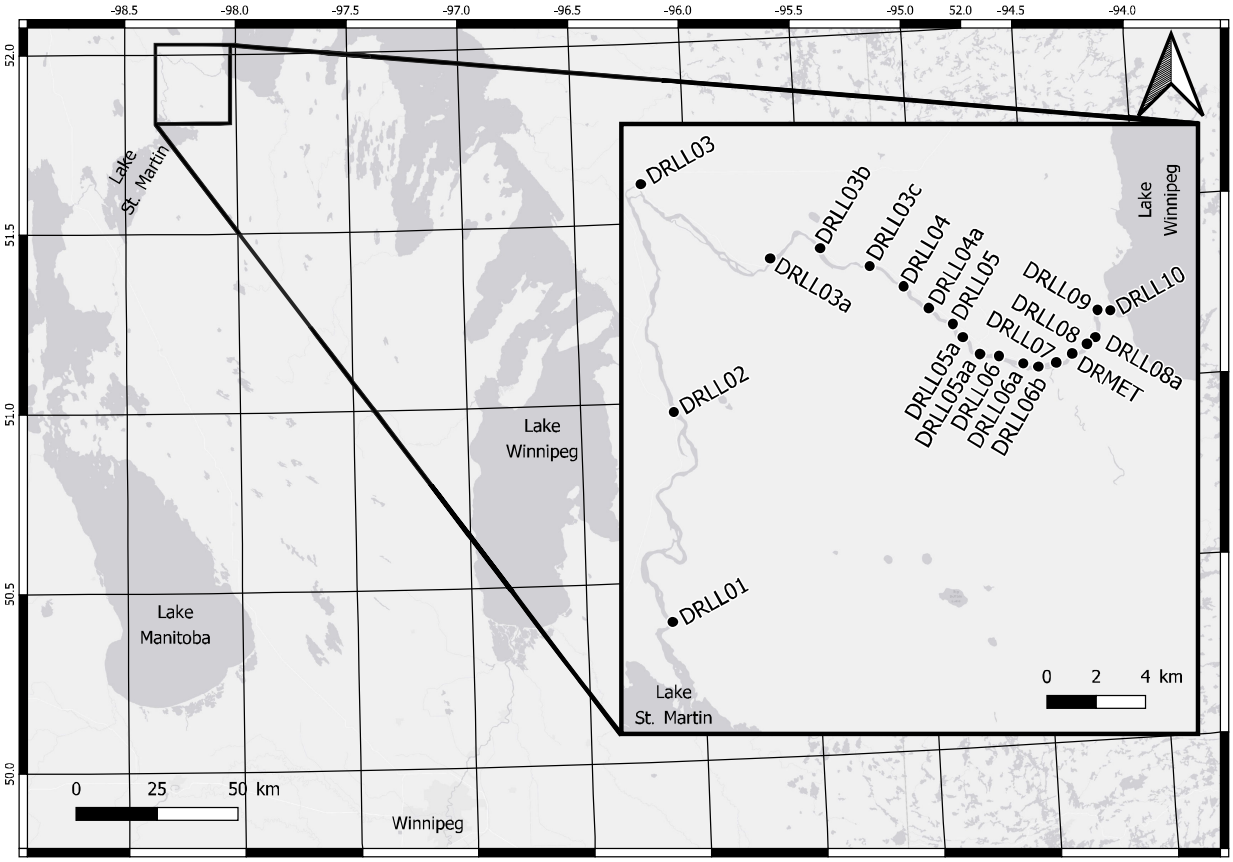

Figure 1.1: Key map of study location

sites. During winter ice formation, dramatic ice consolidation events, jams, and flooding have been reported by Wazney et al. (2018) on the Lower Dauphin River. Lake Winnipeg water levels can have a significant effect on the most downstream 2 km of this reach; this was typically where the largest toe of the ice jam would form.

Table 1.1 outlines the daily maximum and minimum recorded temperatures and wind velocity, averaged over each month for the five years that the site has been operational. All weather data were collected remotely by an established weather station operated by the University of Manitoba, located at 51°56’ 44.67” N, 98°4’ 57.53” W.

A Water Survey of Canada (WSC) gauge station (05LM006) is located $\approx$ 100 m downstream of

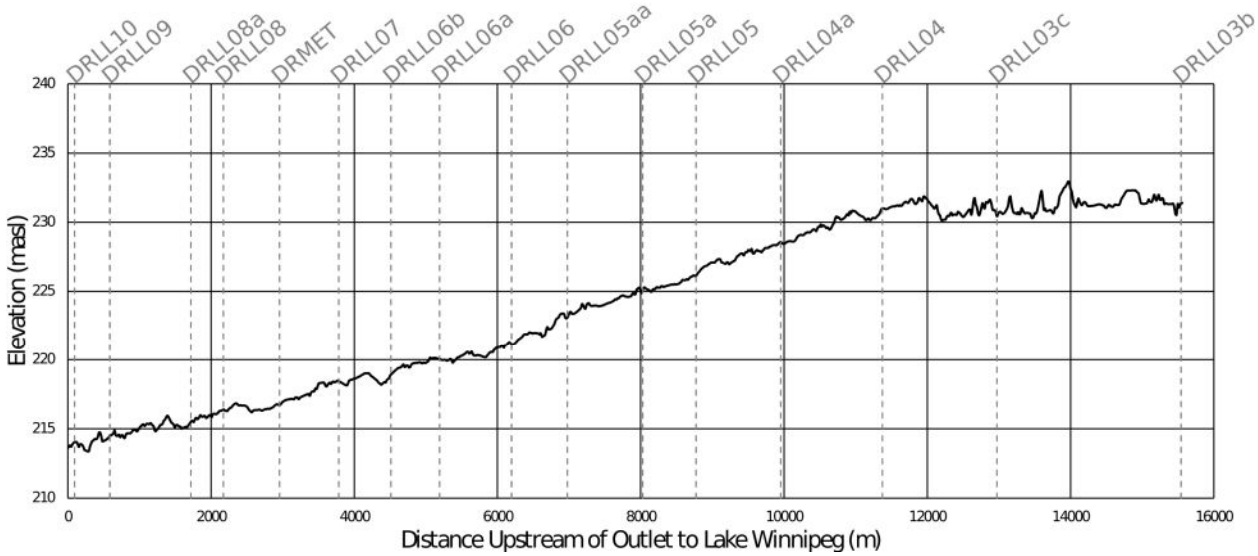

Figure 1.2: Channel bed profile of the Lower Dauphin River, with study locations

Table 1.1: Daily weather data, averaged by month, Dauphin River, Dec. 2015 to May 2020

Month	Min. T. [°C]	Max. T. [°C]	Avg. Wind Vel. [m/s]	Prom. Wind Direction
Jan.	-21.6	-10.3	1.65	SW
Feb.	-23.4	-9.4	1.70	SW
Mar.	-14.1	-0.3	1.82	W
Apr.	-7.2	6.4	1.86	NW
May	2.9	16.2	1.91	NW
June	10.0	22.4	1.63	W
July	13.0	25.3	1.44	SW
Aug.	11.5	24.0	1.28	SW
Sept.	6.8	17.5	1.49	W
Oct.	0.3	8.5	1.88	SW
Nov.	-8.2	-0.3	1.86	SW
Dec.	-18.3	-8.9	1.56	SW

site DRLL03, and logs water surface elevation and flow at five minute intervals, and reports daily values. The data are periodically adjusted for ice effects during the winter.

1.3 Research Objectives

This research hypothesizes that at the time of freeze-up, the surface roughness of a fluvial ice cover will have some relationship to the roughness of the subsurface. Figure 1.3 illustrates this supposition. The objective of this research is to understand and characterize the relationship between surface and subsurface fluvial ice cover roughness.

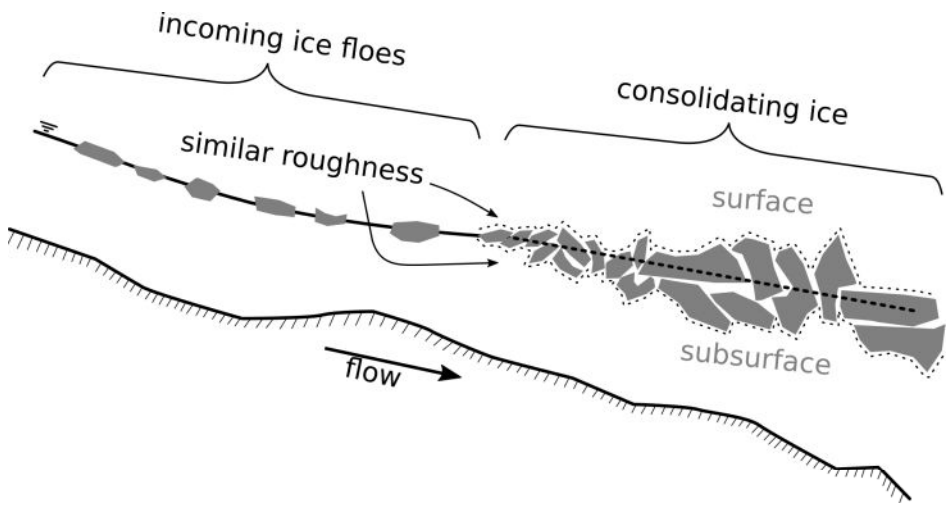

Figure 1.3: Proposed fluvial ice roughness relationship

2 Literature Review

2.1 Hydraulic Roughness and Roughness Characterization

Roughness is an important parameter in the prediction of fluid flow along solid boundaries. This roughness creates drag between fluid boundary layers, generating the logarithmic fluid velocity distribution observed in open channel hydraulics. The portion of flow directly in contact with the flow boundary is known as the viscous sub-layer, and almost fully dictates the characteristics of flow. In the case of a hydraulically smooth boundary, viscous and turbulent shear forces are influential in the viscous sub-layer. Hydraulically smooth boundaries generally do not occur in natural fluvial systems, instead hydraulically rough conditions dominate. Hydraulically rough conditions are those where the perpendicular size of roughness elements exceeds the thickness of the viscous sub-layer. Here, the height of roughness elements becomes far more influential than viscous forces in the determination of the velocity profile. The dimensionless relationship between friction factor, which represents frictional losses in flow energy, and the Reynold's number, the ratio of fluid inertial forces to viscous forces, is illustrated with the Moody Diagram, Figure 2.1. In the chart; ε is the representative height of roughness elements; Re is the Reynold's Number, calculated using fluid density (ρ), fluid velocity (V), and the dynamic viscosity of the fluid (μ); d is a characteristic length scale, pipe diameter in this case.

Additional information is plotted in the chart with the inclusion of multiple lines representing the relative roughness (a scaled representation of flow boundary conditions) of the flow boundary. The plot may be broken into three regions, described by the Reynold's number. On the right hand side of the diagram, at $Re >\approx 3000$, changes in the relative roughness produce differences in the energy lost at constant flow conditions. These conditions are known as turbulent flow. On the left hand side of the plot, at $Re <\approx 2000$ changes in roughness do not impact the flow velocity, as

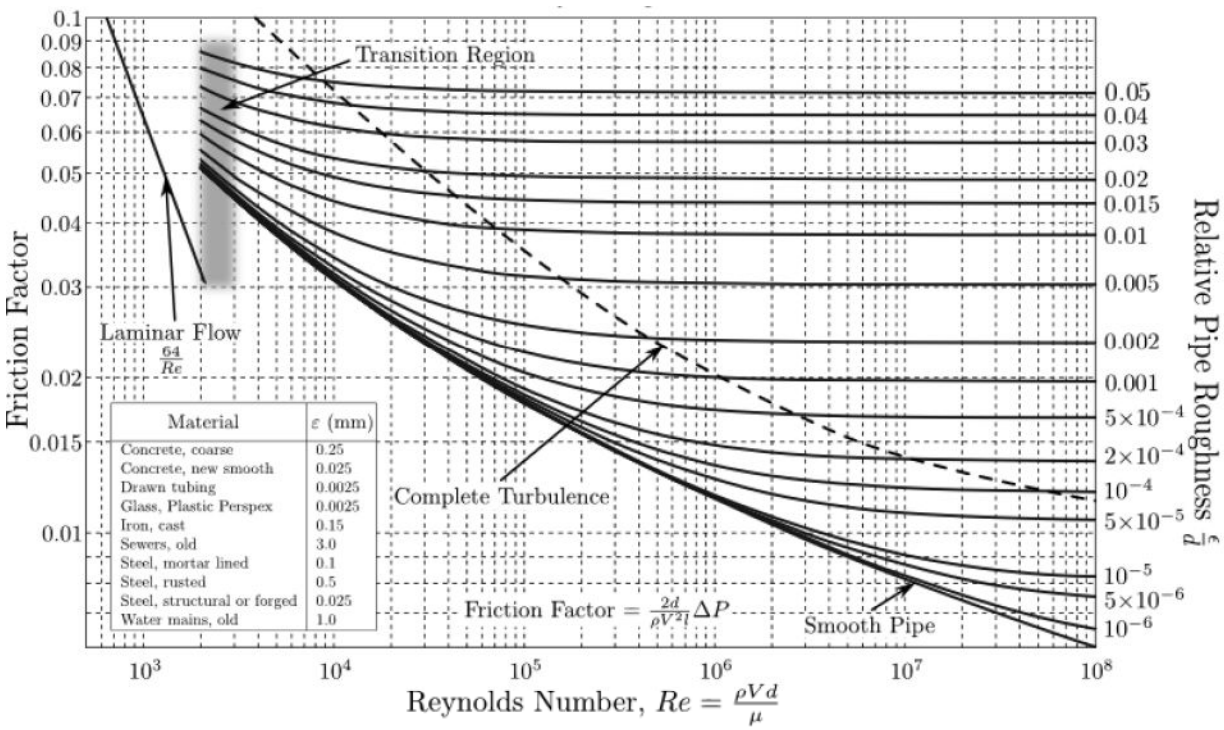

Figure 2.1: Moody Diagram (source: Wikimedia Commons)

shown by all relative roughness lines collapsing into one relationship. These conditions describe laminar flow. The final region is known as the “Transition" region with $\approx 2000 < Re <\approx 3000$, which is poorly understood, and generally not applicable in the hydraulics of natural systems. It is interesting to note that the flow condition, either laminar or turbulent, is independent of the roughness of the flow boundary. Further, at fully turbulent flow, far to the right of the diagram, the conditions generally assumed in natural systems, the friction factor is independent of Reynold’s number, and instead depends only on relative roughness.

Nikuradse (1950) helped develop the concept of roughness height, as associated with the Von Karman velocity distribution law. His experiments used pipes coated in sand, wherein the average dimensions of the sand grains was determined via sieve analysis and manual measurements using a thickness gauge, and taken to be the representative roughness height for computation of the pipe’s relative roughness. Much work has been done in the field of engineering to determine the appropriate methods of characterizing roughness. These calculations are most commonly performed using

a two-dimensional, high-resolution profile of a surface along a chosen transect, known as a surface profile. Surface profiles are measured using many different methods, depending on the scale of roughness under consideration. In the study of surface friction for mechanical engineering applications, Poon and Bhushan (1995) defined contact and non-contact methods of surface profiling. The most popular contact surface profiling method is stylus profiling, where the stylus is moved across a surface at a constant rate, and lateral movement is recorded. Non-contact methods include optical and electrical methods. An extensive discussion of methods used to represent roughness from a surface profile was provided in Gadelmawla et al. (2002), many of which involve statistical analyses of the entire sample, or some subset (i.e. the peaks, valleys, etc.). Gomez (1993) investigated gravel-bed roughness through experiments of an artificial gravel bed in a flume. They used the difference between peaks and a locally-derived average bed surface, measured using a vernier gauge mounted on an instrument carriage which tracked along the length of the flume. Nikora et al. (1998) measured profiles using a rigid frame holding 200 6.0 millimeter (mm) vertical sliding rods, and assumed their surface data derived from natural gravel point-bars constituted a random field, and found that the second-order moment of the frequency distribution yielded a suitable estimate of roughness height when compared to the Wolman (1954) method. Aberle and Nikora (2006) used photographic measurement methods and investigated higher-order statistics but confirmed the use of sample standard deviation (SD) as a representation of gravel bed roughness height.

Manning's equation is the most widely used steady flow equation for fluvial applications in modern hydraulic modeling and relates flow velocity to hydraulic radius (R_h) and slope, with the reciprocal of a third term known as Manning's n. The n value is a dimensionless parameter which is proportional to the sum of the contribution of all roughness elements, including boundary layer roughness in fully turbulent flow. Typical values of Manning's n are widely applied to different channel boundary types, such as cement, steel, earth, and sediment. The Manning's n value is often determined in a qualitative manner, since it lumps together other, less quantifiable features that contribute to flow resistance, such as channel bends and vegetation. A widely-used quantitative

method of estimating Manning's n from roughness height measurements was proposed by Strickler (1923), and is presented below.

$$n \approx c_n D^{1/6} \tag{2.1}$$

The Strickler coefficient (c_n) is the critical parameter of the Strickler equation. Strickler (1923) reported a value of $c_n = 0.047$ for general use, but this can be adapted for specific applications (Sturm, 2001). The Strickler coefficient has units of seconds/meter$^{1/2}$. D represents the characteristic roughness height of the flow boundary in m. Manning's n has units of seconds/meters$^{1/3}$ Julien (2002).

The bulk effect of all roughness contributions in a fluvial system is to impede the flow of water. With all other factors constant, an increase in roughness causes a reduction in flow momentum, and raises upstream water levels. This can be seen by examining the Manning's equation (Equation 2.2): A is the cross sectional area, with SI units of m^2, P_w is the wetted perimeter, with SI units of m, and S is the bed slope (which is equal to the water and friction slope in uniform flow), and has units of m/m. b is a unit conversion coefficient, and has the value 1 or 1.49 if dealing in SI or imperial units, respectively. The components of Manning's equation are illustrated in Figure 2.2. It can be seen that an increase in n must result in an increase in cross sectional area and consequently wetted perimeter to maintain constant flow.

$$Q = \frac{b}{n} A^{\frac{5}{3}} P_w^{\frac{-2}{3}} S^{\frac{1}{2}} \tag{2.2}$$

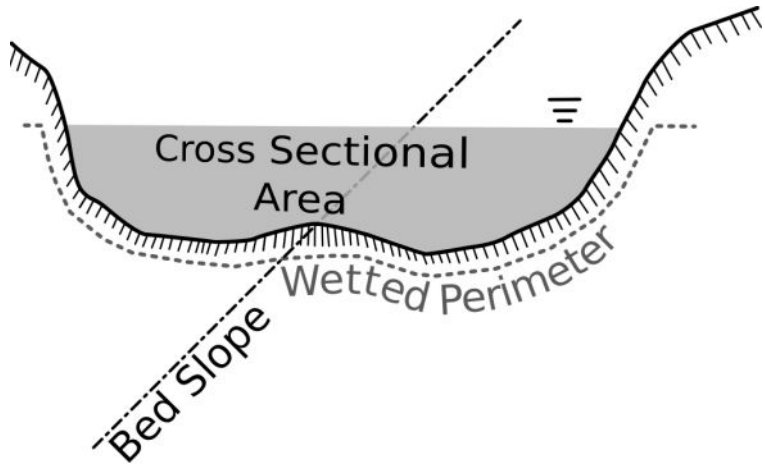

Figure 2.2: Components of Manning's equation

2.2 River Ice Formation and Implications

Ice covers increase hydraulic resistance in fluvial systems by replacing the relatively friction-free air-water boundary with a new ice-water boundary. This expands the wetted perimeter of the channel, and if the ice cover completely bridges the channel, may pressurize flow. The added source of roughness and constriction of flow results in upstream staging (Beltaos, 2013).

In a river system, ice may be formed in several ways. Perhaps the first type of ice to be observed during the freeze-up period is skim ice. This type of ice forms when the water surface has become supercooled, and flow is of relatively low velocity, under 0.5 - 0.9 m per second (m/s) depending on the heat flux between the water surface and the atmosphere (Matousek, 1984). These conditions most often occur in pools and at channel borders. If the skim ice becomes established along a channel bank, and thickens through thermal or mechanical means, it may be then known as border ice. Alternatively, frazil ice may form once the water has become supercooled, and the flow is turbulent and of relatively high velocity, above 0.5 - 0.9 m/s (Matousek, 1984).

Newly-formed frazil ice particles are on the order of 0.5 - 0.05 mm wide (Ashton, 1986), and are in the shape of an thin circular disc. In supercooled water, frazil particles are "sticky", and

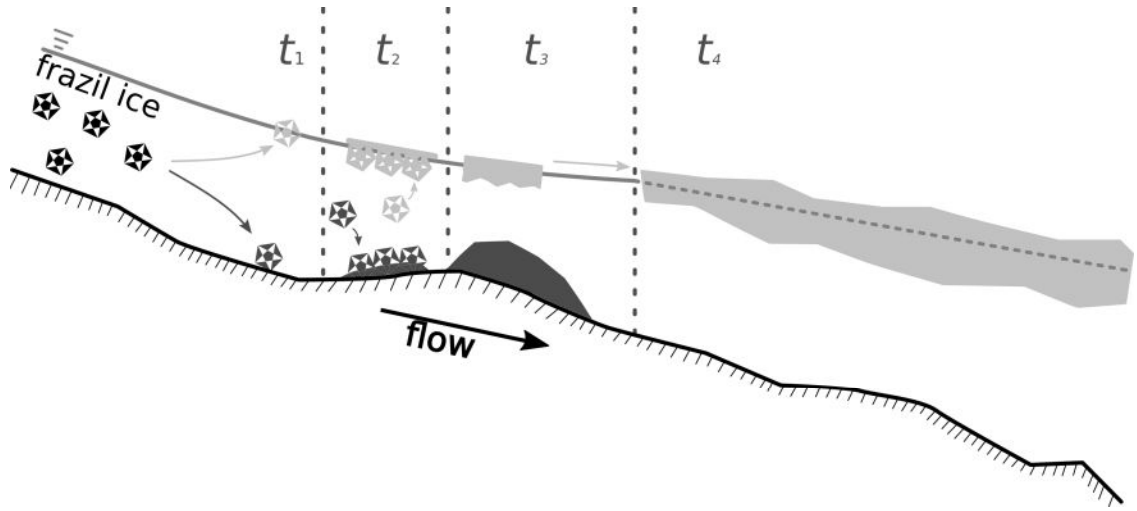

Figure 2.3: Frazil ice generation and evolution

will adhere to other cold objects, including other frazil particles. The general process of frazil formation, transportation, and transformation is shown in Figure 2.3. After generation, frazil ice will be transported downstream (t_1), and either flocculate and rise to the surface to form pans of ice, or attach to the channel bottom, forming anchor ice (Bisaillon and Bergeron, 2009) (t_2). At this stage, pans are very low density, and mechanically weak (Beltaos, 2013). Frazil pans will then be transported further downstream. Depending on their length of travel and weather conditions, the portion of the pan exposed to air may freeze and thicken, adding strength. However, obstacles such as riffles, rapids, or waterfalls may cause them to shatter into smaller pans. Finally, pans may jam against an obstacle, such as established ice cover (t_3 - t_4).

Frazil pans contacting a solid obstacle at water surface level may experience one of several possible outcomes. They may be stopped fully at the water surface level and thus progress the ice cover further upstream. Secondly, their momentum may carry them over top of the ice cover, fully, or partially, and thus extend the cover upstream, albeit at a slower rate than the first case. In the third case, they may sink or underturn to move under the ice cover, and deposit at some further location, or stay in place, as a mirror to the second condition. Finally, if the frazil pan has not gained sufficient strength, it may be crushed by it's momentum contacting the solid boundary.

Indeed, even once any of the first three conditions has occurred, the pans may be crushed by "telescoping" ice shove events (Beltaos, 2013).

Wazney et al. (2018) reported on the mechanisms of wide-channel ice jam consolidation on the Dauphin River and their consequences for the resulting ice cover. During a consolidation event a portion of the temporarily stable ice cover mechanically fails and shoves forward, with ice pieces stacking, crushing, and turning. As a result, the newly consolidated ice is thicker, and generally composed of larger pieces than would be found as frazil pans in the ice-producing portion of the river. Since upstream ice production usually continues, the incoming ice supply causes the ice cover to begin advancing upstream of this newly thickened stationary ice. This upstream ice cover advancement causes an increase in force applied to the ice cover, which may eventually exceed the ice cover strength once again. The resulting sequence of ice cover lengthening, shortening through consolidation events, and then lengthening again is referred to as telescoping. This process can occur multiple times with a compounding effect on ice cover and ice piece thickness. Consolidation events have been shown to generate pressure waves which travel downstream, possibly inducing further events. On any given stationary section of an ice jam, resisting forces oppose driving forces to create a force balance holding the ice in place. Resisting forces include the friction between the jam and the channel banks, and the compression forces, while the driving forces are composed of the flow shear and the downstream component of the jam weight. Shear stresses on the channel boundaries consequently increase as thickening ice cover constricts flow area, increasing water velocity, and larger ice pieces protrude further into the remaining flow area. Ultimately, the jam must be thick enough to withstand a force transfer to the channel banks sufficient to hold it's weight in place. Once stability has been attained, the pieces may further strengthen through freezing.

The specific conditions surrounding fluvial ice cover formation impact the conditions of the final ice cover. One particularly visible result of this is ice cover roughness. Border ice which expands to cover a quiescent pool will have a markedly different roughness from the ice formed by

multiple consolidation events on a riffle reach. As noted in Section 2.1 changes in roughness reduce channel conveyance and produce upstream staging, making ice roughness a critical parameter in hydraulic models considering winter flow. As with estimates of channel boundary roughness, ice roughness can also be judged qualitatively based on general observations, with some success. The Nezhikhovskiy (1964) equation is widely-used for this purpose, in the form provided below.

$$n_i \approx 0.0252 ln(t_i) + 0.0706 \tag{2.3}$$

Where n_i is the Manning's roughness of the ice cover and t_i is the cover thickness in m. This relationship is based on measurements conducted on rivers in Russia several decades ago; their wider applicability is unknown. However, it has served well as an estimation tool for engineering applications. Using more complex data, the Strickler equation (Equation 2.1) was adapted by Beltaos (2013) for use in the estimation of the roughness of newly-formed ice jams, resulting in the following:

$$n_i \approx 0.095 D^{1/2} R_h^{1/3} \tag{2.4}$$

The value given for $c_n = 0.095$ has been determined to be representative for ice jams. Additionally, the inclusion of the hydraulic radius (R_h) term, which is found by dividing the cross sectional area by the wetted perimeter (A/P_w), accounts for the fact that the roughness elements of ice jams are often of such magnitude as to increase relative roughness to the point where it has significant impact on the hydraulic radius. Finally, this relationship is only valid for newly-formed ice jams. Immediately after formation, the ice is subject to shear forces from the water flowing underneath, which serve to slowly smoothen the sub-surface of the cover over the course of the winter (Ashton,

1986).

In addition to reducing conveyance, the presence of an ice cover also changes the distribution of flow. During normal open-channel flow, the velocity is minimal at the channel boundaries, and maximal near the free surface, in the middle of the channel span, as illustrated in Figure 2.4. When an ice cover is formed, along with its additional roughness, the maximum velocity is reduced, and is pushed toward the centroid of the cross section, again as shown in 2.4. In this case, an isoline of maximal velocities may be plotted, which conceptually divides the flow area into that which is ice-affected, and that which is bed-affected. The location of this line will depend on the relative magnitude of roughness exhibited by each area. An ice cover with the same roughness as the channel boundary will produce roughly equivalent ice and bed-affected flow areas. An increase in roughness in the ice cover will consequently increase the ice-affected flow area.

This relationship requires special attention when attempting to determine a single roughness for application in modeling using Manning's equation. Due to their areas of influence, the ice and bed roughnesses are not simply additive. Many relationships have been proposed for determining a single, composite roughness n_c. Perhaps the most widely used is the Sabaneev equation, as found in Uzuner and Kennedy (1976) and shown below.

$$n_c = n_b \left[\frac{1 + \frac{P_w^i}{P_w^b} \left(\frac{n_i}{n_b} \right)^{\frac{3}{2}}}{1 + \frac{P_w^i}{P_w^b}} \right]^{\frac{2}{3}} \tag{2.5}$$

The variables n_i, n_b, and n_c are the ice, bed, and composite roughnesses, respectively. P_w^i and P_w^b were taken to be the wetted perimeter of the ice cover and channel bed, respectively.

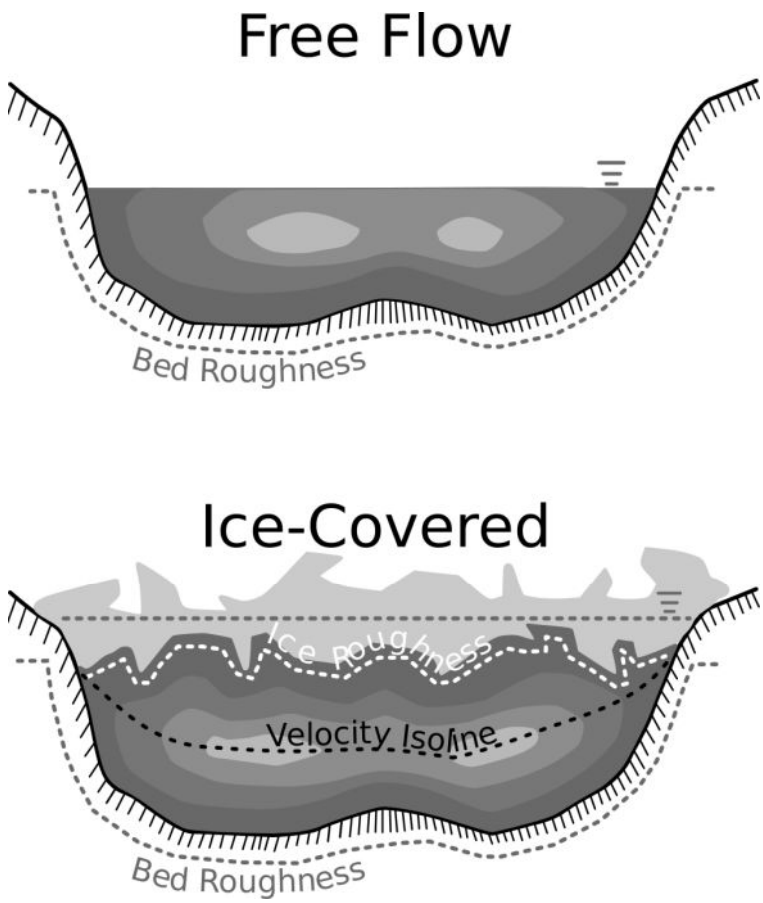

Figure 2.4: Example cross sectional hydraulics of free-flow and ice-covered conditions, contours are printed for illustrative purposes only

2.3 Remotely Piloted Aircraft and Photogrammetry

Recently RPA equipped with high-resolution digital cameras have been used extensively in the collection of near-surface photographic and topographic data (Colomina and Molina, 2014; Watts et al., 2012). They are smaller and more cost-effective than conventional aircraft, allowing for much more versatile data collection. Compared to manual surveying methods, they can collect a greater volume of data in less time, and greatly reduce risk to personnel. Additionally, Lane et al. (1993) proposed that the retrodictive nature of data collected via photogrammetry allows the researcher to decide how and what to analyze after the fact, rather than committing to a predefined sampling strategy. For the purposes of topography, images collected with an RPA are subsequently

processed using some form of photogrammetry, a three-dimensional rendering algorithm which uses the parallax between stereo-matched points to infer distance. The ultimate goal of this analysis is a three-dimensional, geo-rectified digital representation (Digital Elevation Model) of the area contained within the set of images captured by the RPA. The use of photogrammetry on RPA collected images for the purposes of topographic data collection will henceforth be referred to as "RPA photogrammetry". Niethammer et al. (2012) used this method to monitor the progression of the Super-Sauze landslide, a dangerous field task if it were to be monitored manually. Eisenbeiss et al. (2005) employed RPA photogrammetry to document in detail the layout of ancient ruins in Peru. Completing this task manually would have risked the integrity of the site. Hamshaw et al. (2019) found use for RPAs in the monitoring of river-bank erosion. RPAs were even used by Alfredsen et al. (2018) in the mapping of river ice in Norway.

Several operational and external factors impact the quality of topographic data collected via RPAs. Lane et al. (2000) found that quality of experimental design for RPA flights was a larger source of error than those produced in the subsequent photogrammetry analysis. From an operational standpoint, wind speed, visibility, data collection area, and light conditions are perhaps the most critical parameters to take into account. Limiting wind speeds for RPAs depend on the mass and engine power for the specific unit, as well as local laws. Wind speeds exceeding 30 km/h overwhelm most small aircraft (Kienapple, 2017). Canadian law requires that an RPA be flown within visual line of sight, which depends on local terrain and vegetation. Weather conditions such as rain, snow, and fog will also limit the line of sight. The total area to be captured must be carefully considered, factoring in estimated battery life, and image density. Finally, light conditions are important for line of sight as well as quality of images collected. Eisenbeiss et al. (2005) and Alfredsen et al. (2018) both reported that bright light conditions casting strong shadows can cause errors in subsequent photogrammetry analysis, particularly if those shadows change with sun angle over the flight time. From the perspective of image quality, light conditions (as discussed previously), altitude, camera angle, and image overlap are of greatest concern. Flight altitude should

remain constant throughout the flight to aid in point matching. Flight altitude will also determine field of view for the attached camera. Given a set flight time, a larger area may be captured with an RPA flown at a higher altitude. The trade-off is that fine details will be more obscured. Camera angle also impacts the field of view. A 0°camera angle will capture an image directly below the RPA, while any larger angle will capture a somewhat wider trapezoidal area. While capturing some images at a slightly oblique angle may be helpful for certain terrain (Alfredsen et al., 2018), too high of an angle may capture too large of an area leading to irreconcilable points in the photogrammetry algorithm. Finally, image overlap is perhaps the most important parameter related to final accuracy of the photogrammetry product (Westoby et al., 2012). This does however depend on the features being captured, the required level of detail, and flight time restrictions. Alfredsen et al. (2018) had success using as little as 20% overlap, while others have prescribed a minimum 75% overlap (Eisenbeiss et al., 2005) to upwards of 95% (Harwin and Lucieer, 2012).

There are several methods of producing a Digital Elevation Model (DEM) from a set of overlapping close-range aerial images. Currently, the most widely used and time-effective method is that of Structure from Motion (SfM) photogrammetry (Matthews, 2008; Fraser and Cronk, 2009). Previous methods relied on user-defined "tie-points", those points which are used to match and orient images. Alternatively, the SfM algorithm determines tie-points internally (Snavely, 2009). For the purposes of this research, SfM photogrammetry will be the sole method of consideration.

In the application of SfM, each image is first analyzed to determine "keypoint descriptors" (Snavely, 2009), or prominent features which can be identified in two or more images. This is generally done using the Scale Invariant Feature Transformation object recognition system (Lowe, 2004), a method of finding a set of nearly unique values that represent the local characteristics of important image features, such as boundaries. The goal of this is to find features which can be recognizable at different scales (translates to camera altitude in RPA flights), rotations (translates to camera pose), and illuminations (translates to changes in sun angle and shade) so they may be

identified in multiple images. Next, these keypoints are linked between images, matching their unique values, and camera position is inferred from their correlation (Snavely, 2009). A sparse point cloud is then generated in a local coordinate system now knowing the relative position of key features in each image. Bundle adjustment is undertaken using optimization algorithms to find optimal camera placement and pose (Harwin and Lucieer, 2012), and a dense point cloud is generated. To convert the point cloud to a real coordinate system, surveyed ground control point data must be manually added (Westoby et al., 2012). Finally, a DEM may be generated from the geo-rectified dense cloud.

An important consideration when using the RPA-photogrammetry method for topographic data collection is the impact of doming errors on the final product (James and Robson, 2014). Doming errors are most prominent when all images are taken from a parallel axis (Eltner and Schneider, 2015). In the case of RPA-photogrammetry, this is when the camera angle is set to 0° tilt; however, some distortion is also caused by the shape of the camera lens. Most advanced software packages used to produce three-dimensional surfaces from photogrammetry data include a self-calibration process that develops a model of the distortion caused by the lens of the camera. Additionally, many purpose-built cameras used on RPAs come with software pre-processing to correct lens distortion. James et al. (2020) argued that it is not yet clear if these corrections universally reduce doming errors in DEMs, while Eltner and Schneider (2015) found that along with ground-control points corrected images were a major factor in minimizing doming errors.Eltner et al. (2016) makes the distinction between local surface quality and more systematic errors such as doming, relating these two categories to the precision and accuracy of the surface, respectively.

Fourier analysis is most commonly used in one-dimensional signals analysis, but can be applied to different data in higher dimensions. It has been used to examine the components of undesirable patterns in DEMs (Liu and Jezek, 1999). This analysis finds the characteristics of a set of sine waves which, when combined, fully recreate the input data. The frequencies of the resultant sine

waves may then be considered to determine which are responsible for noise or extraneous patterns in the data. Undesirable frequencies can be filtered by simply setting their amplitude to 0. The results may then be passed through a reverse Fourier transform, recreating the original surface, less the impact of unwanted frequencies. This resultant surface can then be analyzed for representative characteristics, such as roughness height.

3 Materials and Methods

Several field sites were selected on the Lower Dauphin River, as summarized in Table 3.1. Their relative locations are shown in Figure 1.1. This study collected data in the winter months between 2017 and 2020. In general, sites DRLL01, DRLL02, DRLL03, and DRLL03a are not considered in the following analyses, as they were located far enough upstream of the grade break between the Lower and Upper Dauphin River that complex ice dynamics were not observed. A smooth ice cover has been observed to form at DRLL03b in all previous years, due to it's low bed slope (0.029%). Sites DRLL05 and DRLL06 exhibited substantial ice dynamics as they are within the higher gradient (0.16%) Lower Dauphin River (Wazney et al., 2019a), when compared to DRLL08 and DRLL08a which had much milder water surface slopes, and were affected by the Lake Winnipeg water level. The toe of an ice jam has formed in previous years near sites DRLL08a and DRLL08. These sites were selected in an effort to compare the efficacy of the RPA photogrammetry method on different ice conditions, and to determine if the methods can distinguish roughness differences between sites.

A conceptual summary of the pertinent data collected, and it's relationship to the proposed methods of testing the hypothesis is presented in Figure 3.1. Roughness measurements were conducted, as shown by the RPA in the top middle of the graphic; the detailed field and laboratory methodology for this are presented in Sections 3.1 and 3.3. If possible, ice thickness was measured

Table 3.1: Field site summary, number of observations per study year

Site Name	'17-'18	'18-'19	'19-'20	Description
DRLL03b	0	0	1	Low-gradient, smooth ice
DRLL05	1	0	2	High-gradient, dynamic ice
DRLL06	3	2	3	High-gradient, dynamic ice
DRLL08	0	0	1	Lake-affected, ice jam toe
DRLL08a	1	1	2	Lake-affected, ice jam toe

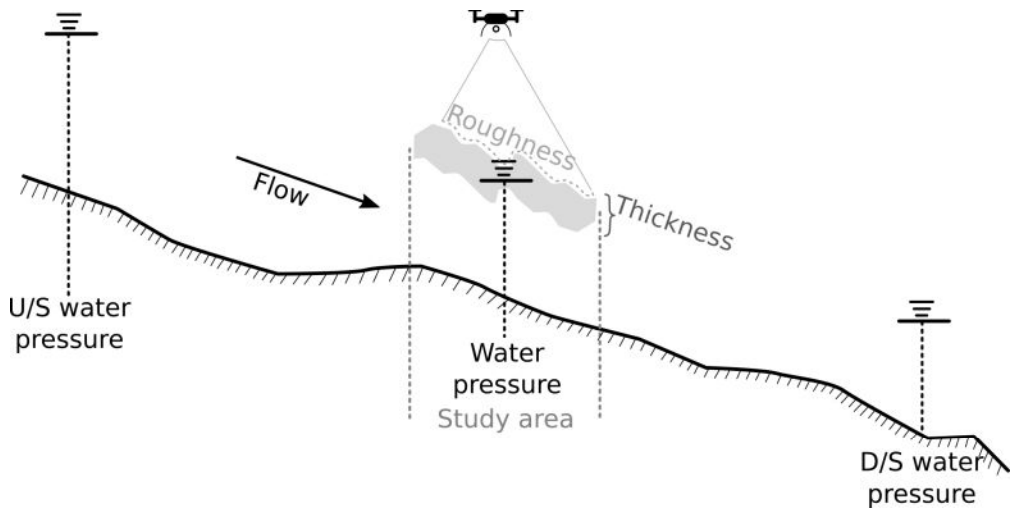

Figure 3.1: Conceptual schematic of collected field data

at the site using the methods presented in Section 3.2. Additionally, water pressure was recorded continuously at the study site, and at the stations immediately upstream and downstream of the study area, with the methodology outlined in Section 3.2. These data were then used to determine the upstream and downstream water surface slopes, for use in further analysis, as described in 3.4. Flow was collected by the WSC, as described earlier in this section. Table 3.2 outlines the dates of field visits, and what tasks were undertaken.

3.1 Photogrammetry

Ten 1 m^2 high-visibility medium-density fiberboard targets were distributed on the grounded ice near the left bank, and on snow near Provincial Trunk Highway (PTH) 513. A typical layout of targets is shown in Figure 3.2, which illustrates how the targets are placed exclusively on the left bank of the river. The targets must be clustered in this way since the right bank was inaccessible. Ideally, the targets would be evenly distributed across the entire study area (Alfredsen et al., 2018; Gini et al., 2013). In Section 3.1.1, the methods used for testing the effects of target distribution on surface accuracy are presented.

Table 3.2: Field schedule

Date	Location	Purpose
2017/10/24 - 26	Dauphin River, MB	Levelogger® and trail camera deployment
2017/11/21 - 23	Dauphin River, MB	Photogrammetry at DRMET, DRLL06, DRLL06a, and DRLL08a
2018/02/21 - 23	Dauphin River, MB	Top of ice survey, photogrammetry at DRLL05 and DRLL06
2018/06/05 - 07	Dauphin River, MB	Levelogger® and trail camera retrieval
2018/10/15 - 17	Dauphin River, MB	Levelogger® and trail camera deployment
2018/11/21 - 22	Dauphin River, MB	Photogrammetry at DRLL06 and DRLL08a
2019/02/19 - 20	Dauphin River, MB	Top of ice survey, photogrammetry at DRLL06 and DRLL08a
2019/04/05	La Barriere, MB	Photogrammetry testing
2019/06/05 - 07	Dauphin River, MB	Levelogger® and trail camera retrieval
2019/08/21 - 22	Dauphin River, MB	Supplemental channel survey
2019/10/30 - 31	Dauphin River, MB	Levelogger® and trail camera deployment
2019/11/12-14	Dauphin River, MB	Photogrammetry at DRLL03b, DRLL05, DRLL06, DRLL07, DRLL08, and DRLL08a
2019/11/26	Dauphin River, MB	Photogrammetry at DRLL06 and DRLL08a
2020/02/18 - 21	Dauphin River, MB	Top of ice survey and ice thickness measurements
2020/06/08 - 09	Dauphin River, MB	Levelogger® and trail camera retrieval

After targets were placed, their centers were surveyed using a Leica Viva GS14® survey-grade Global Navigation Satellite System (GNSS) base-and-rover system, which was typically observed to have a horizontal accuracy of $\approx$ 5 centimeters (cm), and a vertical accuracy of $\approx$ 10 cm. As mentioned in Section 2.3, geo-rectification of surfaces produced through RPA-photogrammetry occurs after the generation of a dense cloud. A dense cloud is all that is necessary for the production

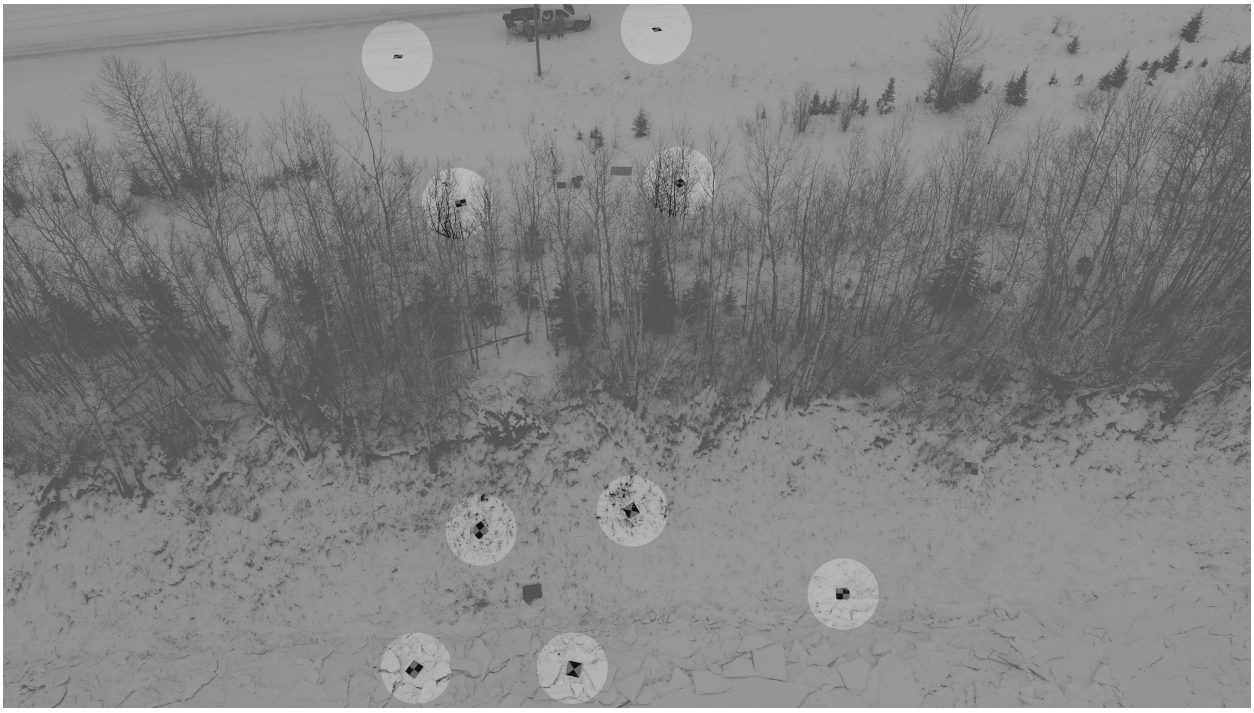

Figure 3.2: Typical target distribution

of a DEM. The process of geo-rectification allows for the resultant DEM to be compared to other geospatial data. However it may not be strictly necessary for the analysis of surface roughness characteristics since these analyses are conducted in a shifted spatial reference frame. A comparison between the representative metrics calculated from a surface before and after geo-rectification is presented in Section 4.1.1. Based on these results, in the 2019-2020 season some RPA flights were completed without targets to allow for more flights to be completed during the field visit.

Once all field personnel had finished active tasks, the RPA was launched, and field staff remained stationary for the duration of the RPA flight. A DJI Phantom 4 Professional® RPA was flown at an approximate altitude of 30 m, with overlapping photos taken every 10 m, at a 0° or 20° camera tilt off of nadir. The on-board 20 megapixel camera had an 84° field of view with a 1 inch CMOS sensor. The RPA flight transected the river and included PTH 513 and forest on the left and right bank. The RPA was flown only if wind speeds measured by a hand-held digital anemometer were less than 36 km per hour (km/h). Finally, light conditions can drastically impact

the quality of images taken, therefore the RPA was flown only during clear, or lightly overcast conditions. Typical capture dimensions of a RPA flight were 90 m in the streamwise ordinate, and 230 m across the river.

During the 2019-2020 field season, the RPA mission planning application Pix4Dcapture® was used to plan and automate RPA flights over study areas. This greatly reduced the required flight time, and produced similar, if not better photo coverage.

PhotoScan Professional® from AgiSoft LLC was used for all photogrammetry image processing in this study. This program uses the SfM method of photogrammetry, which has been widely used in geosciences in recent years (Westoby et al., 2012). Gini et al. (2013) compared their custom research-grade photogrammetry algorithms to results obtained from Pix4UAV Desktop® and PhotoScan Professional®. Their findings suggested that these commercial packages performed similarly to their software, with PhotoScan Professional® performing somewhat better than Pix4UAV Desktop®. PhotoScan Professional® is also considered to be a relatively fully-featured and complex (Eltner and Schneider, 2015) tool as compared to other options, and includes an automated process for estimating and correcting doming errors.

Images were imported into PhotoScan Professional®, and aligned to create a sparse point cloud of tie points. Where targets were used, they were identified in all images containing them, and their coordinates were imported to provide geo-rectification of the resultant point cloud. A dense point cloud was then generated, followed by a DEM. An example point cloud and DEM are shown in Figures 3.3 and 3.4.

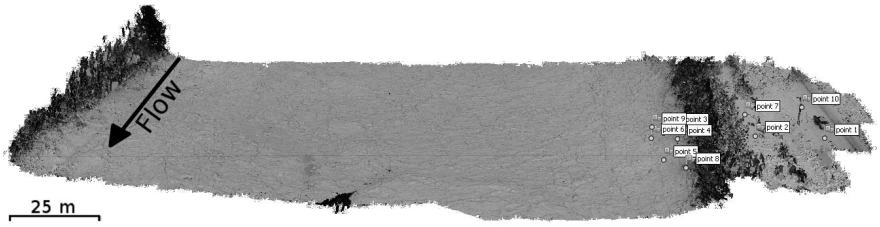

Figure 3.3: Example point cloud, DRLL06 2018-11-21

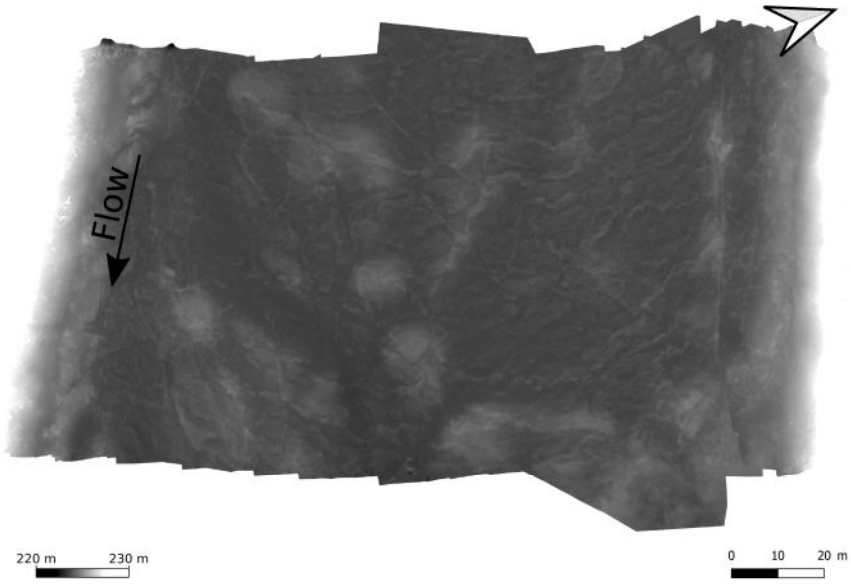

Figure 3.4: Example DEM, DRLL06 2018-11-21

3.1.1 Field Accuracy Tests

Ideally, geo-rectification targets used in RPA-photogrammetry would be evenly distributed across the study area. In this research, targets could only be placed on the left bank of the study area, and none could be placed directly on floating ice, due to safety concerns. Therefore, there was a need to quantify the impact of this non-ideal target placement scenario. A maximum acceptable vertical error target of 0.1 m was adopted, since this was the upper limit of expected field accuracy of the GNSS base-and-rover system (Clark and Lee, 1998; Johnson and Barton, 2004). The GNSS base-and-rover system was the limiting factor for accuracy in this study since it is the tool which informs the absolute spatial position of all field equipment. The field methods described in Section

3.1 were repeated at River's Edge Nursery in La Barriere, Manitoba. A fully dry land study area of equivalent size to typical study areas flown at the Dauphin River was delineated, and 15 targets were distributed. The targets were conceptually grouped into three areas: typical, middle, and end, as illustrated in Figure 3.5. The "typical" group represented a target distribution that was generally produced during field work at the Dauphin River sites. The "middle" and "end" target groups were supplemental, which would be added or subtracted from the photogrammetry analysis to test their respective impacts on surface quality.

Additionally, six rectangular cuboids of various known dimensions were placed throughout the study area. Their top surface areas ranged from 0.05 to 0.24 m^2 and their heights ranged from 0.06 to 0.6 m. The intent was to evaluate the ability of the RPA-photogrammetry technique to capture angular shapes. Finally, after the RPA flight was conducted, 10 independent and unmarked locations were captured by GNSS survey as a check for accuracy in subsequent data analysis.

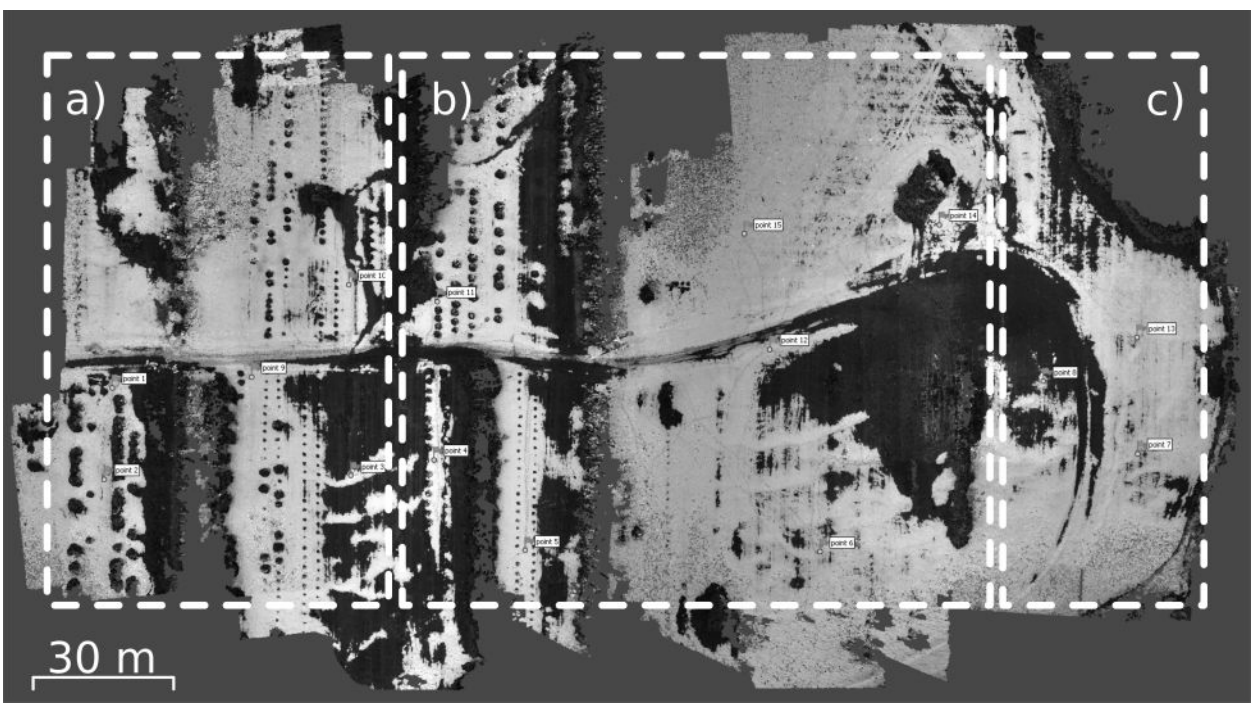

Figure 3.5: Accuracy test experimental set up, a) typical, b) middle, c) end

Three scenarios were tested using the land-based test data gathered at La Barriere, Manitoba,

as described below.

- **All Targets Scenario**: All 15 targets across the three groups were used in the photogrammetry procedure. This was regarded as the most accurate scenario.
- **Typical Targets Scenario**: Only the seven targets in the “typical" area were used in the photogrammetry procedure. The remaining targets were used as an accuracy check. This tested the accuracy of a surface generated with targets clustered on one side of the study area.
- **Three Target Scenario**: Three targets in the “typical" area were used in the photogrammetry procedure. This scenario tested the accuracy of a surface generated using the minimum number of targets for three-dimensional rectification. The intent was to determine if sufficiently accurate results could be obtained with minimal resources and time.
- **Two Target Scenario**: Two targets in the “typical" area were used in the photogrammetry procedure. This scenario aimed to determine how poorly the results could be with fewer targets than required.

In each scenario, the ten independently surveyed points, as well as any unused targets were used to compare the elevation deviation from the “all targets" scenario. Further, the representations of the six rectangular cuboids in the resultant surface were measured and compared to their known dimensions. A maximum acceptable absolute vertical error of 0.1 m was adopted to evaluate the results of this test.

During the 2019-2020 field season, some test sites were flown without the placement and survey of geo-rectification targets. This was done under that assumption that lack of geo-rectification targets would not severely influence the resultant surface texture. The test performed at the La

Barrier field site was formulated to test the impacts on surface accuracy. An additional test was required to determine if systemic errors were introduced in surfaces generated without the use of geo-rectification targets. The data collected at site DRLL06 on 2019-11-13 was prepared using the methods introduced in Section 3.1 and 3.3, and then prepared again using the same method, although this time skipping the geo-rectification step. A maximum acceptable percent error of 5% was adopted to evaluate the results of this test.

3.2 Hydraulic Parameters

Water pressure was recorded every eight minutes at the study sites using Solinst Levelogger® Edge 3001 M5 pressure transducers, and accompanying nearby Solinst Barologger ® Edge 3001. The listed accuracy of these devices is $\pm$ 0.003 m and $\pm$ 0.05 kPa respectively. These instruments were installed before the ice season began (typically October), removed for download and maintenance after the end of the ice season (typically April/May), and were then subsequently re-installed for summer flow observations. During installation, the water surface was surveyed for use in post processing to determine the absolute Water Surface Elevation (WSE) of the observations in meters above sea level (masl). Additionally, the observed barometric pressure, converted to its equivalent depth of water, was subtracted from the pressure observations.

Late in the winter (typically February) after a stable ice cover had formed, an ice elevation survey was undertaken. Using the base-and-rover system, the top of ice elevation was surveyed along the length of the Lower Dauphin River. Truncated transects of ice thickness were also surveyed at locations where ground elevation had previously been surveyed. A transect was performed at site DRLL06 and DRLL05, but not at DRLL08, due to safety concerns. During the 2019-2020 field season holes were drilled in the ice cover at safe locations, and following established safe work procedures, to determine ice thickness. If measurements of ice thickness were not possible at a

given site, for a given year, thickness was estimated through observation and photographs.

Most of the channel geometry was determined through a bathymetric survey conducted by KGS group and the Province of Manitoba. Supplemental channel surveys were conducted in the area nearby DRLL06, DRLL07, and DRLL08a using a Nikon Nivo 3.M® Total Station and SonTek RiverSurveyor M9® ADCP towed by a flatwater kayak. These surveys provided additional detail for cross sectional hydraulics and reach slope.

3.3 Roughness Characterization

The photogrammetry method outlined in Section 3.1 produced surfaces of the study area which included trees, roads, and other objects near the river. Further, during some field visits, the ice cover was partially grounded near the banks. To avoid unwanted influences in the surface slope and texture, a 50 m^2 sub-sample from the center of the river was taken, which excluded all overbank objects and sections of the ice cover that were near to the bank. Additionally, a three-dimensional plane-of-best fit (linear model) was found for each sample, and then subtracted from the surface data. The goal of this was to normalize each data set, setting the mean surface elevation to 0, and removing the river slope from the sample data. Gadelmawla et al. (2002) notes that the mean surface elevation is the most commonly used and most sensible reference standard from which to assess roughness height. By shifting the elevation data down to a base elevation of 0 masl and removing unwanted patterns, each data point was transformed from an elevation to a roughness height.

A two-dimensional Fast Fourier Transform (FFT) was then applied to each sub-sample, with the goal of filtering the input data and removing other surface trends beyond those addressed with the plane-of-best-fit. An analysis of dominant frequencies was performed on a test surface, which is

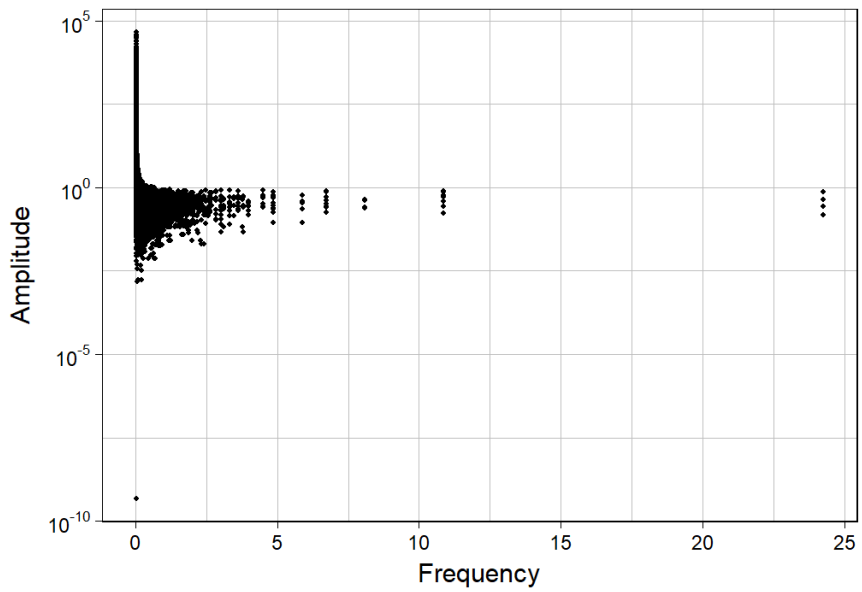

Figure 3.6: Representative frequency-amplitude histogram for tested ice surfaces, DRLL06 2018-11-21

displayed in Figure 3.6. It was concluded that components associated with low-frequency effects, such as the curvature of the ice surface due to flow subsidence, had the largest amplitudes. The highest frequency signals were associated with noise in the image and generally had the lowest amplitudes.

A two-dimensional FFT analysis reports the amplitude and phase of one sine wave for each element of an input matrix, in other words, an image composed of N-by-N pixels (the input matrix must be square) will produce an N-by-N Fourier matrix. A typical distribution of amplitudes is shown in Figure 3.7 a. These results are arranged such that the highest frequency waves are found in the center of the matrix, while the lowest frequencies are found in the corners of the matrix (Smith, 1997). Based on this interpretation, a band-pass filter was constructed as an annulus about the center of the results matrix, the result of the application of this filter is shown in Figure 3.7 b. Each point in the results matrix was interpreted to have a frequency based on its distance from the center using the spatial coordinates of the original image. Frequencies corresponding to wavelengths shorter than 0.08 m were removed since these were below the expected accuracy of

the combined RPA and topographic survey methods. The high-pass component of the filter was adjusted for each image, to ensure large trends were removed. The wavelength cut-off ranged from 70 m to 70.5 m. Figure 3.7 c and d show the surface before and after the application of this filter. Results comparing the quality of surface data resultant from both the linear modeling and the additional two-dimensional FFT are presented in Section 4.2.1.

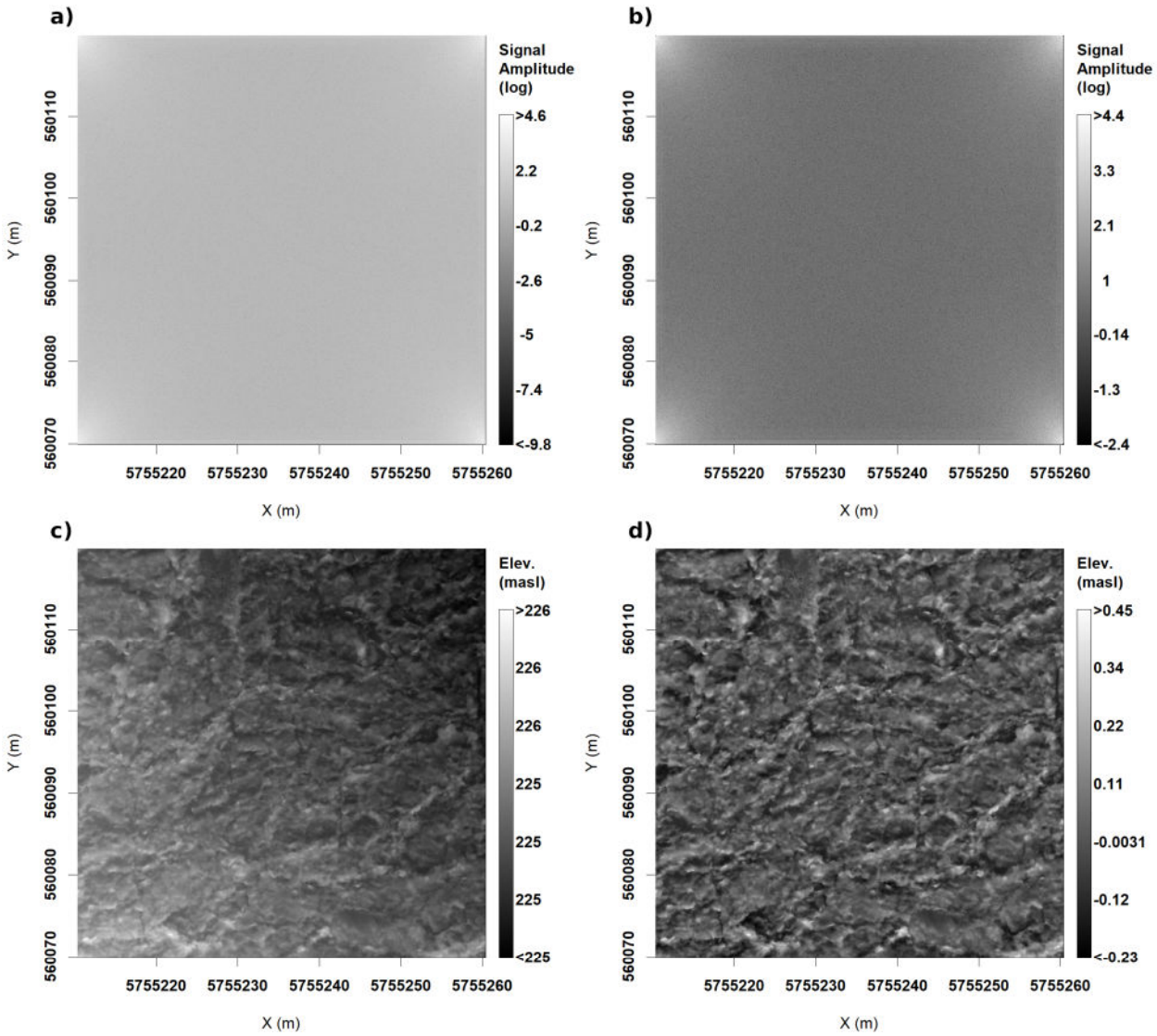

Figure 3.7: Summary of impacts of filtering through Fourier analysis, DRLL06 2019-11-13

Once the data were in a form that directly represented roughness height, and unwanted patterns had been removed, assessment of statistics representing bulk roughness were computed. Based on a review of relevant literature in the fields of photogrammetry, fluvial geomorphology, and

Table 3.3: Selected statistical methods

Method	General, Peaks, or Both	Reference
IQR	General	(Aberle and Nikora, 2006)
SD	General	(Aberle and Nikora, 2006)
Min. Peak Value	Peaks	(Gadelmawla et al., 2002)
Max. Peak Value	Peaks	(Gadelmawla et al., 2002)
Mean of Peaks	Peaks	(Gadelmawla et al., 2002; Gomez, 1993)
84th Percentile of Peaks	Peaks	(Beltaos, 2013)

roughness characterization, various statistical methods were considered, and several were chosen for further consideration in this study (Table 3.3). A more detailed discussion on the specifics of these methods was offered in Section 2.1. Aberle and Nikora (2006) suggests the use of SD as a characteristics roughness height for a normally-distributed roughness sample. For non-normal data, the inter-quartile range (IQR) is a more suitable representation of the spread of the data. The data were grouped into three categories: the first being the “Raw" data, which was the set of surface data as reported by the RPA-photogrammetry technique; the second is referred to as the “General" data, which was all the surface data after linear and FFT analyses have been conducted; and the “Peaks" data, which corresponded to values of peaks within the sample. Figure 3.8 illustrates the difference between the General and Peaks categories of roughness height measurements. Peaks were determined using a two-dimensional overlapping transect approach, where each row of the data were evaluated for peaks, and then compared to peaks found in each column of data. True peaks were then taken to be those cells of the data set which were peaks in both the row and column searches.

The roughness heights found from the above methods were then used to calculate Manning’s n for each value, using Equation 2.4, which is an adaptation of the Strickler formulation and has been used for ice jam roughness. The hydraulic radius was found using Manning’s equation, with the observed flow and water depth, and observed or calculated ice thickness at the time of the RPA

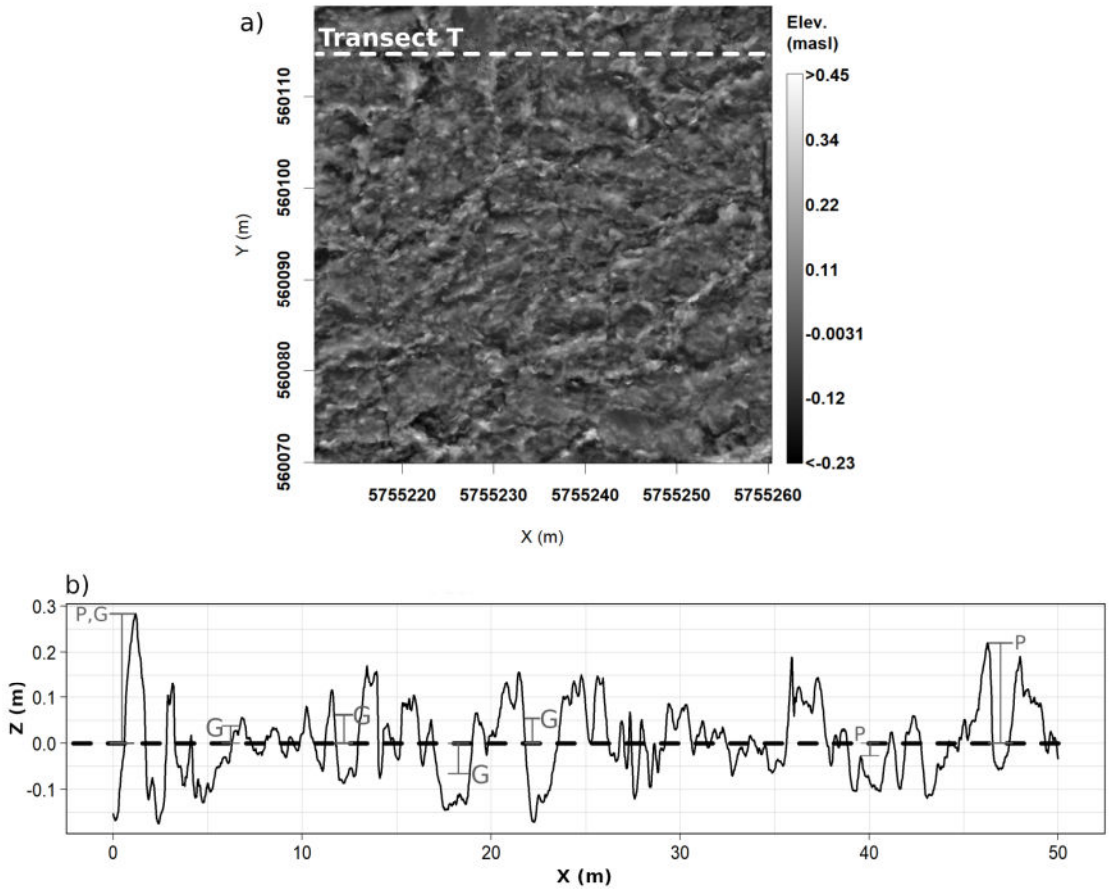

Figure 3.8: a) filtered ice surface DEM illustrating example transect T location, b) profile of transect T. P represent peak values, or local maxima, and G represent general values, which incorporate all roughness height observations in a sample, including peaks. Data are taken from DRLL06 2019-11-13.

flight.

In addition to numerical characterization of roughness, classification of roughness type was undertaken using k-means clustering, which is the most commonly-used clustering approach (Jain, 2010). The data used for input were the following: IQR of the general and peak data, median of the peak data, and kurtosis of the general and peak data. Mean and median of the general data were excluded since they were set to 0 through the linear adjustment and Fourier analysis. The mean of the peak data was excluded since it is the first statistical moment, and is related to the kurtosis.

SD was removed from both data sets since it is used in the computation of kurtosis, likewise with skewness. The data were then mean-centered and the optimal number of clusters was determined using the average silhouette method. K-means clustering using the Euclidean distance formula was then performed.

3.4 Hydraulic Modeling

In order to test the hypothesis of this research, inverse hydraulic modeling was employed to determine ice roughness values based on collected hydraulic data. HEC-RAS was applied to the determination of reach-averaged bed roughness values using open-water flow and WSE observations. HEC-RAS is a one-dimensional backwater model which uses the implicit finite-difference method to solve the one-dimensional simplification of the St. Venant equation, as shown in Equation 3.1. u is the flow velocity in the x (downstream) direction, t is time, h is the depth of flow, g is the gravitational constant, and S_f and S are the friction and bed slopes, respectively.

$$\frac{\partial u}{\partial t} + u\frac{\partial u}{\partial x} + g\frac{\partial h}{\partial x} + g(S_f - S) = 0 \tag{3.1}$$

In this research, HEC-RAS was successful in the calibration of reach-averaged channel bed roughness values during open water flow conditions. It's application to ice-covered conditions was unsuccessful in this research. Unfortunately, through several trials, HEC-RAS could not account for all ice and hydraulic implications of the cover observed on the Dauphin River, and failed to reproduce the observed water surface profile. Further, while detailed ice observations had been made, there were not enough data to confidently model the ice cover thickness across the entire 15 km reach.

In lieu of HEC-RAS, a one-dimensional at-a-station hydraulic model (referred to from here on in as the ice roughness model) was developed to determine ice roughness values. The ice roughness model was based on Manning's equation, Equation 2.2, and considered the cross sectional hydraulics of a single station. Channel bathymetric data were used in conjunction with observed or assumed ice thickness and WSE observations to determine flow area, A and wetter perimeter, P_w. The specific gravity of ice was assumed to be 0.916. Slope, S was determined using the elevation difference between WSE observations of the nearest upstream and downstream stations. The composite roughness n_c was determined using the Sabaneev equation, Equation 2.5. The values of P_w^i and P_w^b were taken to be the width of the ice cover (top width), and the wetted perimeter of the channel, P_w. The channel bed roughness, n_b was determined through manual calibration of an open-water HEC-RAS model, which will be described in more detail in subsequent paragraphs. The remaining term, n_i, ice roughness, was the calibration parameter to be iterated in pursuit of a solution.

3.4.1 Model Assumptions

Since the ice roughness model used Manning's equation, the assumption of uniform, steady flow was implicit in its calculations. Additionally, given the model's simplicity, channel constrictions or expansions could not be considered. However, field monitoring sites were located in the middle of straight, uniform reaches. During the formation of fluvial ice covers, flow is not uniform, which requires the use of the energy slope in such a model. The data demands for an accurate representation of the slope of the energy grade line are quite extensive, making the water surface slope a generally more practical choice. To justify this choice, an estimate of the energy grade line slope was determined for two of the major sites in this research, DRLL06 and DRLL08a. The difference between the water surface and energy grade line slopes was found to be less than 15%. Since the energy grade line slope calculations required additional assumptions, it was decided that

the water surface slope was an acceptable substitute.

A representative flow was required for the ice roughness model. Since fluvial ice covers are known to undergo sub-surface erosion over time, a value near to the onset of freeze-up would be most representative. However, water levels were highly erratic and unsteady during this time. Time-series of WSE and slope upstream, downstream and at each site were generated. Uniform flow was determined to occur after a characteristic spike in water level values associated with ice cover formation, and after the time-series of water surface slopes had stabilized and become parallel. Once the date and time of the re-establishment of uniform flow was noted, the flow recorded at the WSC flow gauge and the recorded water levels associated with this time were used as forcings for the model.

Regarding the HEC-RAS model, the one-dimensional St. Venant equation is a simplification of the much more general, and much more difficult to solve three-dimensional Navier-Stokes equation. This simplification requires several assumptions. Primarily, the three-dimensional equation was first simplified to a single dimension, x, which represents the downstream ordinate. The assumption inherent in this treatment was that the fluid momentum is greatest in the downstream direction, and at the bulk scale, is responsible for the majority of the fluid behavior. This is an acceptable assumption when eddies and cross-channel shear forces, typically caused by channel obstructions or bends are not in consideration. Secondly, friction was assumed to act on the water boundaries, primarily, and internal friction of the fluid may be neglected, which is a reasonable assumption for water at normal temperatures and pressures (Sturm, 2001). This assumptions leaves the principle forces acting on the fluid to be gravity and friction. Thirdly, flow was assumed to be gradually varied throughout the study area, meaning that the water pressure distribution was assumed to be linear. Finally, it was assumed that for a reach of consistent slope, that the energy losses due to friction were the product of the friction slope and the acceleration due to gravity. For the use of the HEC-RAS model in ice-free open water applications and in the determination of

reach-based roughness, these assumptions were deemed acceptable.

In the implementation of the HEC-RAS model there were further assumptions made. Within the model, 15 reaches were defined between the WSE monitoring stations. A single Manning's n value was prescribed for each reach. This value accounted for roughness derived from the bed material, bed forms, bank vegetation, and losses due to bends. This value was then used as a calibration parameter with the observed WSE as the calibration target. This method has the potential to cause unrealistic roughness values caused by "averaging" the impact of large roughness elements across the entire reach. The reaches under consideration in this study have wide cross sections, no large obstructions, and are not tortuous; therefore, the it was decided that this was an acceptable assumption.

This methodology assumed that the bed roughness calibrated through the HEC-RAS model remained the same across all field seasons, and that this value does not change significantly with the inclusion of an ice cover. In gravel-bed rivers such as the Dauphin River, changes in the roughness of a channel may be broadly classified into the small-scale rapid changes, and large-scale slowly occurring changes. Small-scale changes to bed composition and thus roughness may occur several times in a year and are caused in part by variations in flow and ice-induced sediment transport. These changes primarily impact local hydraulics. Large-scale changes in channel roughness occur over the course of several years, and are generally caused by disruptions in flow or sediment regimes. Since the roughness values are reach-averaged, and no disruptions in the flow or sediment regimes were observed, it was reasonable to assume that at they remained constant over the two year period of this study. Anchor ice has been observed to form in this river, which would impact the bed roughness, and cross sectional area in ways that are not accounted for in this study. At the time of this research there were no practical methods to estimate the extent and impact of anchor ice on cross sectional hydraulics.

3.4.2 Model Calibration

The ice roughness model was constructed in Microsoft Excel® and used the Solver Add-In to minimize Equation 3.2 through iteration of n_i. The GRG Nonlinear solving method was used to find a solution. A convergence criteria of 0.0001 was used along with the constraint that $0.2 \geq n_i \geq 0.001$. The constraint placed on n_i was assumed to be the range of roughness values expected in a natural channel, in accordance with data provided in Chow (1959) and Nezhikhovskiy (1964). The Multistart option was enabled, with a population of 100 to increase the probability of finding a global solution. The resultant minima was also evaluated against a solution criteria of 10%. That is, if the minimal solution was within 10% of the observed flow, it may be accepted as a solution.

$$Objective = \left| \frac{1}{n_c} A^{\frac{5}{3}} P_w^{\frac{-2}{3}} S^{\frac{1}{2}} - Q_{obs} \right| \tag{3.2}$$

The HEC-RAS model was manually calibrated using MATLAB and the RASController Application Programming Interface. Manual calibration was selected due to its ease of implementation in this modeling framework. Equation 3.3 was used as an objective function for the calibration of each reach, with a target of $Objective \leq 0.1$ m. The Manning's n value for each reach was constrained to the range $0.7 \leq n \leq 0.012$ based on the range of Manning's n values expected for the beds of alluvial channels (Chow, 1959). Manning's n values were iterated to the accuracy of three significant figures. The model was calibrated for a flow condition of 86 m^3/s, which was the closest observed stable open-water flow condition to the average winter flow condition for the 2018-2019 and 2019-2020 Winter seasons.

$$Objective = |WSE_{Obs} - WSE_{Mod}| \tag{3.3}$$

3.5 Roughness Comparison

Roughness metrics were compared with the following scheme.

- **Modeled - k_s:** Modeled ice Manning's n vs. observed ice roughness height
- **Modeled - n:** Modeled ice Manning's n vs. observed ice Manning's n
- **Nez. - n:** Nezhikhovskiy ice Manning's n vs. observed ice Manning's n
- **Thick. - n:** Ice Thickness vs. observed ice Manning's n

The goal of comparing modeled and observed ice roughness was to determine the performance of ice roughness observations to those computed using the ice roughness model. This is meant to assess the applicability of roughness values determined through RPA-photogrammetry for use in hydraulic modeling. Roughness height and Manning's n values were compared separately to evaluate if the transformation of roughness height into Manning's n created differences in the data relationships. The ice Manning's n predicted through the Nezhikhovskiy relationship was also compared to observed ice Manning's n for further context of the relationship between observed roughness and a widely-used method of determining ice roughness. Finally, since ice thickness is the sole input parameter of the Nezhikhovskiy relationship, it was compared to observed ice Manning's n to determine if there may be any relationship between surface ice roughness and ice thickness. A relationship between these two parameters would indicate a relationship between surface and subsurface ice roughness. All comparisons in each item of the above scheme were plotted against the six roughness height metrics defined in Section 3.3. This resulted in four sets of six plots. A linear regression was computed for the data in each plot. The quality of regressions were evaluated using the R^2, p, and RMSE values. The criteria for significance was set to $\alpha \leq 0.05$. In the cases where Manning's n was plotted against Manning's n a 1:1 line was also plotted on the

chart, and RMSE was computed between the observed ice roughness values and their associated modeled value. The goal of the RMSE value was to evaluate the error between the six plotted metrics in each scheme. The validity of linear regression modeling to these data was evaluated by testing the normality of residuals using the Shapiro-Wilk test for normality ($p > 0.05$). This test was selected due to it's wide usage in data analysis and it's superior power to many other widely-used normality tests (Razali and Wah, 2011). Q-Q plots of residuals were used to confirmed the test statistics.

4 Results

4.1 Remotely Piloted Aircraft Performance

The RPA chosen for this study, the DJI Phantom 4 Professional®, performed well during all field visits in various weather and cloud conditions. In extreme cold (-20°C and below) the RPA performed all functions well, although the battery life was reduced by approximately 50%. Additionally, it was found that the RPA had to be powered on in a warm area, such as the heated cab of the field vehicle. Once powered on, it could then be placed outside for normal operations.

4.1.1 Accuracy of the RPA-Photogrammetry Method

The land-based accuracy test for the RPA-photogrammetry methodology conducted in La Barriere, MB produced results within the acceptable vertical error threshold of 0.1 m identified in Section 3.1.1. Table 4.1 outlines the vertical accuracy of the resultant surface in each scenario proposed in Section 3.1.1, additionally, the vertical accuracy of the tests involving rectangular cuboids was evaluated. It was clear that more than two points must be used for an accurate result; however, the data do no support the use of many more targets for increased accuracy in this research. The results of the test to determine if a lack of geo-rectification targets introduces systemic error are presented in Table 4.2.

Table 4.1: Remotely Piloted Aircraft photogrammetry accuracy test results

Test	Scenario	Vertical error (m)
Surface	All Points	0.03
	Typical Points	0.03
	Three Points	0.03
	Two Points	6.30
Rectangular Cuboids	Typical Points	0.07

Table 4.2: Percent and absolute difference between various statistical metrics computed from geo-rectified and non geo-rectified surfaces produced from data collected and site DRLL06 on 2019-11-13

Metric	Absolute	Percent
Max. (m)	0.02	4
Min. (m)	0.12	43
Mean (m)	<0.01	<1
Med. (m)	<0.01	6
IQR (m)	<0.01	2
SD (m)	<0.01	2
Skew. (-)	0.02	5
Kurt. (-)	0.08	2

4.2 Dauphin River Results

During the 2018-2019 and 2019-2020 field seasons, the Dauphin River experienced much lower flows than those observed in the previous few years. The mean seasonal flow between November and March for each season was 74 and 90 m^3/s for 2018-2019 and 2019-2020 respectively, compared to 178 and 195 m^3/s in 2016-2017 and 2017-2018 respectively, although in prior years lower flows were noted. This resulted in notably thinner ice covers, more thermal ice growth, and less extensive ice jamming than was reported by Wazney et al. (2018). Figure 4.1 displays the two years of collected top-of-ice survey data for this study (2018-2019, 2019-2020), compared to the data collected in 2016-2017. The freeze-up characteristics of the 2018-2019 and 2019-2020 seasons were very similar to one another. The toe of the ice jam was noted near DRLL08a during

both field seasons, as was observed in previous years. The leading edge of the ice jam occurred near DRLL05 during both field seasons. In previous years the leading edge had been observed to extend much further upstream. While the 2018-2019 field season was noted to be quite cold, the 2019-2020 field season was not as consistently cold. Somewhat thinner ice accumulations were noted in the 2019-2020 field season, as illustrated in Table 4.3.

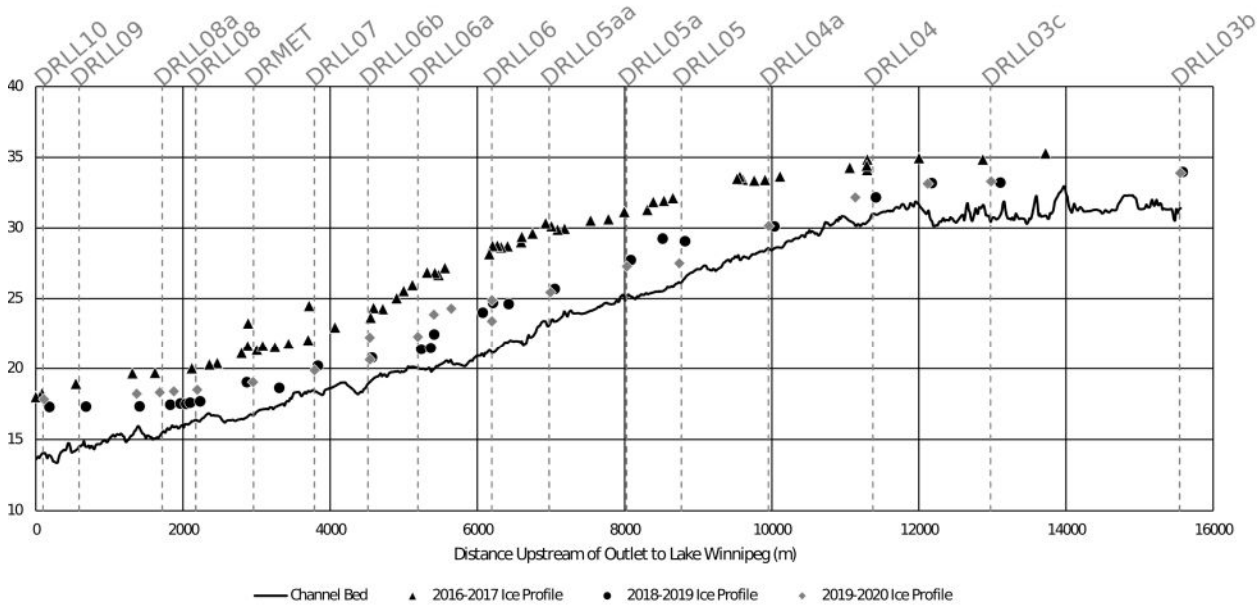

Figure 4.1: Surveyed Ice profile of the Lower Dauphin River

Table 4.3: Ice thickness, in m, 2017-2020 ([1]value estimated from photo data, [2]value transferred from nearby observation)

Site	2017-2018	2018-2019	2019-2020
DRLL03b	-	-	0.51[2]
DRLL05	2.30	2.10	0.58
DRLL06	3.44	1.56	1.04
DRLL08	-	-	0.86[2]
DRLL08a	-	1.00[1]	0.86

Additionally, for later use in Equation 2.4, the hydraulic radius, computed from the same conditions associated with the re-establishment of near-uniform flow (described in Section 3.4), adjusted for ice thickness was found using the observed water level, ice thickness, channel cross section, and assumed specific gravity of ice of 0.916. The results are presented in Table 4.4 below.

Table 4.4: Ice-affected hydraulic radius, concurrent with peak ice roughness

Site	Ice Year	R_h (m)
DRLL03b	2019-2020	0.68
DRLL05	2019-2020	0.49
DRLL06	2018-2019	0.50
DRLL06	2019-2020	0.91
DRLL08	2019-2020	0.70
DRLL08a	2017-2018	0.77
DRLL08a	2018-2019	0.38
DRLL08a	2019-2020	0.38

Only some of the observations listed in Table 3.1 were selected for further analysis. Rejected observations included those that were too small to be sub-sampled and those that produced poor quality surfaces in AgiSoft. For each site at which a roughness measurement was undertaken in a given field season, a WSE plot and a Water Surface Slope (WSS) plots were generated, which included data from stations immediately upstream and downstream. These plots are found in Appendix A, and an example of each is presented in Figures 4.2 and 4.3.

4.2.1 Application of Fast Fourier Transform to RPA-Photogrammetry Data

A comparison of the suitability of the Linear Modeling (LM) versus the combined Linear Modeling and Fast Fourier Transform (LMFFT) analysis was desired to determine if the additional computational effort was worthwhile. Both DRLL05 and DRLL06 were surveyed using the RPA-photogrammetry method on 2019-11-12 and again 2019-11-13. Field notes and pictures confirmed that the nature of the ice covers in each case underwent some minor changes between the two samples, described in Section 5.3. It was concluded that these changes were not significant enough to make the following comparison invalid. The results of this comparison are presented in Table 4.5. The LMFFT approach did not appreciably change the mean surface elevation, compared to the mean determined through the LM approach. For most other metrics the difference between

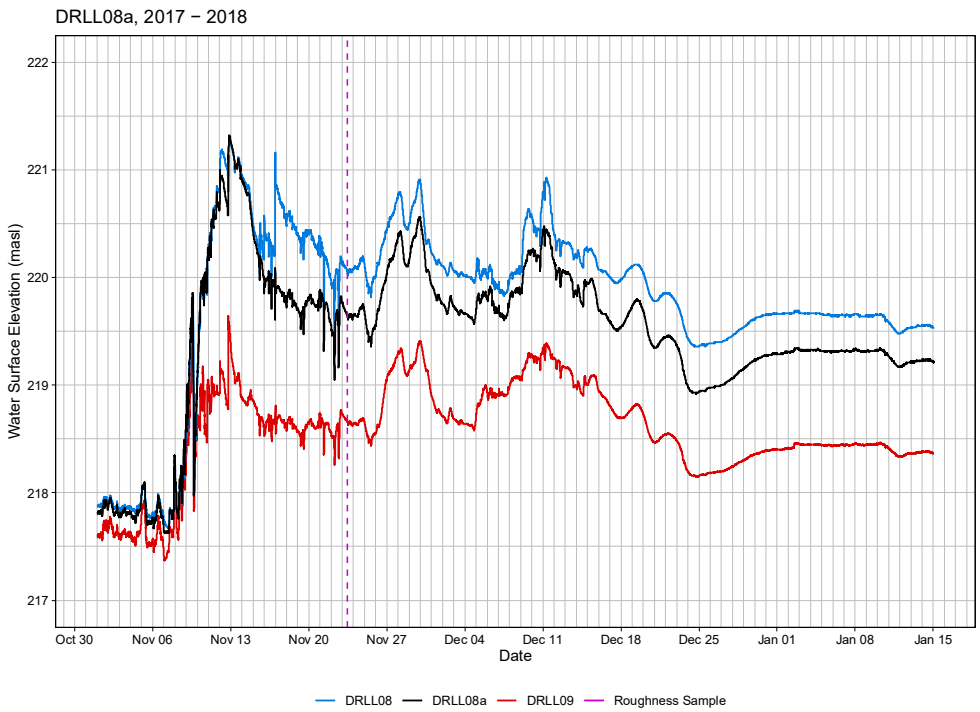

Figure 4.2: Observed WSE versus time at DRLL08a, at its surrounding stations during the 2017-2018 field season

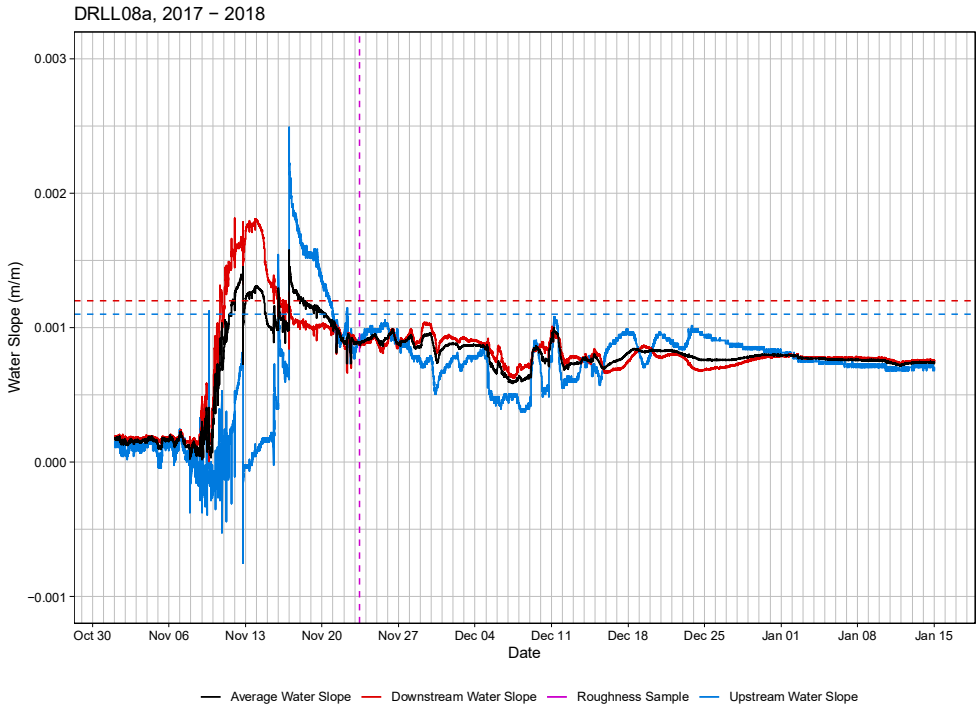

Figure 4.3: Calculated water slope versus time, upstream and downstream of DRLL08a, including the mean slope during the 2017-2018 field season

the two dates was smaller in the LMFFT scenario than the LM Scenario, which indicated that the additional post-processing improved surface representation in each test, and was suitable for use in further analyses.

Table 4.5: Percent difference between statistical metrics computed from RPA-photogrammetry data post-processed using LM and LMFFT, gathered on 2019-11-12 and 2019-11-13 at site DRLL05 and DRLL06

Metric	DRLL05		DRLL06	
	LM	LMFFT	LM	LMFFT
Max.	35.2	33.1	17.4	29.7
Min.	29.3	25.5	69.1	61.5
Avg.	0.0	0.0	0.0	0.0
Med.	69.5	24.5	65.2	38.2
IQR	83.7	2.3	8.7	12.1
SD	74.5	17.1	7.4	10.2
Skew.	16.7	7.9	84.3	34.1
Kurt.	29.4	17.7	5.7	14.8

4.2.2 Statistical Properties of Ice Roughness Height Distributions

Several different forms of ice roughness were observed in surfaces produced using RPA-photogrammetry. Figure 4.4 illustrates three different ice roughness forms and their appearance in cross section. The “rough" form of ice roughness was classified visually as any type of ice formed by the accretion and consolidation of frazil pans, but without extensive secondary formations, such as coherent compression ridges. The “smooth" form of ice roughness was classified as ice that appeared to have formed under quiescent conditions, from a combination of transported and thermally-grown ice, and did not consolidate. Ice which exhibited pressure ridges on otherwise smooth ice was termed “ridged".

Ridged ice presented a unique situation for the evaluation of ice roughness based on surface ice characteristics. In the fluvial setting it is unclear if the height of an observed pressure ridge above

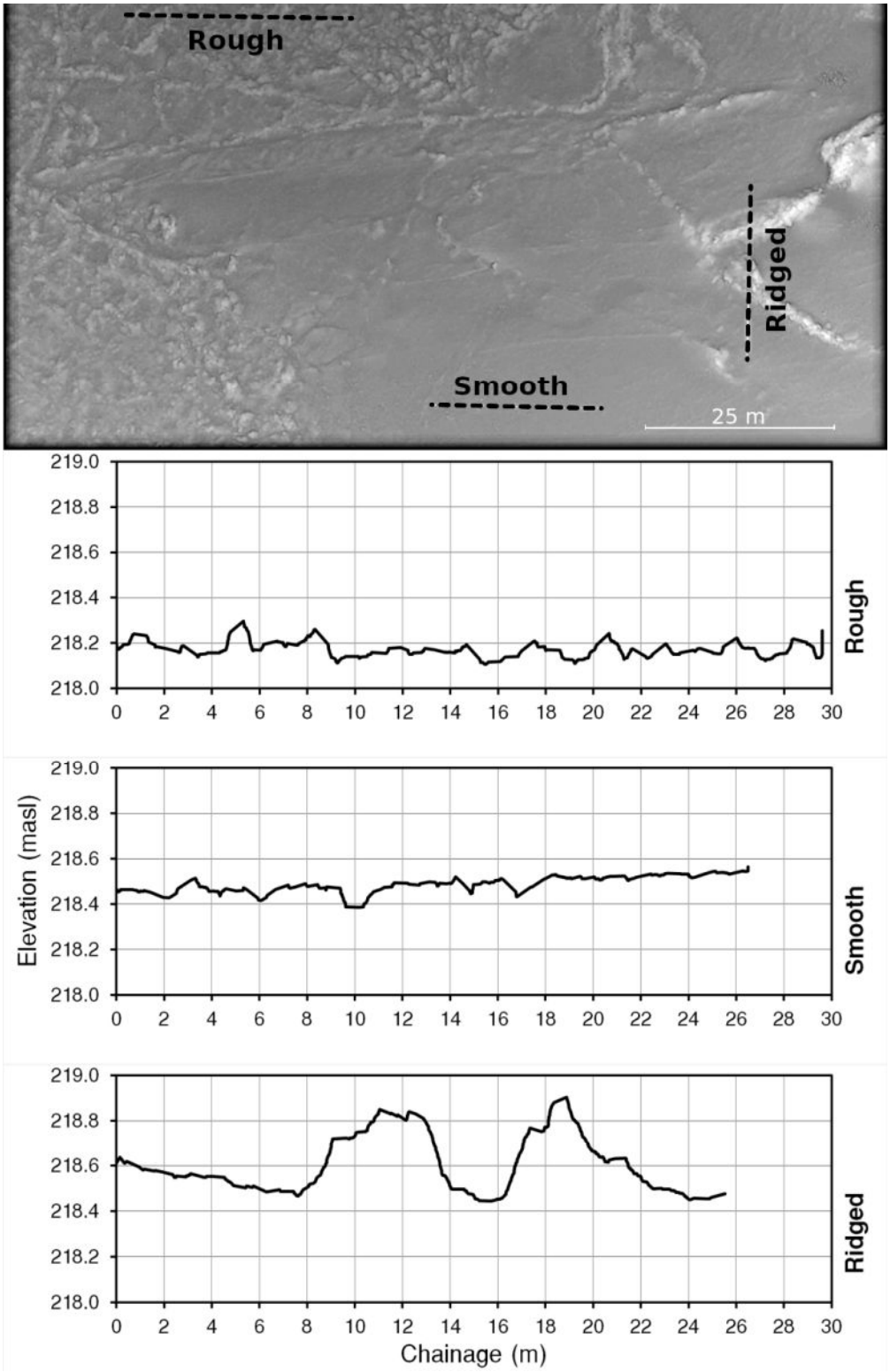

Figure 4.4: Examples of three types of roughness observed in ice surface roughness samples, DRLL08a 2019.11.13

the ice cover, known as the “sail", is indicative of the depth to which the ridge extends below the ice cover, known as the “keel". In sea ice, the keel is often greater than the sail (Johnston et al., 2009). Two samples were observed to display ridged ice, both of which occurred at site DRLL08a, on the dates 11/23/2017 and 11/26/2019. These samples were discarded from subsequent analysis.

Tables 4.6, 4.7, and 4.8 outline the results of analyses of the roughness height distributions for the raw data, the general transformed surface data, and the peak data (a subset of the general data), respectively. Histograms of the roughness height values for each test can be found in Appendix B.

Table 4.6: Statistical properties of raw surface data obtained through RPA-photogrammetry

Site	Date	Mean	Median	IQR	SD	Skew.	Kurt.
DRLL03b	11/14/2019	231.00	230.99	0.15	0.10	0.26	2.43
DRLL05	11/12/2019	295.27	295.27	1.96	1.15	0.00	1.88
DRLL05	11/13/2019	227.90	227.90	0.14	0.10	0.55	3.15
DRLL06	11/21/2018	223.80	223.76	0.20	0.17	1.13	4.14
DRLL06	2/20/2019	223.24	223.17	0.24	0.23	1.13	3.47
DRLL06	11/12/2019	285.93	285.94	0.95	0.54	-0.10	1.83
DRLL06	11/13/2019	225.15	225.14	0.22	0.15	0.27	2.81
DRLL06	11/26/2019	212.84	212.82	0.21	0.15	0.55	2.90
DRLL08	11/13/2019	218.92	218.91	0.16	0.12	0.21	2.69
DRLL08a	2/20/2019	217.95	217.96	0.27	0.14	0.06	1.62
DRLL08a	11/13/2019	218.57	218.55	0.18	0.15	0.80	4.09

Table 4.7: Statistical properties of general surface data obtained through RPA-photogrammetry

Site	Date	Mean	Median	IQR	SD	Skew.	Kurt.
DRLL03b	11/14/2019	<0.01	<0.01	0.01	0.02	2.04	15.51
DRLL05	11/12/2019	<0.01	<0.01	0.02	0.02	0.79	6.45
DRLL05	11/13/2019	<0.01	<0.01	0.02	0.02	0.73	7.59
DRLL06	11/21/2018	<0.01	-0.01	0.12	0.10	0.48	3.91
DRLL06	2/20/2019	<0.01	-0.01	0.12	0.11	0.96	5.81
DRLL06	11/12/2019	<0.01	<0.01	0.08	0.06	0.32	4.32
DRLL06	11/13/2019	<0.01	<0.01	0.08	0.07	0.44	3.68
DRLL06	11/26/2019	<0.01	<0.01	0.07	0.06	0.46	3.78
DRLL08	11/13/2019	<0.01	<0.01	0.05	0.04	0.88	5.70
DRLL08a	2/20/2019	<0.01	<0.01	0.02	0.02	0.32	6.58
DRLL08a	11/13/2019	<0.01	<0.01	0.05	0.05	0.98	6.64

Cluster analysis was conducted using K-means clustering. The optimal number of clusters was

Table 4.8: Statistical properties of peak data obtained through RPA-photogrammetry

Site	Date	Mean	Median	IQR	SD	Skew.	Kurt.
DRLL03b	11/14/2019	0.04	0.03	0.02	0.02	2.63	12.86
DRLL05	11/12/2019	0.04	0.03	0.01	0.01	2.13	9.64
DRLL05	11/13/2019	0.04	0.04	0.02	0.02	2.08	10.29
DRLL06	11/21/2018	0.25	0.23	0.08	0.06	1.46	5.67
DRLL06	2/20/2019	0.25	0.22	0.07	0.07	2.40	10.62
DRLL06	11/12/2019	0.16	0.15	0.05	0.05	2.34	11.24
DRLL06	11/13/2019	0.18	0.16	0.05	0.05	1.55	5.71
DRLL06	11/26/2019	0.15	0.14	0.04	0.04	1.99	9.38
DRLL08	11/13/2019	0.10	0.09	0.03	0.03	2.46	14.54
DRLL08a	2/20/2019	0.05	0.04	0.02	0.02	2.29	10.79
DRLL08a	11/13/2019	0.12	0.10	0.06	0.05	1.69	6.29

found to be two using average silhouette analysis. This was enforced by observations taken at the time of sample collection. The samples were broadly separated into two groups corresponding to the visual extent of “rough" or “smooth" ice, as defined earlier in this section. The cluster plot is illustrated in Figure 4.5. The resultant clusters are presented in Table 4.9. Cluster centers and within cluster sum of squares are presented in Table 4.10.

Table 4.9: Sample categorization results from K-means cluster analysis

Site	Date	Cluster
DRLL06	11/21/2018	1
DRLL06	2/20/2019	1
DRLL06	11/12/2019	1
DRLL06	11/13/2019	1
DRLL06	11/26/2019	1
DRLL03b	11/14/2019	2
DRLL05	11/12/2019	2
DRLL05	11/13/2019	2
DRLL08	11/13/2019	2
DRLL08a	2/20/2019	2
DRLL08a	11/26/2019	2

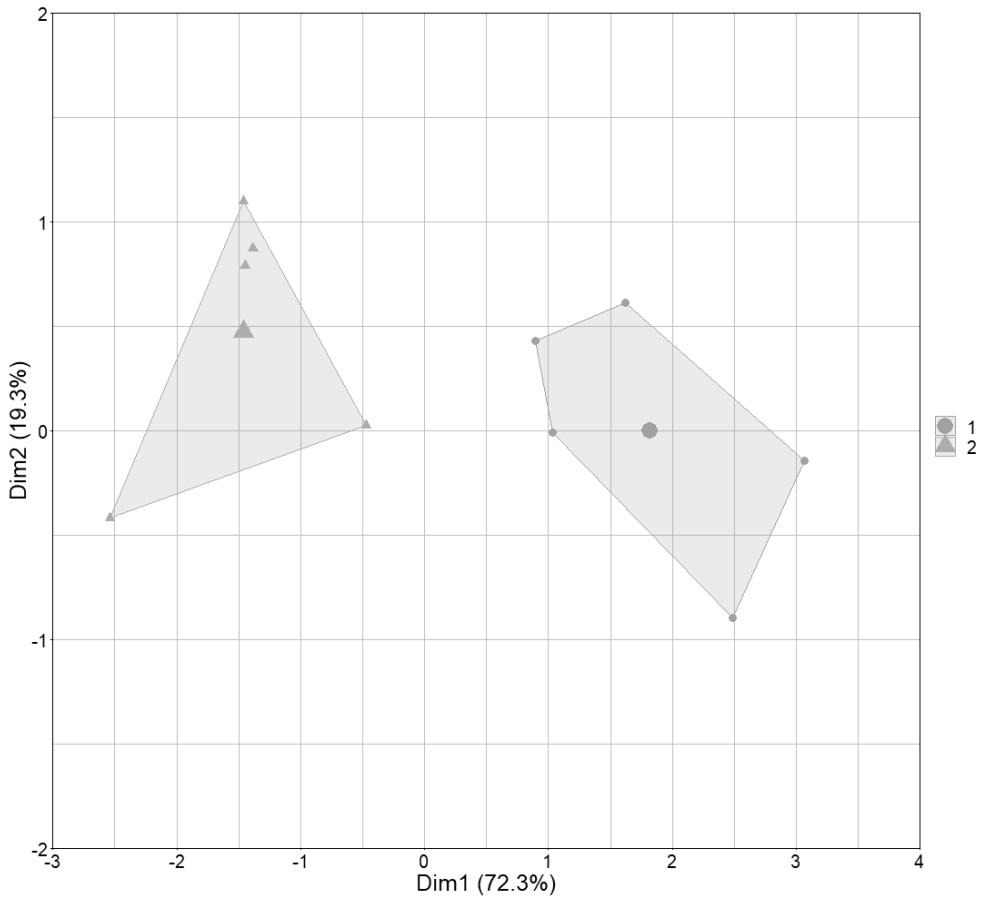

Figure 4.5: K-means clustering

Table 4.10: Cluster centers and sum of squares results

Metric	Cluster 1	Cluster 2
IQR cluster center (m)	0.09	0.03
Kurt. cluster center (-)	3.96	10.00
Med. Of Peaks cluster center (m)	0.06	0.05
IQR of Peaks cluster center (m)	0.05	0.03
Kurt. of peaks cluster center (-)	17.85	14.61
Within cluster sum of squares	5.53	14.09

4.2.3 Inverse Hydraulic Modeling

The calibration of bed roughness values using HEC-RAS was successful. Manual calibration was able to produce objective function values below the established threshold. The model's perfor-

mance is summarized in Table 4.11.

Table 4.11: HEC-RAS Manual Calibration Performance

Reach	Modeled WSE (masl)	Observed WSE (masl)	Objective (m)
1	233.29	233.27	0.02
2	232.85	232.79	0.06
3	231.56	231.64	-0.08
4	229.17	229.15	0.02
5	226.89	226.83	0.06
6	225.89	225.83	0.07
7	223.83	223.87	-0.05
8	221.95	221.88	0.07
9	220.67	220.59	0.07
10	219.72	219.81	-0.08
11	218.97	218.90	0.07
12	217.13	217.16	-0.03
13	217.09	217.13	-0.04
14	217.06	NaN	NaN
15	217.05	217.05	0.01

The calibration of ice roughness values was generally successful, a summary of the model performance is provided in 4.12. At site DRLL08a in the 2018-2019 season the lower constraint of ice roughness was enacted which prevented the model from reaching a solution within the solution criteria. The objective function was minimized to 15.9 m^3, or 20.3% of the observed flow which is above the 10% solution criteria outlined in Section 3.4.2. This data point was discarded from further analysis. The Manning's n values for bed and ice roughness values resultant from inverse hydraulic modeling are summarized in Table 4.13.

Table 4.12: HEC-RAS Manual Calibration Performance

Site	Year	Observed Flow (m^3)	Modeled Flow (m^3)	Objective (m^3)
DRLL03b	2019-2020	117.0	117.0	0.0
DRLL05	2019-2020	131.0	131.0	0.0
DRLL06	2018-2019	77.5	77.5	0.0
DRLL06	2019-2020	143.0	143.0	0.0
DRLL08	2019-2020	132.0	132.0	0.0
DRLL08a	2017-2018	171.0	171.0	0.0
DRLL08a	2018-2019	78.1	62.2	15.9
DRLL08a	2019-2020	144.0	144.0	0.0

Table 4.13: Bed and sub-surface ice Manning's roughness determined from inverse hydraulic modeling (**minimum ice roughness value used*)

Site	Ice Year	Bed	Sub-surface Ice
DRLL03b	2019-2020	0.042	0.018
DRLL05	2019-2020	0.042	0.015
DRLL06	2018-2019	0.036	0.070
DRLL06	2019-2020	0.036	0.117
DRLL08	2019-2020	0.023	0.065
DRLL08a	2017-2018	0.023	0.047
DRLL08a	2018-2019	0.023	0.010*
DRLL08a	2019-2020	0.023	0.040

5 Discussion

5.1 Accuracy of the RPA-Photogrammetry Method

Generally, if three or more targets were used, acceptable vertical and horizontal errors were observed in resultant DEMs. No excessive tilt was observed in DEMs as a result of clustering targets on one side of the study area. AgiSoft PhotoScan Professional® appeared to be able to find an adequate number of tie point between images principally comprised of snow. The rectangular cuboids maintained acceptable shape in the final DEM, as illustrated in Figure 5.1. The photogrammetry algorithm generally struggled to resolve points within forested areas. This limitation is well known within photogrammetry (Harwin and Lucieer, 2012; Hamshaw et al., 2019; Lane et al., 2000), but since there were no trees in the areas of interest of our study areas, this limitation was not consequential to the study.

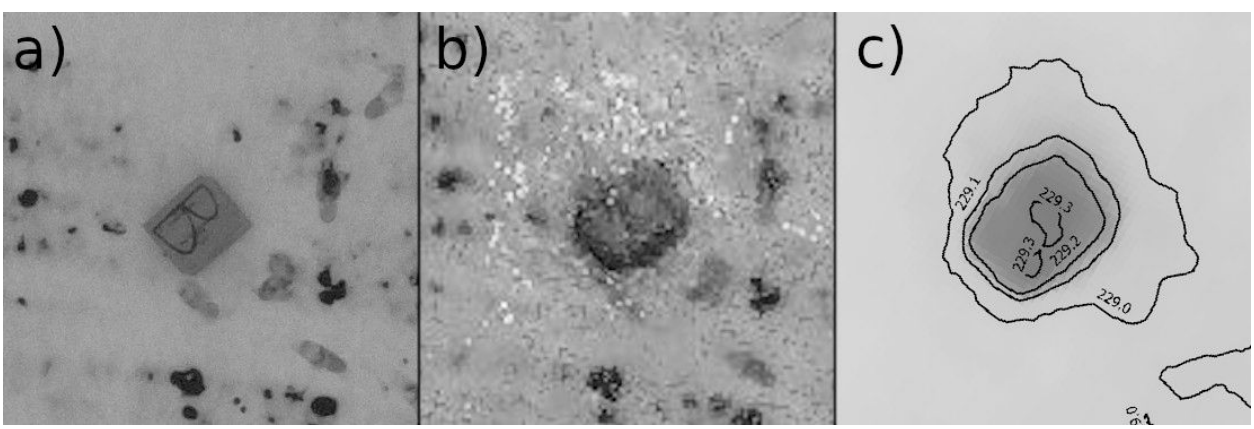

Figure 5.1: A rectangular cuboid viewed from: a) original RPA image, b) dense cloud, c) DEM

As described in Eltner et al. (2016) systemic errors causing deficiencies in surface accuracy differ from local-scale errors causing deficiencies in surface precision. Systemic errors include those incurred by improper sampling technique and by limitations in the analysis. These errors were largely assumed to have been handled to the extent that is possible in this research by the automated processes in AgiSoft PhotoScan Professional®. Eltner and Schneider (2015) found

that AgiSoft PhotoScan Professional® also performed well in reproducing the texture of complex natural surfaces. Direct comparisons could not be made in this research between the naturally occurring ice surfaces and the RPA-photogrammetry reproductions. However, the magnitude of such results as the maximum ice peak value matched visual observations and field notes. The accuracy test performed at the La Barrier field site confirmed that with appropriate ground control points this method could accurately reproduce snow surfaces. It also showed that the method could precisely reproduce features of the same order of magnitude as the chunks of ice expected to be measured on the Dauphin River.

The additional test performed to determine if systemic errors were introduced in surfaces lacking geo-rectification resulted with most metrics well within the 5% threshold. The median had percent differences greater than 5%; however, it's absolute deviation was < 0.005 m, which is much less than the expected vertical error of the survey equipment (≈ 0.1 m). The minimum value deviated by 43% and 0.12 m. This deviation puts the precision of the extreme values into question. However, since the mean, median, SD, and IQR all had deviations < 0.005 m, it was concluded that surfaces which were generated without geo-rectification targets were not subject to systematic errors which greatly impacted the precision of the overall data set.

5.2 Water Surface Elevation and Slope Plots

The WSE and WSS plots clearly showed ice jamming and consolidation events at study sites known for these processes. WSE plots showed the characteristic offset and delay of spikes attributed to surge wave movement downstream. These waves have been observed on the Lower Dauphin River by Wazney et al. (2018), and were determined to be caused by ice jamming and consolidation events. WSEs were generally observed to be higher after freeze-up, which was consistent with expectations. The following sections organize the WSE and WSS plot observations by site. The

plots are found in Appendix A.

5.2.1 DRLL03b

DRLL03b exhibited little change in both the WSE and WSS plots over the freeze-up period during the 2019-2020 field season. This site is located upstream of the break in slope between the Lower and Upper Dauphin River; it's low slope likely contributed to a slow, thermally driven freeze-up.

5.2.2 DRLL05

DRLL05 in the 2019-2020 field season exhibited typical behavior for a reach with ice dynamics. The WSE downstream of the site was observed to rise sharply two days later than at the study site. The WSE upstream was recorded to have jumped suddenly and fall again. This was recorded overnight and likely due to a flash freeze of ice pans in the system, which broke up the next day. Additionally, the upstream and downstream water slopes were observed to have lowered over the course of freeze-up. The record shows that for a moment, the slope upstream of DRLL05 was steeper than the slope downstream, indicating a possible jamming event at the site around 2019-11-11.

5.2.3 DRLL06

DRLL06 during the 2018-2019 season exhibited a delayed spike in WSE between sites DRLL06a and DRLL06. A large discrepancy was noted in the record for site DRLL05aa. This was assumed to be a momentary error in the pressure readings of the transducer. The expected peak can be seen

approximately one day after the trough following the end of discrepancy. At this site, the upstream water slope was lower after freeze-up, and vice versa for the downstream slope. This may indicate that in the 2018-2019 season, DRLL06 was the site of a constriction in flow caused by ice. Near the apex of ice dynamics, the two slopes converged around 2018-11-13. In the 2019-2020 season, ice appeared to have had a much greater impact on hydraulics than in 2018-2019, and the WSS plot showed multiple peaks, troughs, and inversions between the upstream and downstream water slope time series. However, in the end, the upstream slope reduced while the downstream slope increased, perhaps indicating that an ice-related constriction was once again formed at DRLL06. A normal pattern of delayed WSE peaks was observed during this season.

5.2.4 DRLL08 and DRLL08a

Sites DRLL08 and DRLL08a were 450 m apart, but both exhibited backwatering effects from Lake Winnipeg, and both experienced a similar ice jamming behavior. At site DRLL08, during the 2019-2020 season the WSE plot showed the expected delayed peak behavior between DRLL08 and DRLL07; however, the WSE at site DRLL08a appeared to not become elevated after freeze-up. It was also seen that the WSE of DRLL08 and DRLL08a were closely mirrored prior to freeze-up. The WSS plots indicated that the water slope became much steeper between DRLL08 and DRLL08a during freeze-up, but the slopes converged after about two weeks. DRLL08a was observed to have higher upstream and downstream water surface slopes after freeze-up than before during the 2017-2018 season, indicating backwatering was occurring upstream of this location. During the 2018-2019 and 2019-2020 seasons, however, at site DRLL08a, the upstream slope was the only one to respond to freeze-up events. During the 2019-2020 season the Levelogger® at site DRLL10 could not be retrieved, instead the Lake Winnipeg level reported by Manitoba hydro was used. While it did not capture the minute fluctuations seen in the 2018-2019 season, it was noted that the 2018-2019 data was remarkably consistent, indicating that a single lake level may

Figure 5.2: Observed WSE versus time at DRLL06 during the 2018-2019 field season

be sufficient for this analysis.

The effects of seasonal smoothing of the sub-surface of the ice cover were observed. Figure 5.2 provides an example of these observed effects. Region A represents the uniform flow conditions observed prior to ice formation. Region B shows a sharp increase in water levels associated with freeze-up jamming, and secondary consolidation previously observed by Wazney et al. (2018). Region C is the response of water levels to gradual release of the backwatering caused by the jam. Region D shows a decline in WSEs over time at a slow rate. This was thought to be partly caused by the gradual smoothing of the sub-surface of the ice cover, along with a gradual reduction of discharge as it approaches baseflow.

5.3 Statistical Properties of Ice Surface Roughness Heights

The distribution of roughness heights changed substantially through the stages of analysis. Initially, the distributions were somewhat non-normal, generally with peaks slightly to the left of the mean value (0 m), or bi-modal, such as in some cases at site DRLL08a. After the Fourier transform had been conducted, the data appeared to be more normal, with slightly less biased peaks, and more even tails. The data were tested for normality using the Shapiro-Wilk test. All tested distributions failed the Shapiro-Wilk normality test, with $p << 0.05$ (n $\approx$ 5000). However, normality tests with large sample sizes are known to be adversely affected by small departures from normality within the data set (Field, 2009). Considering the distribution of peak values only, all sites exhibited clearly non-normal distributions, heavily biased to the extreme left of the chart. This was interpreted to mean that the majority of peaks are small compared to the maximum peak values. It also means that the mean of peaks value is probably not very physically representative of the data set.

In some cases where RPA flights had been conducted at the same sites on consecutive days, differences were observed between the distributions of roughness heights and peaks. The distribution of raw and general data at sites DRLL05 changed between 2019-11-12 and 2019-11-13 (referred to as the 12th and 13th for the remainder of this paragraph). The distribution of raw data became bimodal and the distribution of general data had longer tails on the 13th. When the representative photos included in the charts were compared, it could be seen that by the 13th, the ice cover was more opaque. Water level data showed that a small consolidation event likely occurred between the two tests, presumably changing the nature of the surface ice. The peak data remained somewhat consistent, although more peaks were noted on the 13th. At site DRLL06, the tails of the distribution were longer on the 12th than the 13th, although the overall distribution shape and height were fairly consistent. Some of these differences could be explained by differences in light conditions between the RPA flights, indeed this may have given rise to some of the differences observed at

site DRLL05 over the same time period. This was corroborated by the RPA flight conducted at DRLL06 on 2019-11-26, under similar light conditions to the flight on the 13th, which showed very similar general and peak distributions. Similar general and peak distribution data were noted at site DRLL08a between the two RPA flights conducted on the 13th and 2019-11-26. The raw distributions had some noted differences in composition, although they were similar in height and width.

5.4 Comparison of Ice Roughness Estimates

In the case of site DRLL08a during the 2018-2019 monitoring year, the ice roughness model failed to produce an n_i that satisfied the constraint and solution criteria placed on the model. This data point was therefor removed in subsequent analysis.

5.4.1 Modeled - k_s

Figure 5.3 shows a comparison of the modeled ice roughness to various metrics of representative surface roughness height values, as outlined in Table 3.3. In general, at sites where rougher ice was predicted by the model, most roughness height metrics were also greater, indicating a rougher ice surface. Linear regressions were computed for all metrics and are illustrated in their corresponding graphs. The parameters of these regressions are presented in Table 5.1. The R^2 values indicated that the best fitting relationship was found with the maximum peak metric. The author hesitates to suggest this as the most representative metric, since maximum values can be heavily influenced by outliers in the distribution. The p values show that none of the linear regressions were significant, although there is still indication of correlation.

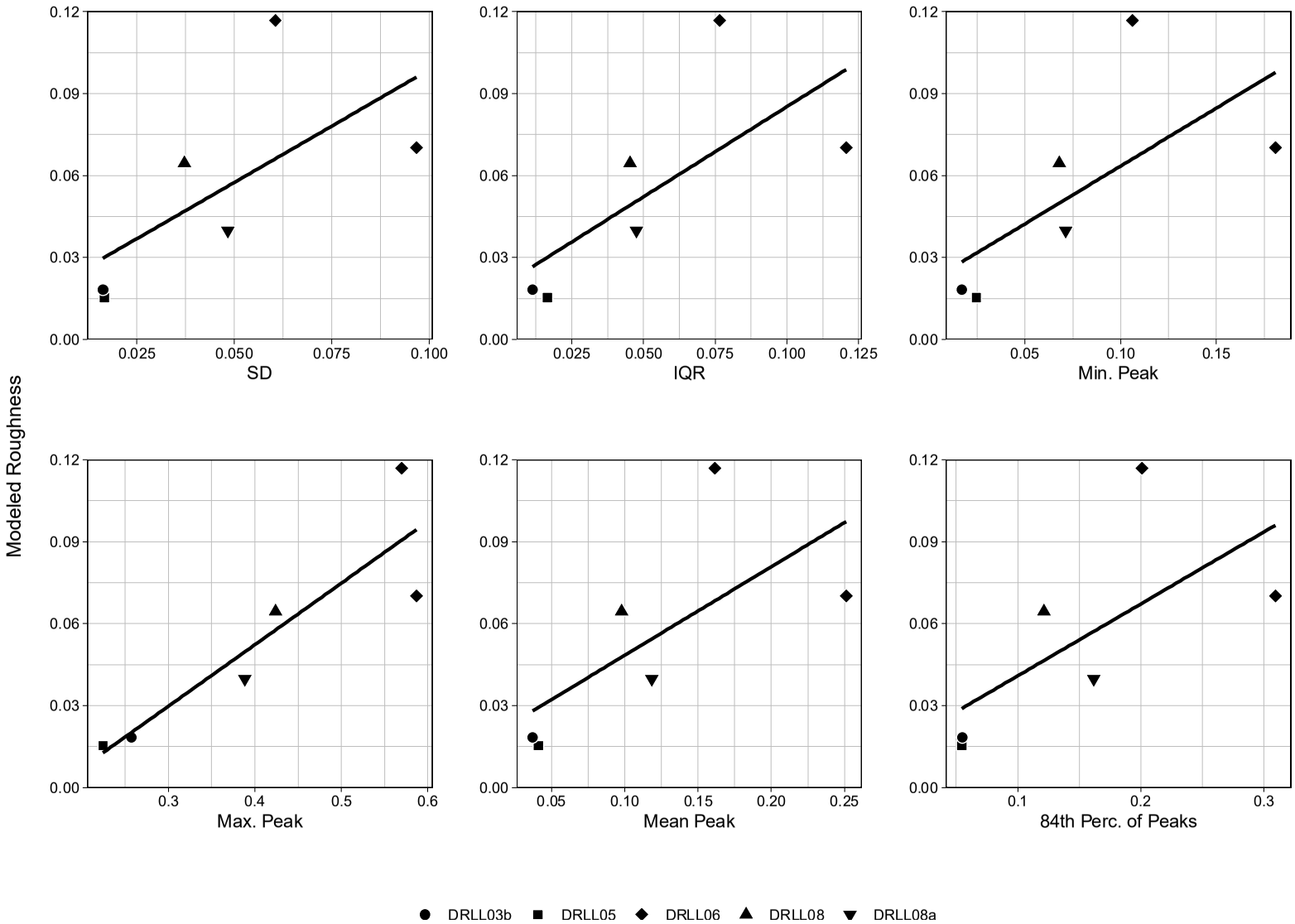

Figure 5.3: Comparison of modeled roughness to various metrics of representative roughness heights of sampled surfaces

5.4.2 Modeled - n

Figure 5.4 compares the modeled roughness to roughness values derived from the above representative statistical metrics of roughness height, which have then been converted to Manning's n values using Equation 2.4. The data showed a general trend where ice that was observed to be rough through RPA-photogrammetry was also predicted to have a rough sub-surface through inverse hydraulic modeling. However, the RPA-photogrammetry method generally produced lower roughness values than those determined through modeling. In all cases, one point at the upper boundary of each plot, associated with DRLL06, fell outside of the expected trend, with a modeled ice roughness much higher than the observed RPA-photogrammetry roughness. Table 5.2 summarizes the root-mean-square error (RMSE) between the observed and modeled roughness. Excluding the maximum peak metric, the 84th percentile of peak produced the best fit for this data, based on RMSE. Linear regressions were computed for all metrics and are illustrated in their corresponding graphs. The parameters of these regressions are presented in Table 5.1. On the basis of the R^2 value of the linear regression, the maximum peak metric again had the highest value. The p statistic also reports that this was also the only significant ($\alpha \leq 0.05$) relationship of the metrics tested. These data also show that the conversion of observed roughness height values to Manning's n resulted in little change in the nature of the relationship between observed and modeled roughness. RMSE values were typically much lower in the linear regressions computed for the Modeled - n scenario.

As noted by Beltaos (2013) ice-covered flow gauging is notoriously difficult, and subject to considerable error. On the Dauphin RiverWazney et al. (2019a) calculated instantaneous discharges several times greater than the recorded value at the WSC gauge due to ice jam release events. The observed ice-affected flow reported by the WSC was the primary calibration target for this analysis, and almost certainly much smaller than the instantaneous discharge caused by ice consolidation events, making it an obvious source of potential error. If the true instantaneous discharge had been

known, and used, these results would have been quite different. It is also possible that the conducted modeling was simply not detailed enough to account for the complicated ice and hydraulic processes occurring at these study sites. The choice to use at-a-station one-dimensional modeling was based on difficulties encountered with the more sophisticated HEC-RAS modeling platform, with the hope of a simpler model being better able to capture bulk hydraulic behavior in a simpler process. These results indicate that the modeling approach taken may not be sufficient, and a more detailed approach may be required. A possible and obvious candidate would be the CRISSP-2D finite element model, which has been applied to the Dauphin River by Wazney et al. (2019b).

5.4.3 Nez. - n

In Figure 5.5 the Manning's n determined by using the various representative roughness height metrics were compared to the Manning's n calculated using Equation 2.3. These plots show that ice that was predicted to have a rougher sub-surface via the Nezhikhovskiy relationship also had a rougher surface, as observed using RPA-photogrammetry. Table 5.2 summarizes the RMSE between the observed roughness and roughness determined through the Nezhikhovskiy relationship. The maximum peak height metric had, by far, the best fit based on the RMSE between the two metrics. As noted earlier, the maximum peak metric is prone to influence from outliers. With this in mind, the 84th percentile of peaks had the next lowest RMSE between observed and modeled values. Linear regressions were computed for all metrics and are illustrated in their corresponding graphs. The parameters of these regressions are presented in Table 5.1. The RMSE between the data and the linear regression showed a less clear distinction, with all models performing well, although the SD and IQR had the lowest RMSE values. Considering the R^2 value of the linear regressions, the IQR had the highest value, although all models performed much better than in the Modeled - k_s and Modeled - n scenarios. The p statistic found that all relationships were significant ($\alpha \leq 0.05$) in this comparison. These results indicate the the ice roughness values derived

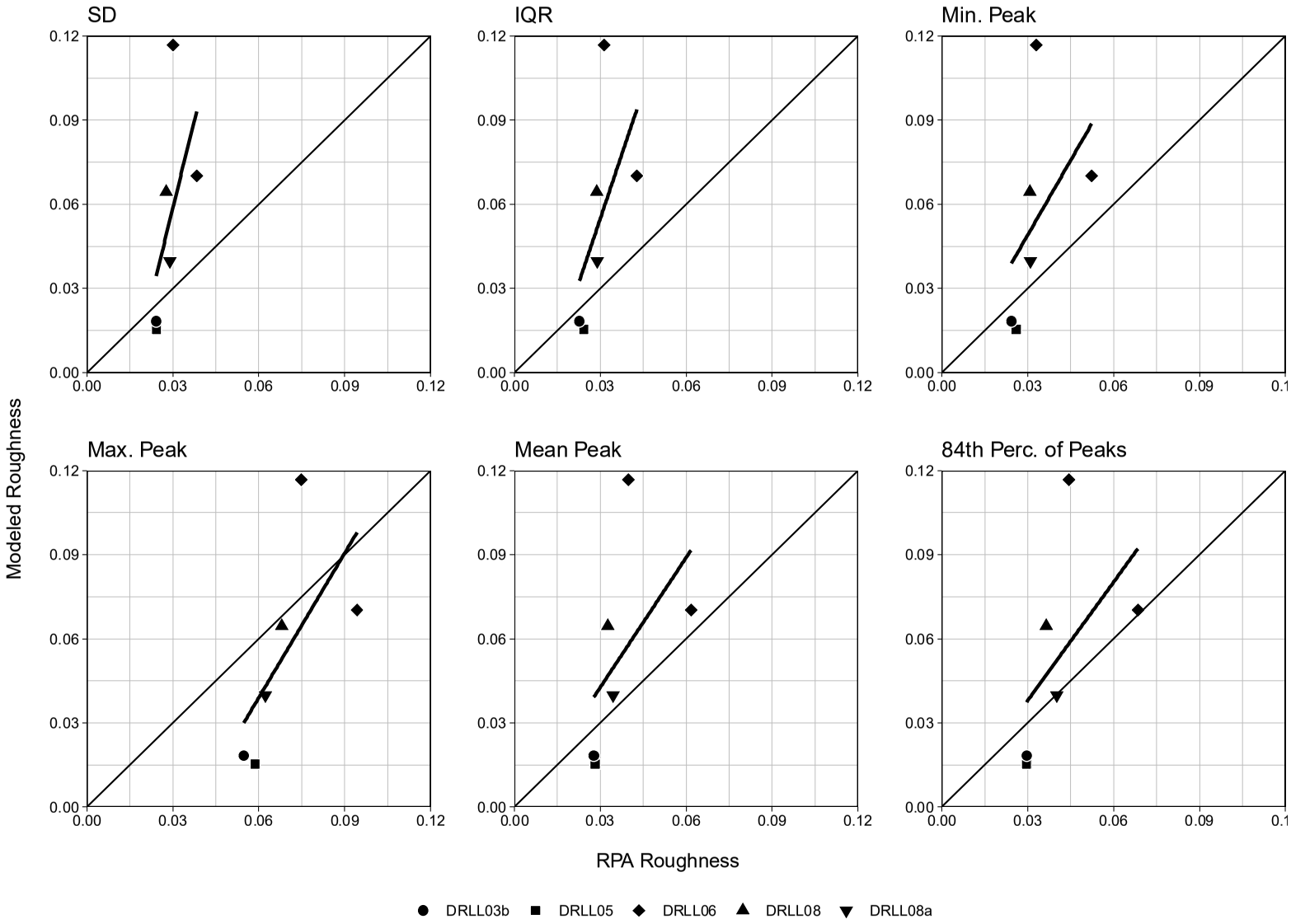

Figure 5.4: Comparison of modeled roughness to observed Manning's ice roughness computed using various metrics of representative surface roughness height

from RPA-photogrammetry closely match roughness values predicted using the Nezhikhovskiy relationship. Given the wide use of the Nezhikhovskiy relationship, this may indicate that it is a more robust ice roughness predictor than the ice roughness model produced in this thesis.

5.4.4 Thickness - n

Since the only input parameter for the Nezhikhovskiy relationship is ice thickness, Figure 5.5 suggests a relationship between ice thickness and surface roughness. Since the original observations that support the Nezhikhovskiy (1964) equation related thicker ice to ice with a rougher sub-surface, the link between surface ice roughness and ice thickness supports a link between surface and sub-surface ice roughness. Pursuant to the idea of a linkage between surface ice roughness and thickness, the observed Manning's ice roughness was compared to the observed ice thickness in Figure 5.6. Linear regressions were computed for all metrics and are illustrated in their corresponding graphs. The parameters of these regressions are presented in Table 5.1. All metrics showed a strong positive relationship with ice thickness. The IQR again performed the best with the highest R^2 value and lowest RMSE, although all metrics performed exceptionally well. The p statistic shows that all relationships were significant ($\alpha \leq 0.05$) in this comparison. Further research would be required to determine if this relationship may be used to estimate ice thickness based on observed surface roughness.

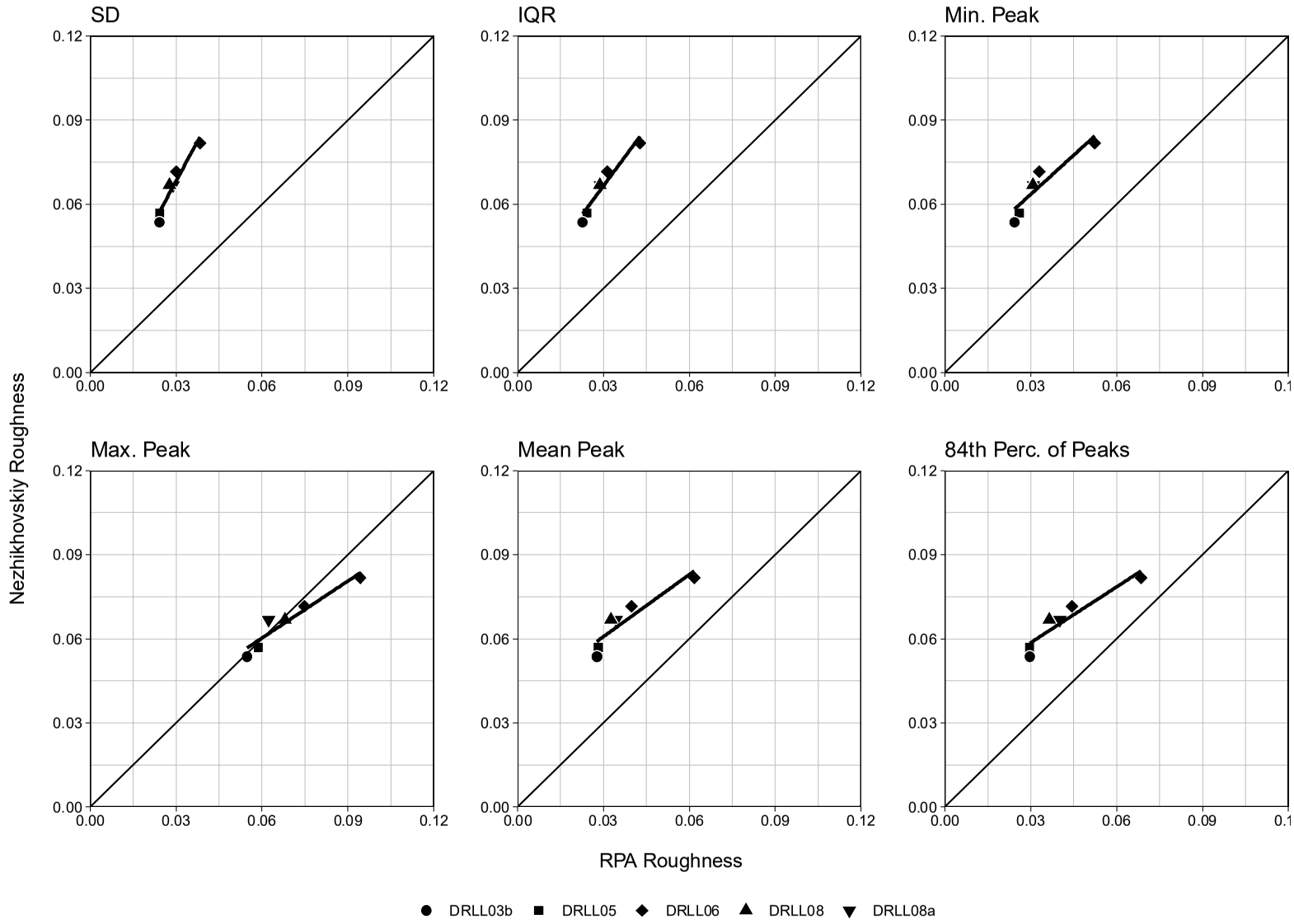

Figure 5.5: Comparison of observed Manning's ice roughness calculated from various metrics to calculated Manning's ice roughness using the Nezhikhovskiy relationship

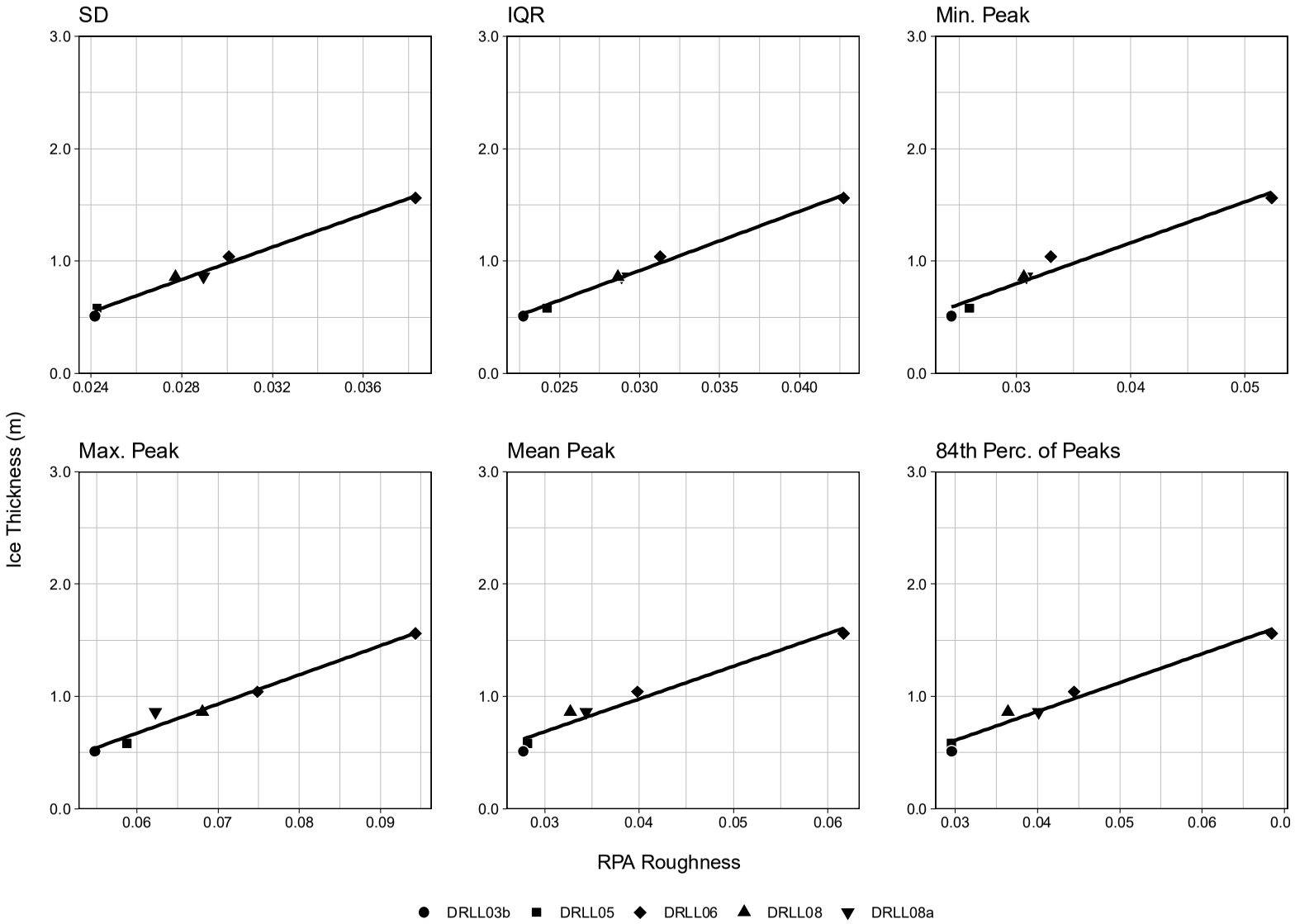

Figure 5.6: Comparison of observed Manning's ice roughness calculated from various metrics to observed ice thickness

5.4.5 Statistical Results

The statistical parameters of each linear regression are presented in Table 5.1. Additionally RMSE between observed and modeled roughness in the Modeled - n and Nez. - n scenario is found in Table 5.2.

Table 5.1: Performance statistics of applied linear models

Model	Metric	y	m	R^2	$F_{1,4}$	p	RMSE
Modeled - k_s	SD	0.018	0.522	0.430	1.884	0.242	0.021
	IQR	0.012	0.751	0.496	1.909	0.239	0.026
	Min. Peak	0.021	1.052	0.445	1.132	0.347	0.041
	Max. Peak	0.215	3.565	0.803	2.855	0.166	0.062
	Mean Peak	0.040	1.446	0.469	1.428	0.298	0.054
	84th of Peaks	0.058	1.702	0.448	1.593	0.275	0.066
Modeled - n	SD	0.025	0.077	0.320	3.019	0.157	0.004
	IQR	0.024	0.106	0.323	3.935	0.118	0.005
	Min. Peak	0.026	0.124	0.221	3.212	0.148	0.008
	Max. Peak	0.056	0.242	0.417	16.312	0.016	0.010
	Mean Peak	0.028	0.170	0.263	3.532	0.133	0.010
	84th of Peaks	0.030	0.202	0.285	3.247	0.275	0.011
Nez. - n	SD	-0.004	0.492	0.930	53.217	0.002	0.001
	IQR	-0.015	0.674	0.933	55.283	0.002	0.002
	Min. Peak	-0.028	0.916	0.853	23.295	0.008	0.004
	Max. Peak	-0.020	1.343	0.910	40.431	0.003	0.004
	Mean Peak	-0.039	1.148	0.849	22.466	0.009	0.005
	84th of Peaks	-0.047	1.339	0.887	31.439	0.005	0.004
Thick. - n	SD	0.017	0.014	0.986	284.096	<0.000	0.001
	IQR	0.013	0.019	0.992	496.959	<0.001	0.001
	Min. Peak	0.009	0.026	0.953	81.092	0.001	0.002
	Max. Peak	0.035	0.037	0.970	128.176	<0.001	0.002
	Mean Peak	0.008	0.033	0.954	82.852	0.001	0.002
	84th of Peaks	0.007	0.038	0.971	135.185	<0.001	0.002

Using the results of the K-means clustering analysis, a breakdown of ice roughness cluster characteristics was generated. Table 5.3 illustrates the site grouping under the cluster analysis results, with maximum, mean, and minimum values reported within each cluster. The two best performing roughness metrics in the above subsections, IQR and 84th percentile of peaks are included, as

Table 5.2: RMSE between observed surface ice roughness and modeled subsurface ice roughness, errors are in the units of Manning's n

Metric	Modeled - n	Nez. - n
SD	0.041	0.038
IQR	0.040	0.037
Min. Peak	0.038	0.033
Max. Peak	0.032	0.006
Mean Peak	0.035	0.029
84th of Peaks	0.033	0.025

well as the strongest defining metrics in the principal components analysis, IQR and kurtosis are included in this table. This table may serve as a defining guide for further categorization of ice surface types. Since cluster 1 corresponded to ice surfaces with higher IQR and 84th percentile of peaks values, this group was interpreted as the "rough" ice group. Consequently, cluster 2 was termed "smooth". The range of values are mostly mutually exclusive, indicating a strong divide between the two groups.

Table 5.3: Categorization of ice roughness via cluster analysis and associated summary statistics

Site	Date	Cluster	General Data		Peak Data			
			IQR (m)	Kurt. (-)	Median (m)	IQR (m)	Kurt. (-)	84th Perc. (m)
DRLL06	11/21/2018	1	0.121	3.910	0.234	0.078	5.669	0.309
DRLL06	2/20/2019	1	0.121	5.812	0.223	0.074	10.622	0.308
DRLL06	11/12/2019	1	0.075	4.317	0.145	0.052	11.239	0.199
DRLL06	11/13/2019	1	0.084	3.678	0.162	0.055	5.714	0.217
DRLL06	11/26/2019	1	0.071	3.776	0.138	0.045	9.375	0.182
DRLL03b	11/14/2019	2	0.011	15.512	0.028	0.022	12.856	0.055
DRLL05	11/12/2019	2	0.017	6.453	0.035	0.015	9.640	0.050
DRLL05	11/13/2019	2	0.016	7.593	0.037	0.021	10.285	0.059
DRLL08	11/13/2019	2	0.045	5.701	0.088	0.032	14.538	0.121
DRLL08a	2/20/2019	2	0.020	6.582	0.042	0.017	10.789	0.061
DRLL08a	11/26/2019	2	0.039	10.672	0.079	0.032	29.543	0.114
Max.		1	0.121	5.812	0.234	0.078	11.239	0.309
		2	0.045	15.512	0.088	0.032	29.543	0.121
Mean		1	0.094	4.299	0.181	0.061	8.524	0.243
		2	0.025	8.752	0.051	0.023	14.609	0.077
Min.		1	0.071	3.678	0.138	0.045	5.669	0.182
		2	0.011	5.701	0.028	0.015	9.640	0.050

5.5 Alternative Uses for RPA-Photogrammetry

A common problem in river ice elevation surveys is the selection of a single, representative value to define the average ice surface elevation in a given area. It is up to the observer to use their best judgment to visually select a single representative point to survey while walking along the river bank. During massive ice jam events, this field task is dangerous, and frequently impossible. The above research shows that RPA-photogrammetry can be used to accurately survey ice areas for the purpose of observing local topography, with much lower risks to field personnel than traditional ice surveying methods. Once a DEM has been established, a representative ice elevation value can be determined using linear modeling. From an appropriately selected sub-area, a linearly-defined plane-of-best-fit may be determined, the mean value of which would provide an excellent estimation of a locally representative ice elevation. This analysis could be extended to examine shear walls, and determine maximum ice elevation of a freeze-up jam, after the fact.

6 Conclusions

The research presented in this thesis has developed novel methods for the capture of fluvial ice surface roughness and the analysis of the resultant high-resolution data. Through field trials, and controlled land-based experiments, it was determined that RPA-photogrammetry produced an accurate digital representation of rough or smooth ice covers, with an mean vertical error of 0.03 m if using three or more ground control points over a 200 m by 100 m area. For the sole purpose of roughness characterization, it was determined that geo-rectification were unnecessary using our equipment. Further, I have found that a consumer-grade RPA was able to operate in harsh winter field conditions, with an approximately 50% reduced battery life. Using this novel, high-resolution data, bulk statistical properties including SD, skewness, kurtosis, and IQR were calculated for two classifications of ice covers. These properties were compared to results from inverse hydraulic modeling, with mixed success. Comparisons were also made between surface ice roughness parameters and ice roughness predicted with the Nezhikhovskiy relationship, which showed promising results.

The hypothesis of this research, that at the time of freeze-up the roughness of the surface of a fluvial ice cover will have some relationship to the roughness of the sub-surface was tested. Four comparison schemes were evaluated, including comparison of: Manning's n determined through inverse hydraulic modeling and roughness height observed through RPA-photogrammetry, Manning's n determined through inverse hydraulic modeling and roughness observed through RPA-photogrammetry assessed as Manning's n, Manning's n determined through the Nezhikhovskiy relationship and roughness observed through RPA-photogrammetry assessed as Manning's n, and ice thickness and roughness observed through RPA-photogrammetry assessed as Manning's n. Each scheme compared the first listed parameter with six selected roughness height metrics. Linear regressions were computed for all comparisons. A general increasing trend was observed when comparing sub-surface ice roughness determined through inverse modeling and surface ice

roughness height observed via RPA-photogrammetry, with the maximum peak value producing the highest correlation relationship. Through comparison of Manning's n values produced by the ice roughness model and through RPA-photogrammetry, the maximum peak value again produced the highest correlation relationship. It was also the only significant relationship found in the first two comparison schemes ($\alpha \leq 0.05$). While the maximum peak value performed well with these data, it was concluded to be unreliable for general use due to the influence of outliers on this value. The next best performing metric was the IQR, which also had one of the lowest observed RMSE values. It was concluded that the modeling approach taken herein was likely not sophisticated enough. The CRISSP-2D model, which has been used on the Lower Dauphin River in previous studies, may be more suitable for further analyses.

When comparing the results of the results of the Nezhikhovskiy relationship to the Manning's n values determined through RPA-photogrammetry, a much better fit was found. All roughness height metrics produced significant relationships, many with $R^2 > 0.9$. In this comparison the IQR had the lowest p value and highest R^2 of 0.933 and 0.002 respectively. Only the SD had a lower RMSE value of the linear regression with values of 0.001 and 0.002 respectively. Aside from the maximum peak value, the 84th percentile of peaks values had the lowest RMSE when compared to the 1:1 line.

Very strong, positive relationships were observed between surface roughness and ice thickness. Once again the IQR performed the best with the highest R^2 and lowest RMSE and p values (0.992, < 0.001, and 0.001 respectively). This relationship provides the basis for a link between surface and sub-surface ice roughness, through the Nezhikhovskiy relationship.

Through evaluation of the statistical properties of the distribution of surface heights observed via RPA-photogrammetry, several interesting patterns were found. All distributions were found to be non-normal, when evaluated with the Shapiro-Wilk normality test. The IQR for these cases

were often very similar. K-means cluster analysis displayed two strong groupings, one comprised of DRLL06, and the other of DRLL03b, DRLL05, DRLL08, and DRLL08a. Based on field observations the first group was labeled “rough" ice, while the second was labeled “smooth" ice. The range of IQR values observed in each group was 0.07 - 0.12 m and 0.01 - 0.05 for the rough and smooth groups respectively.

This research would benefit from a more thorough treatment of the inverse hydraulic modeling component. However, detailed hydraulic modeling of fluvial ice covers is still an evolving field, and requires much research and refinement in its own right. A higher degree of confidence in the flow data, perhaps through manual measurements, would further benefit the current modeling approach, and any subsequent efforts. More field data would help to further define the relationship between the tested roughness characterization metrics, their resultant Manning’s n values, and the modeled ice roughness values. Of particular interest may be the association of surface ice roughness and ice thickness measurements.

Finally, the methods presented in this research can conceivably be applied to further uses in the field of fluvial ice monitoring. The high-resolution surfaces produced by this method, and retrodictive nature of the data provide ample opportunity for the development of novel analysis methods, and the replacement of traditional techniques. Ice profile surveys may be aided by using RPA-photogrammetry to determine a more representative plane-of-best-fit for a spot measurement of ice elevation. Shear walls may be captured and analyzed in their entirety, even immediately after, or during break-up. This research also presents a possible link between surface ice roughness and ice thickness, which may provide for a method of estimating ice thickness using RPA-photogrammetry. The use of RPA-photogrammetry for the monitoring of fluvial ice covers offers a quicker, safer, and cheaper alternative to any previous method of high-resolution topographic data collection, and it’s applications are open for development.

7 References

Aberle, J. and Nikora, V. (2006). Statistical properties of armored gravel bed surfaces. *Water Resources Research*, 42.

Alfredsen, K., Haas, C., Tuhtan, J. A., and Zinke, P. (2018). Brief communication: Mapping river ice using drones and structure from motion. *The Cryosphere*, 12:627–633.

Ashton, G. D., editor (1986). *River and lake ice engineering*. Water Resources Publication.

Beltaos, S. (2002). Effects of climate on mid-winter ice jams. *Hydrological Processes*, 16:789–804.

Beltaos, S., editor (2013). *River Ice Formation*. The Committee on River Ice Processes and the Environment.

Bisaillon, J.-F. and Bergeron, N. E. (2009). Modeling anchor ice presence-absence in gravel bed rivers. *Cold Regions Science and Technology*, 55.

Buffin-Belanger, T., Demers, S., and Olsen, T. (2015). Quantification of under ice cover roughness. In *18th Workshop on the Hydraulics of Ice Covered Rivers*, Quebec City, QC, Canada. CGU HS Committee on River Ice Processes and the Environment.

Chow, V. T. (1959). *Open Channel Hydraulics*. McGraw Hill.

Clark, R. L. and Lee, R. (1998). Development of topographic maps for precision farming with kinematic gps. *American Society of Agricultural and Biological Engineers*, 41(4):909–916.

Colomina, I. and Molina, P. (2014). Unmanned aerial systems for photogrammetry and remote sensing: A review. *ISPRS Jounral of Photogrammetry and Remote Sensing*, 92:79–97.

Crance, M.-J. and Frothingham, K. M. (2008). The impact of ice cover roughness on stream hydrology. In *65th Eastern Snow Conference*, pages 149–165, Fairlee, Vermont, USA.

Eisenbeiss, H., Lambers, K., and Sauerbrier, M. (2005). Photogrammetric recording of the archaeological site of pinchango alto (palpa, peru) using a mini helicopter (uav). In Figueiredo, A., editor, *The world is in your eyes: CAA 2005: Computer Applications and Quantitative Methods in Archaeology, proceedings of the 33rd Conference*, pages 175–184.

Eltner, A., Kaiser, A., Castillo, C., Rock, G., Neugirg, F., and Abellan, A. (2016). Image-based surface reconstruction in geomorphometry - merits, limits and developments. *Earth Surface Dynamics*, 4:359–389.

Eltner, A. and Schneider, D. (2015). Analysis of different methods for 3d reconstruction of natural surfaces from parallel-axes uav images. *The Photogrammetric Record*, 30(151):279–299.

Field, A. (2009). *Discovering statistics using SPSS*. SAGE Publications, Los Angeles, 3 edition.

Fraser, C. S. and Cronk, S. (2009). A hybrid measurement approach for close-range photogrammetry. *ISPRS Journal of Photogrammetry and Remote Sensing*, (64):328–333.

Gadelmawla, E. S., Koura, M. M., Maksoud, T. M. A., Elewa, I. M., and Soliman, H. H. (2002). Roughness parameters. *Journal of Materials Processing Technology*, 123:133–145.

Gerard, R. and Andres, D. (1984). Hydraulic roughness of freeze-up ice accumulations: North sasksatchewan river through edmonton. pages 62–86.

Gini, R., Pagliari, D., Passoni, D., Pinto, L., Sona, G., and Dosso, P. (2013). Uav photogrammetry: Block triangulation comparisons. *Internation Archives of the Photogrammetry, Remote Sensing and Spatial Information Sciences*, XL-1/W2:157–162.

Gomez, B. (1993). Roughness of stable, armored gravel beds. *Water Resources Research*, 29(11):3631–3642.

Hamshaw, S. D., Engel, T., Rizzo, D. M., O'Neil-Dunne, J., and Dewoolkar, M. M. (2019). Application of unmanned aircraft system (uas) for monitoring bank erosion along river corridors. *Geomatics, Natural Hazards and Risk*, 10(1):1285–1305.

Harwin, S. and Lucieer, A. (2012). Assessing the accuracy of georeferenced point clouds produced via multi-view stereopsis from unmanned aerial vehicle (uav) imagery. *Remote Sensing*, 4:1573–1599.

Jain, A. K. (2010). Data clustering: 50 years beyond k-means. *Pattern Recognition Letters*, 31:651–666.

James, M. R., Antoniazza, G., Robson, S., and Lane, S. N. (2020). Mitigating systemic error in topographic models dfor geomorphic change detection: accuracy, precision and considerations beyond off-nadir imagery. *Earth Surface Processes and Landforms*, 45:2251–2271.

James, M. R. and Robson, S. (2014). Mitigating systemic error in topographic models dervied from uav and ground-based image networks. *Earth Surface Processes and Landforms*, 39:1413–1420.

Johnson, C. E. and Barton, C. C. (2004). Where in the world are my field plots? using gps effectively in environmental field studies. *Frontiers of Ecology and the Environment*, 2(9):475–482.

Johnston, M., Masterdon, D., and Wright, B. (2009). Multi-year ice thickness: Knowns and unknowns. In *Proceedings of the International Conference on Port and Ocean Engineering Under Arctic Conditions*, pages 969–981.

Julien, P. Y. (2002). *River Mechanics*. Cambridge University Press, 1st edition.

Kienapple, K. (2017). *Aerobotika RPAS Ground School Text Book*. Aerobotika Aerial Intelligence, 1.01 edition.

Lane, S. N., James, T. D., and Crowell, M. D. (2000). Application of digital photogrammetry to complex topography for geomorphological research. *Photogrammetric Record*, 16(95):793–821.

Lane, S. N., Richards, K. S., and H., C. J. (1993). Development in photogrammetry; the geomorphological potential. *Progress in Physcial Geography*, 17(3):306–328.

Liu, H. and Jezek, K. C. (1999). Investigating dem error patterns by directional variograms and fourier analysis. *Geographical Analysis*, 31(3):249–266.

Lowe, D. G. (2004). Distinctive image features from scale-invariant keypoints. *Internation Journal od Computer Vision*, 60(2):91–110.

MacDonald, M. K., Stadnyk, T. A., Dery, S. J., Braun, M., Gustafsson, D., Isberg, K., and Arheimer, B. (2018). Impacts of 1.5 and 2.0 c warming on pan-arctic river discharge into the hudson bay complex through 2070. *American Geophysical Union: Geophysical Reserach Letters*, pages 7561–7570.

Matousek, V. (1984). Types of ice run and conditions for their formation. In *IAHR International Symposium on Ice*, volume 1, pages 315–327, Hamburg, Germany.

Matthews, N. A. (2008). Aerial and close-range photogrammetric technology: providing resource documentation, interpretation, and preservation. Technical Report 428, Bureau of Land Management, Denver, Colorado.

Nezhikhovskiy, R. A. (1964). Coefficients of roughness of bottom surface on slush-ice cover. *Sovient Hydrology*, pages 127–150.

Niethammer, U., James, M., Rothmund, S., Travelletti, J., and Joswig, M. (2012). Uav-based remote sensing of the super-sauze landslide: Evaluation and results. *Engineering Geology*, 128:2–11.

Nikora, V. I., Goring, D. G., and Biggs, B. J. F. (1998). On gravel-bed roughness characterization. *Water Resources Research*, 34(3):517–527.

Nikuradse, J. (1950). Laws of flow in rough pipes. Technical Memorandum 1292, National Advisory Committee for Aeronautics.

Poon, C. Y. and Bhushan, B. (1995). Comparison of surface roughness measurements by stylus profiler, afm and non-contact optical profiler. *Wear*, 190:76–88.

Razali, N. M. and Wah, Y. B. (2011). Power comparisons of shapiro0wilk, komolgorov-smirnov, lilliefors and anderson-darling tests. *Journal of Statistical Modeling and Analytics*, 2(1):21–33.

Smith, S. W. (1997). *The Scientist and Engineer's Guide to Digital Signal Processing*. California Technical Publishing, San Diego, CA.

Snavely, N. (2009). *Scene reconstruction and visualization from internet photo collections*. PhD thesis, University of Washington, USA.

Strickler, A. (1923). Contributions to the question of a velocity formula and roughness data for streams, channels and closed pipelines. Technical Report 16, Swiss Department of the Interior, Bureau of Water Affairs.

Sturm, T. W. (2001). *Open Channel Hydraulics*. McGraw Hill.

Uzuner, M. S. and Kennedy, J. F. (1976). Theoretical model of river ice jams. *ASCE Journal of the Hydraulics Divison*, 102(9):1365–1383.

Watts, A. C., Ambrosia, V. G., and Hinkley, E. A. (2012). Unmanned aircraft systems in remote sensing and scientific research: Classification and considerations of use. *Remote Sensing*, 4:1671–1692.

Wazney, L., Clark, S. P., and Malenchak, J. (2019a). Effects of freeze-up consolidation event surges on river hydraulics and ice dynamics on the lower dauphin river. *Cold Regions Science and Technology*, 158:264–274.

Wazney, L., Clark, S. P., Malenchak, J., Knack, I., and Shen, H. T. (2019b). Numerical simulation of river ice cover formation and consolidation at freeze-up. *Cold Regions Science and Technology*, 168.

Wazney, L., Clark, S. P., and Wall, A. J. (2018). Field monitoring of secondary consolidation events and ice cover progression during freeze-up on the lower dauphin river, manitoba. *Cold Regions Science and Technology*, 148:159–171.

Westoby, M. J., Brasington, J., Glasser, N. F., Hambrey, M. J., and Reynolds, J. M. (2012). 'structure-from-motion' photogrammtery: A low-cost, effective tool for geoscience applications. *Geomorphology*, 179:300–314.

Wolman, M. G. (1954). A method of sampling coarse river-bed material. *Transactions, American Geophysical Union*, 35(6):951–956.

Appendix A Plots of Relevant Hydraulic Data

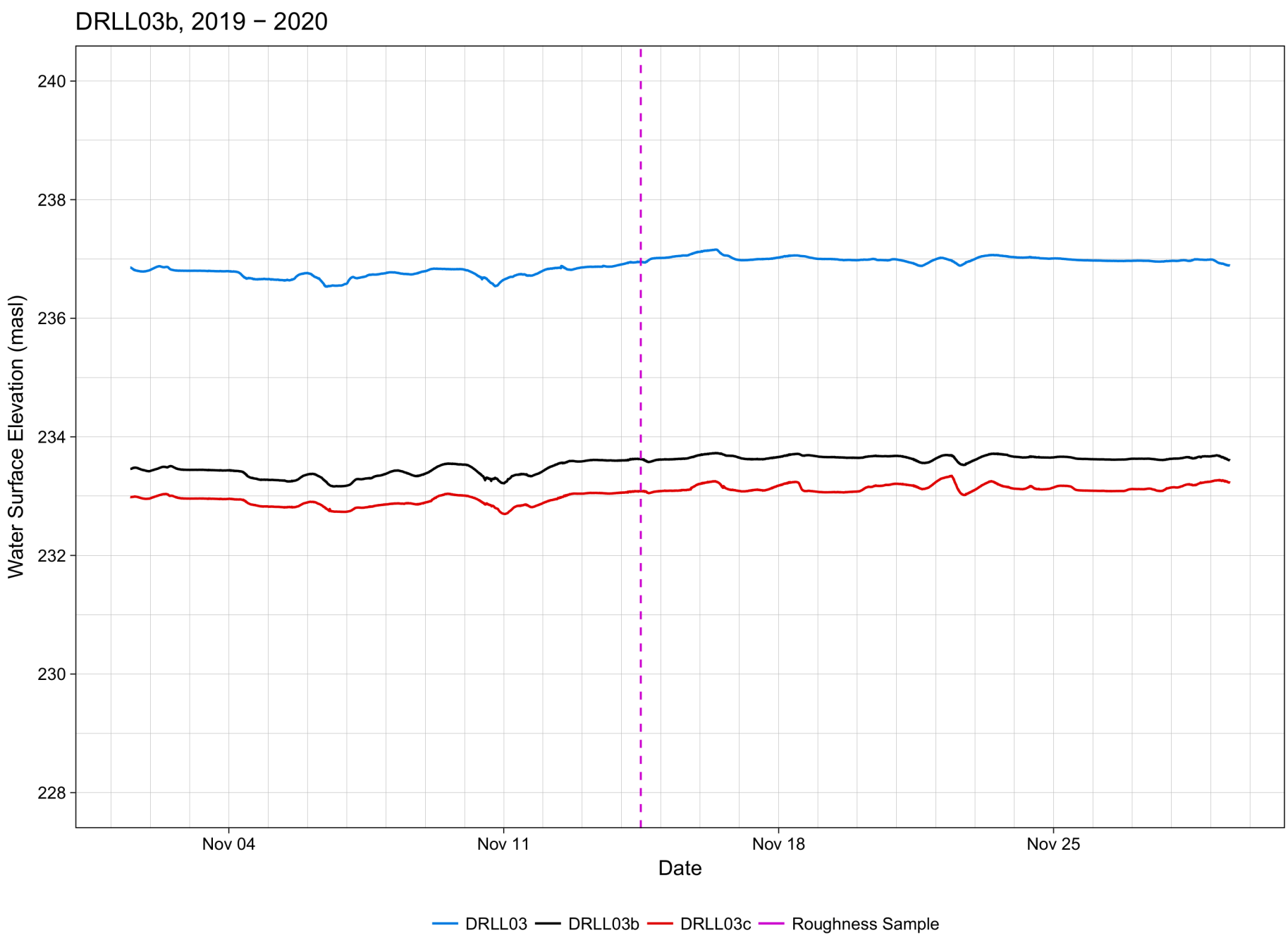
DRLL03b, 2019 − 2020
Water Surface Elevation (masl)
240
238
236
234
232
230
228
Nov 04
Nov 11
Nov 18
Nov 25
Date
DRLL03
DRLL03b
DRLL03c
Roughness Sample

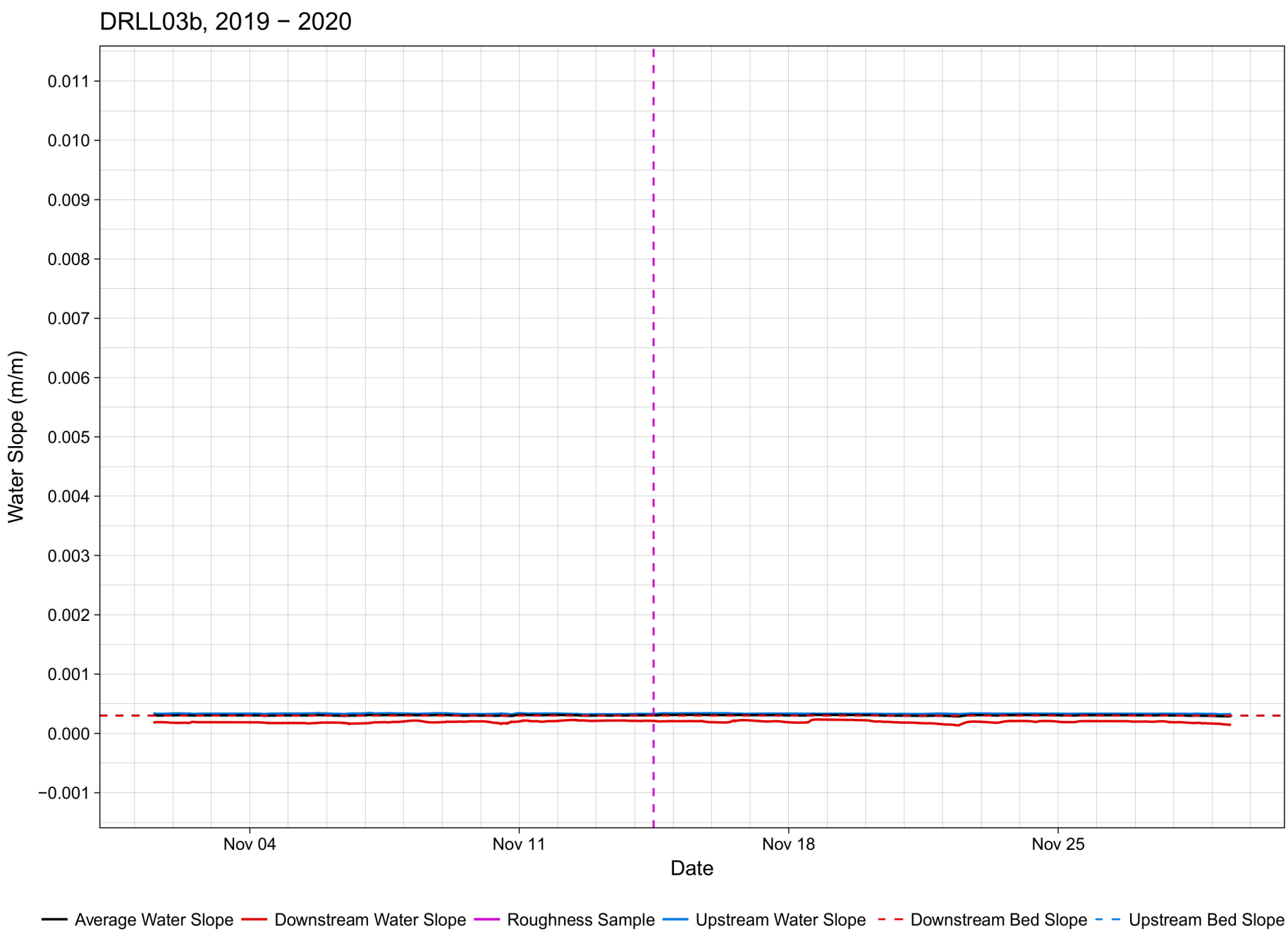
DRLL03b, 2019 − 2020
Water Slope (m/m)
0.011
0.010
0.009
0.008
0.007
0.006
0.005
0.004
0.003
0.002
0.001
0.000
−0.001
Nov 04
Nov 11
Nov 18
Nov 25
Date
Average Water Slope
Downstream Water Slope
Roughness Sample
Upstream Water Slope
Downstream Bed Slope
Upstream Bed Slope

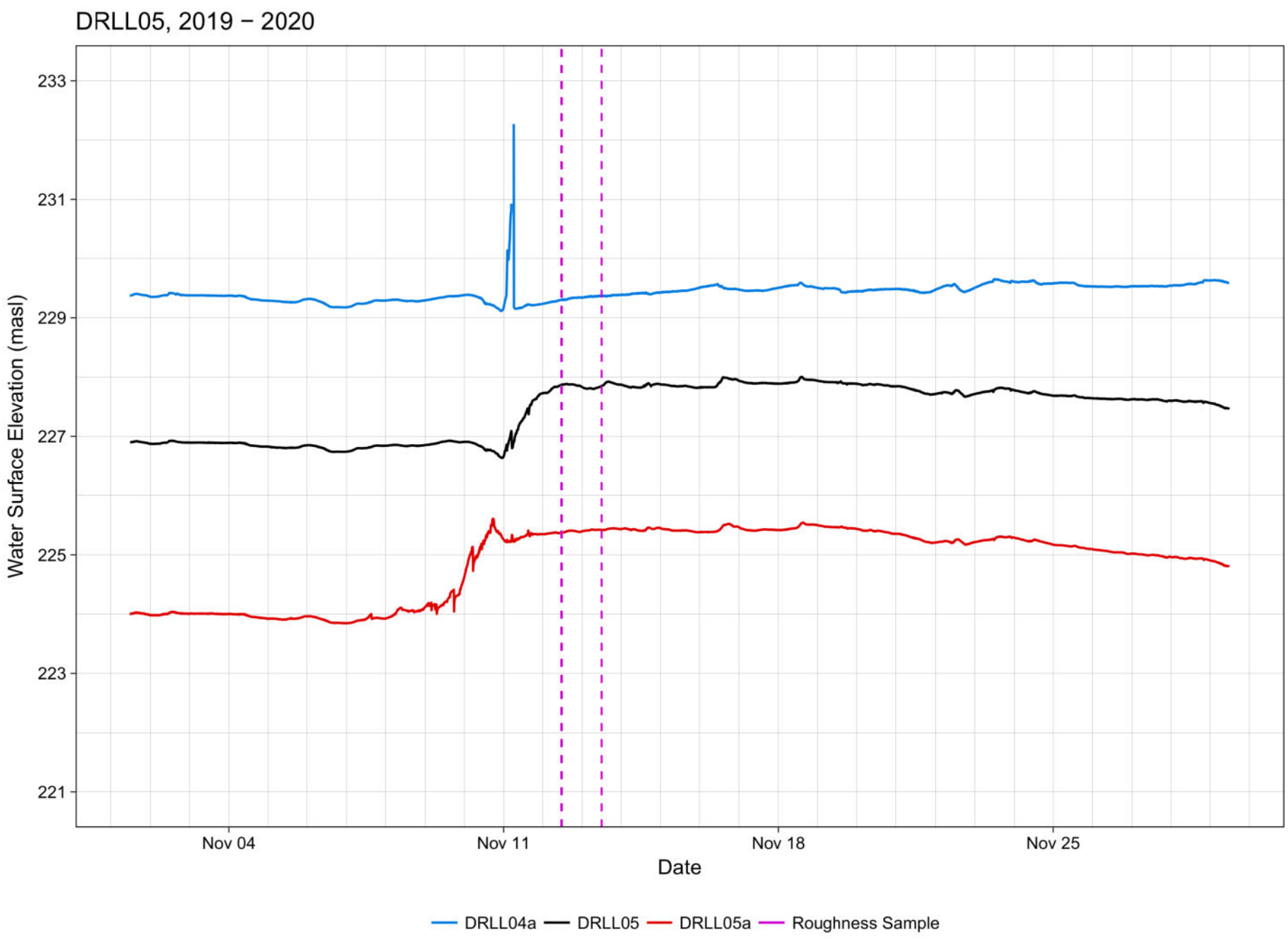
DRLL05, 2019 − 2020
Water Surface Elevation (masl)
233
231
229
227
225
223
221
Nov 04
Nov 11
Nov 18
Nov 25
Date
DRLL04a
DRLL05
DRLL05a
Roughness Sample

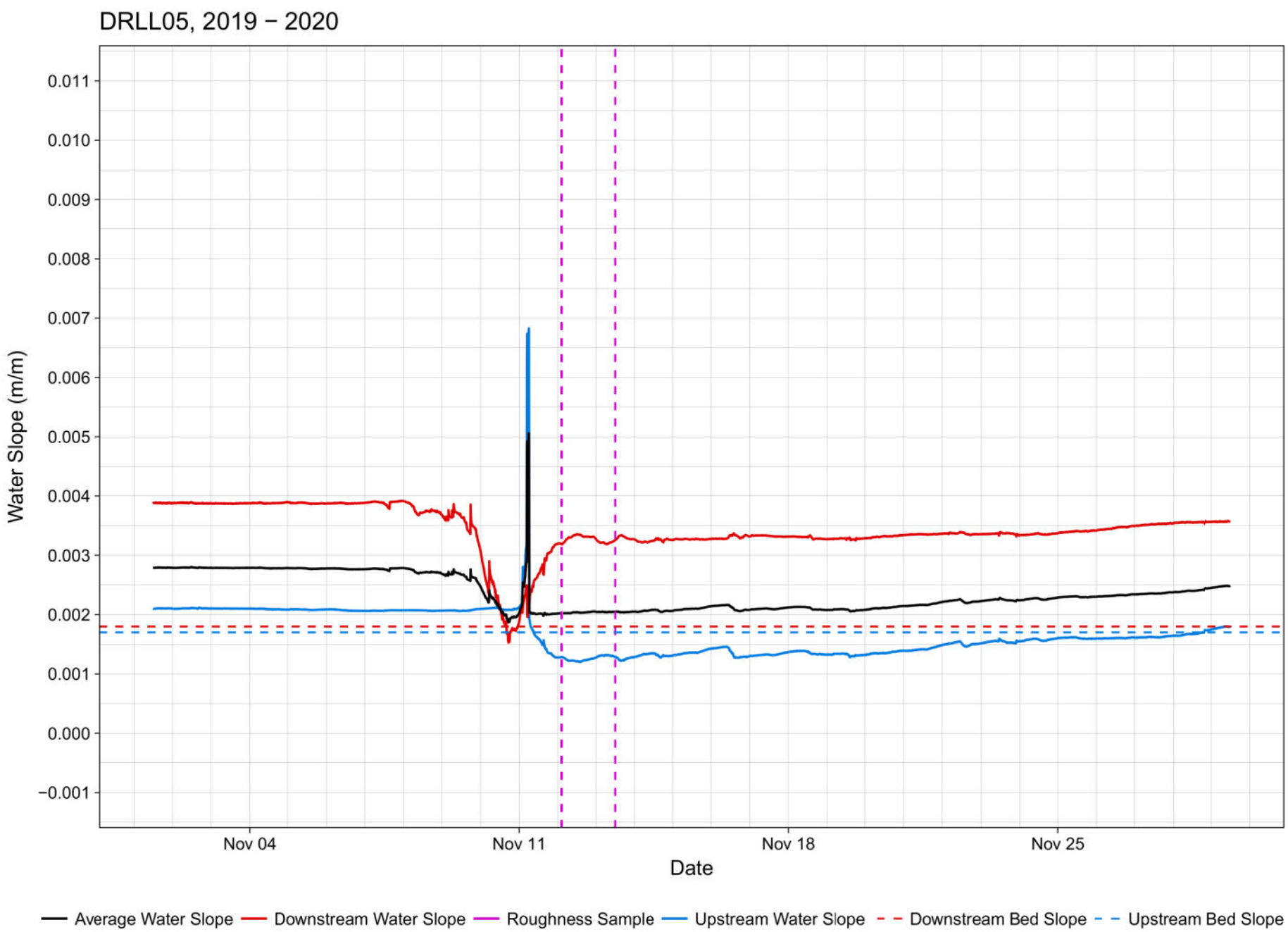
DRLL05, 2019 − 2020
Water Slope (m/m)
0.011
0.010
0.009
0.008
0.007
0.006
0.005
0.004
0.003
0.002
0.001
0.000
−0.001
Nov 04
Nov 11
Nov 18
Nov 25
Date
Average Water Slope
Downstream Water Slope
Roughness Sample
Upstream Water Slope
Downstream Bed Slope
Upstream Bed Slope

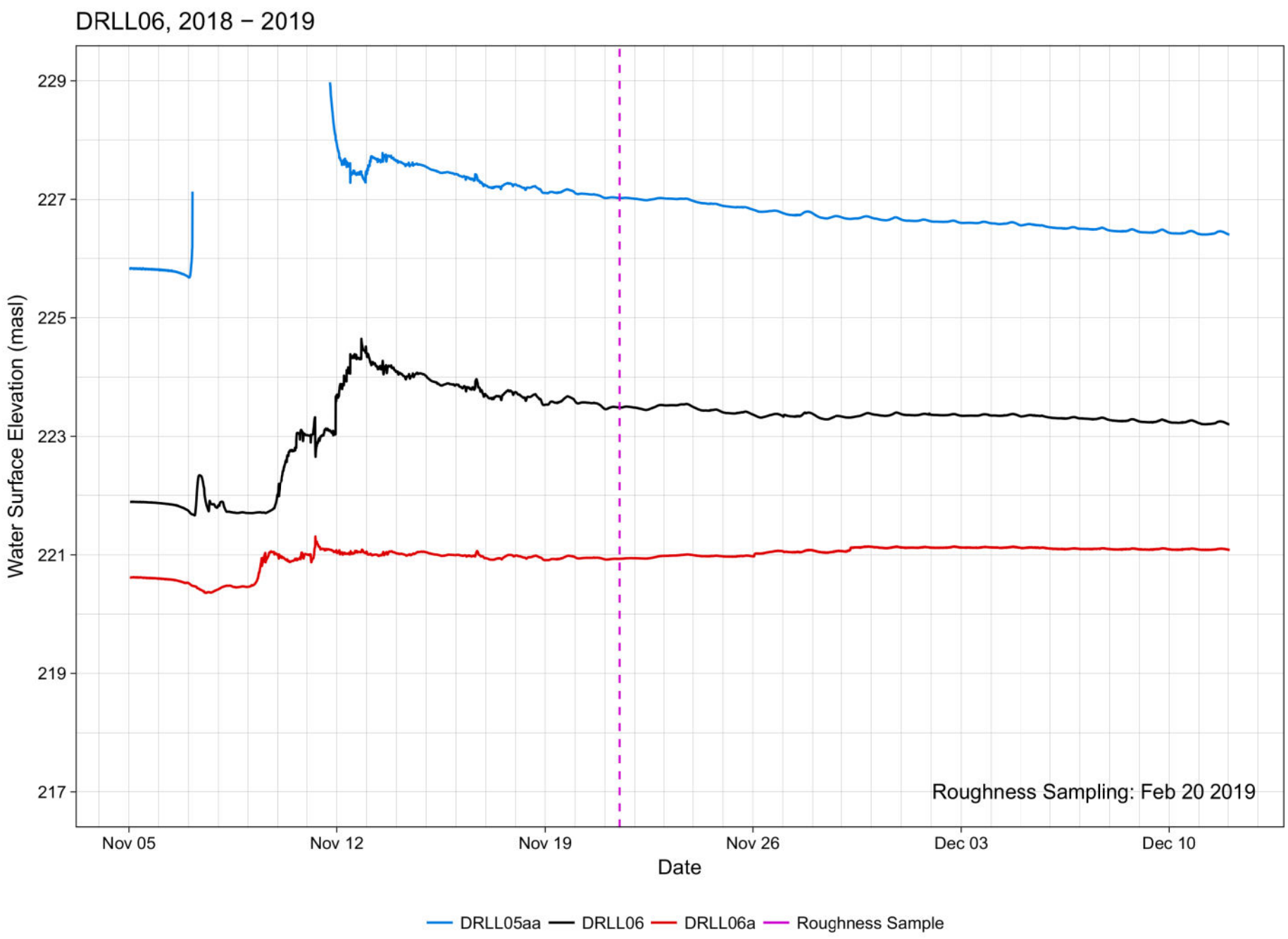
DRLL06, 2018 − 2019
Water Surface Elevation (masl)
229
227
225
223
221
219
217
Nov 05
Nov 12
Nov 19
Nov 26
Dec 03
Dec 10
Date
Roughness Sampling: Feb 20 2019
DRLL05aa
DRLL06
DRLL06a
Roughness Sample

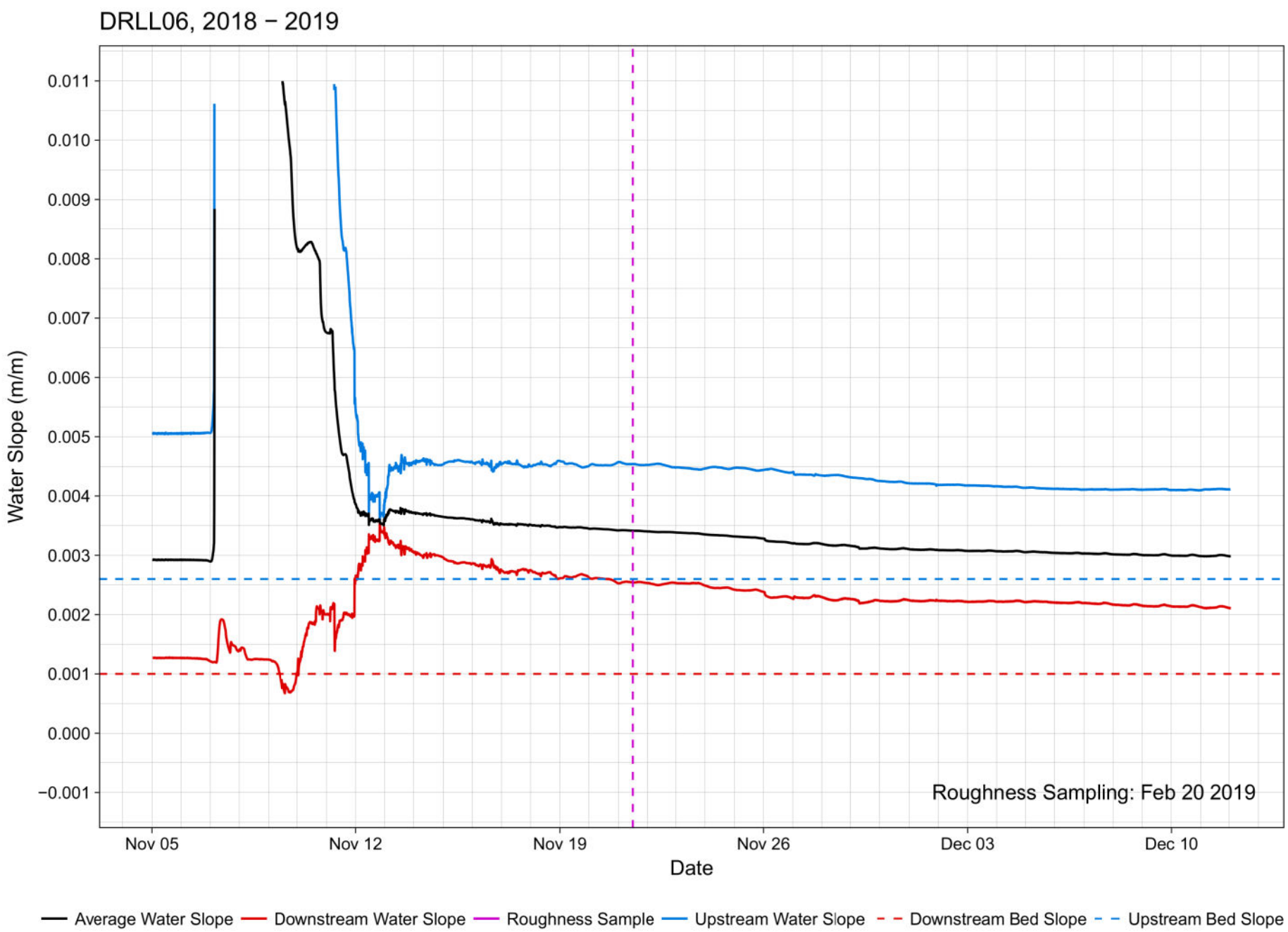
DRLL06, 2018 − 2019
Water Slope (m/m)
0.011
0.010
0.009
0.008
0.007
0.006
0.005
0.004
0.003
0.002
0.001
0.000
−0.001
Nov 05
Nov 12
Nov 19
Nov 26
Dec 03
Dec 10
Date
Roughness Sampling: Feb 20 2019
Average Water Slope
Downstream Water Slope
Roughness Sample
Upstream Water Slope
Downstream Bed Slope
Upstream Bed Slope

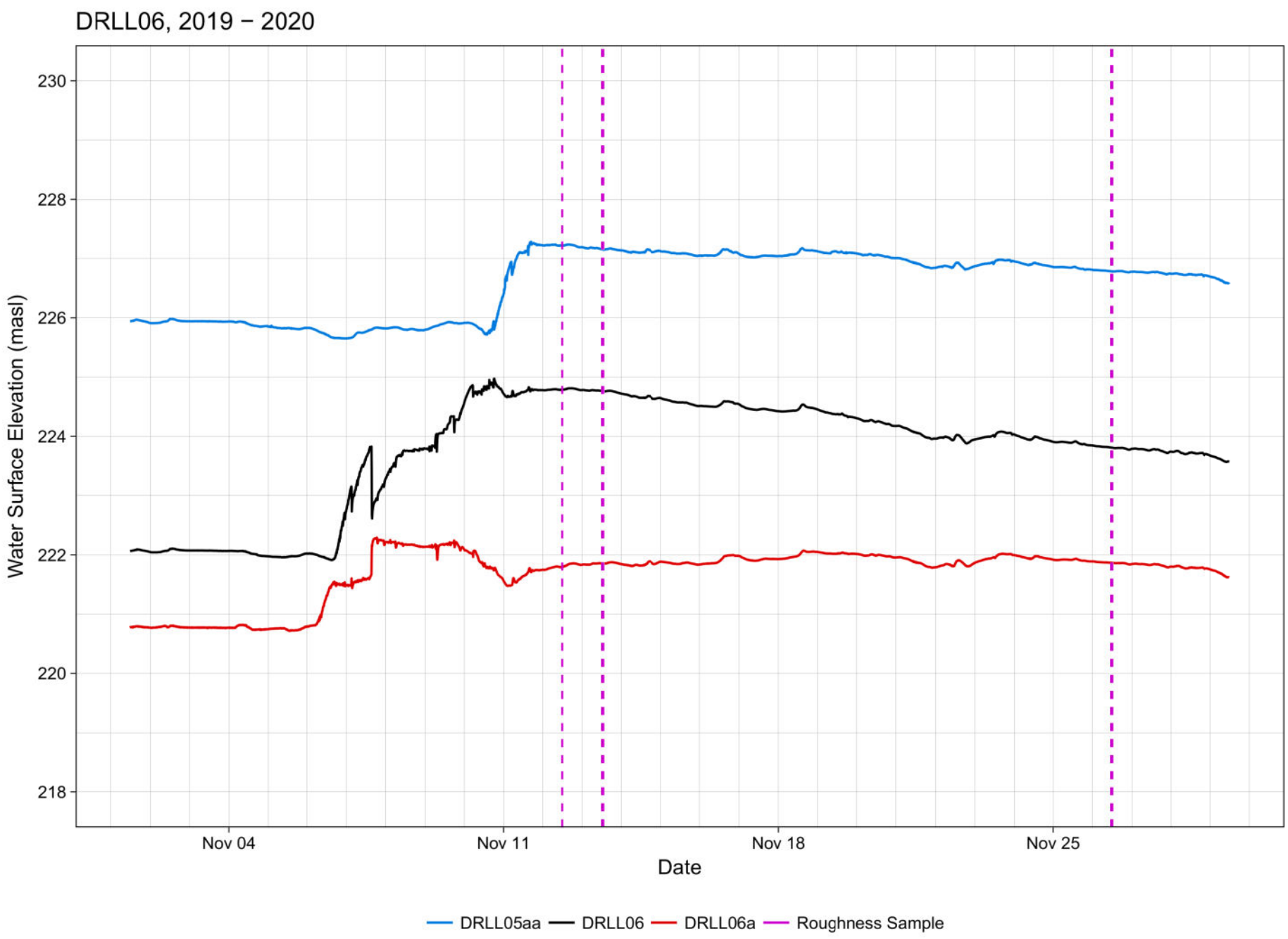
DRLL06, 2019 − 2020
Water Surface Elevation (masl)
230
228
226
224
222
220
218
Nov 04
Nov 11
Nov 18
Nov 25
Date
DRLL05aa
DRLL06
DRLL06a
Roughness Sample

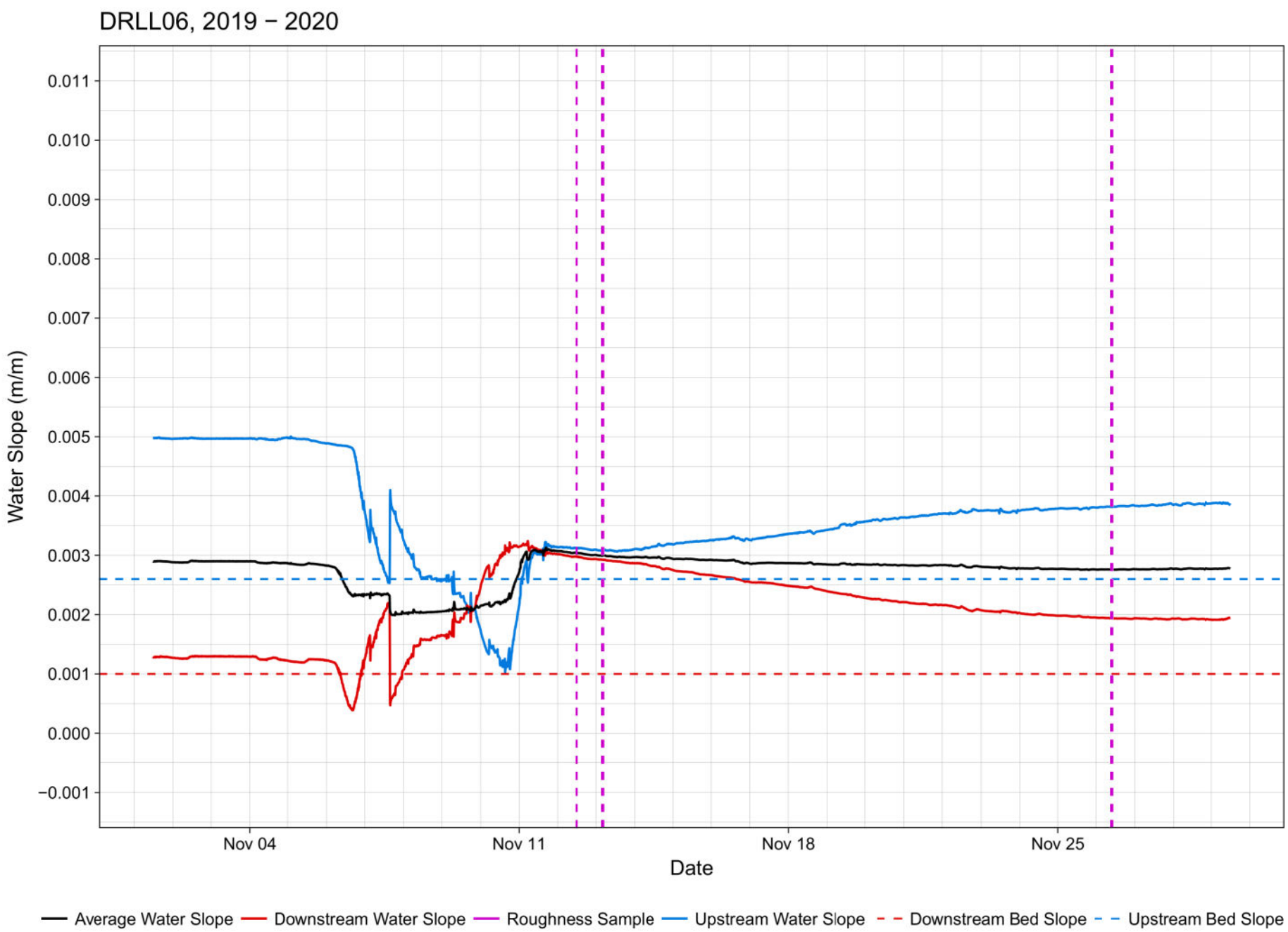
DRLL06, 2019 − 2020
Water Slope (m/m)
0.011
0.010
0.009
0.008
0.007
0.006
0.005
0.004
0.003
0.002
0.001
0.000
−0.001
Nov 04
Nov 11
Nov 18
Nov 25
Date
Average Water Slope
Downstream Water Slope
Roughness Sample
Upstream Water Slope
Downstream Bed Slope
Upstream Bed Slope

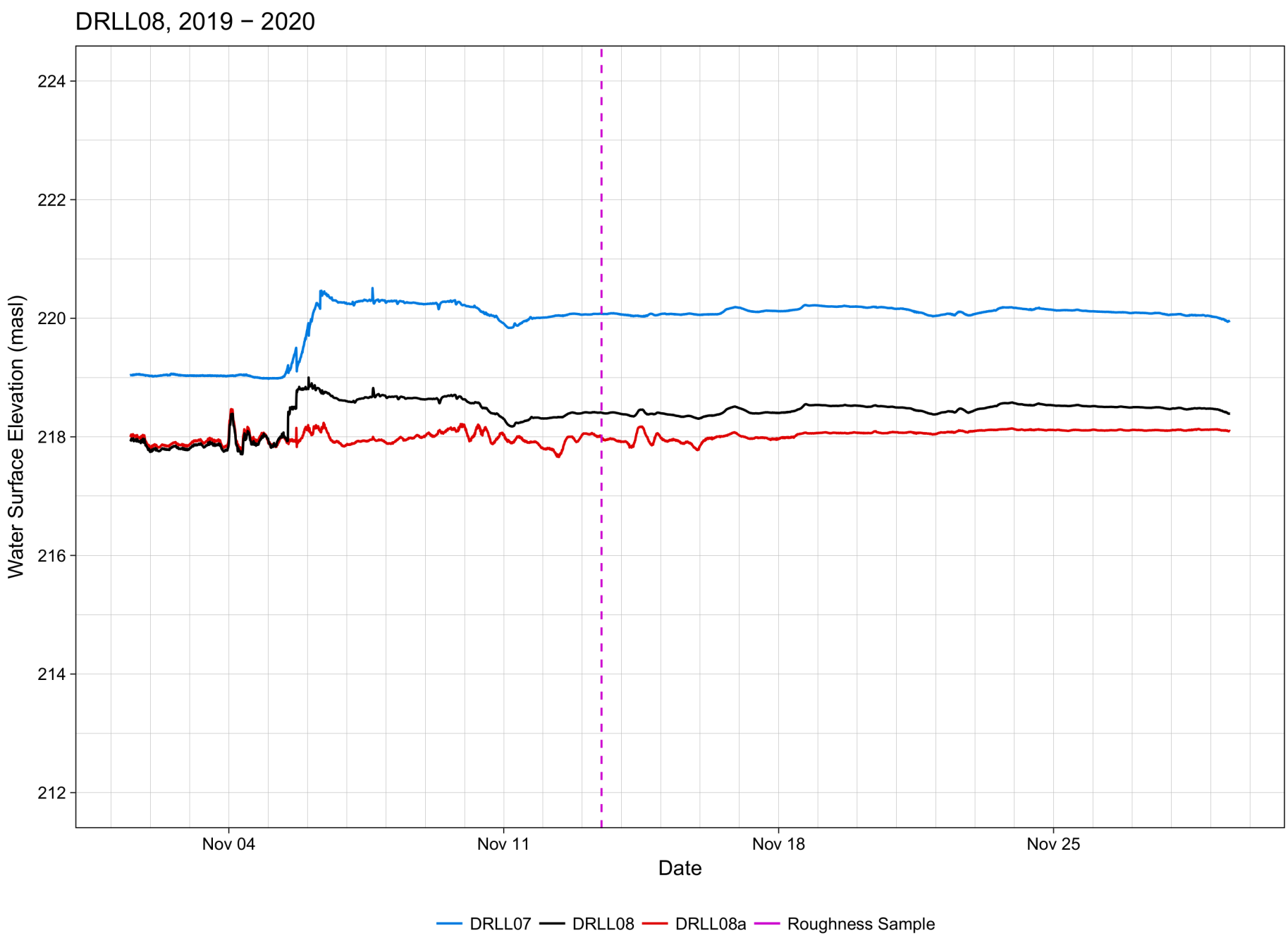
DRLL08, 2019 − 2020
Water Surface Elevation (masl)
224
222
220
218
216
214
212
Nov 04
Nov 11
Nov 18
Nov 25
Date
DRLL07
DRLL08
DRLL08a
Roughness Sample

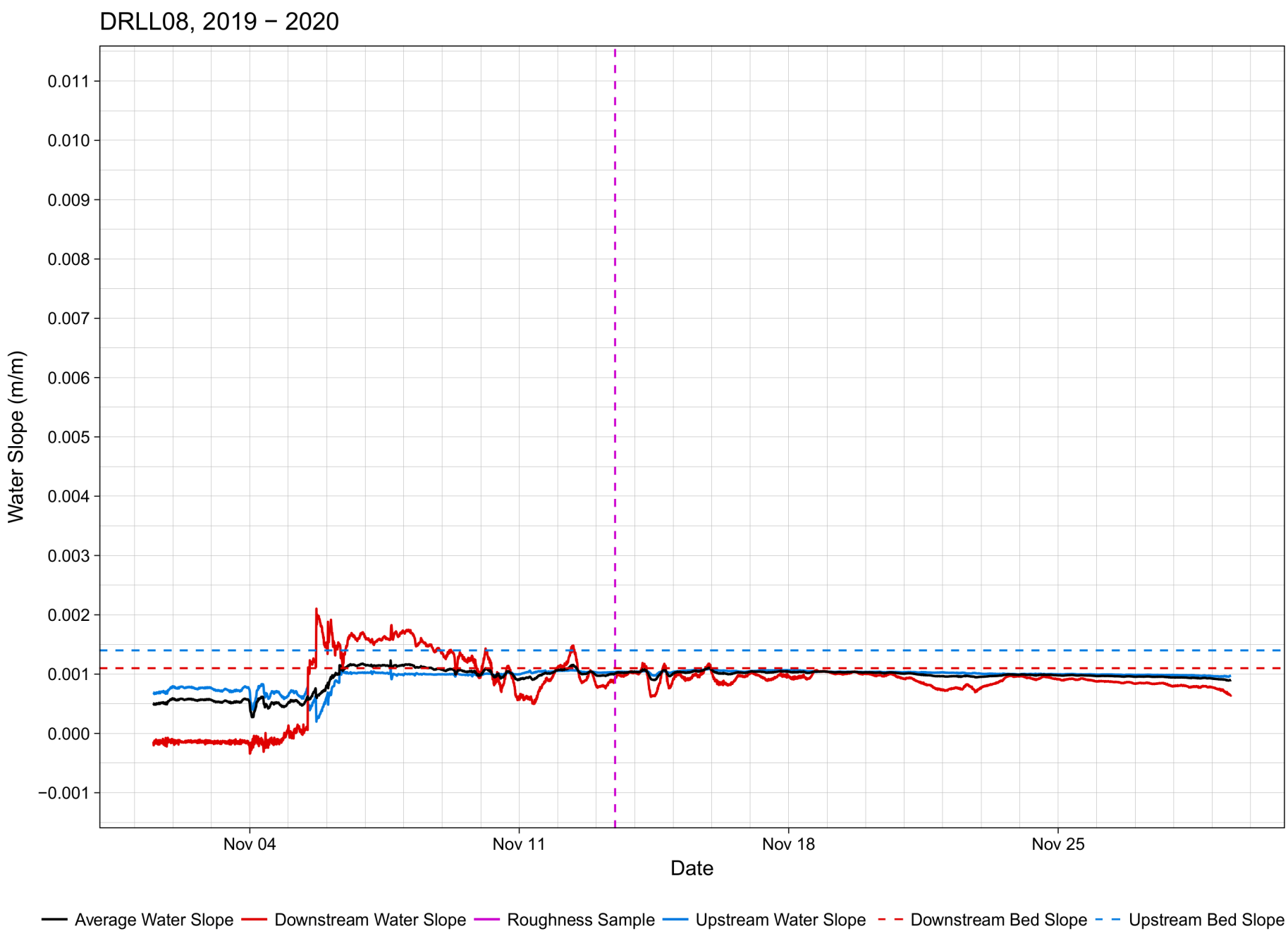
DRLL08, 2019 − 2020
Water Slope (m/m)
0.011
0.010
0.009
0.008
0.007
0.006
0.005
0.004
0.003
0.002
0.001
0.000
−0.001
Nov 04
Nov 11
Nov 18
Nov 25
Date
Average Water Slope
Downstream Water Slope
Roughness Sample
Upstream Water Slope
Downstream Bed Slope
Upstream Bed Slope

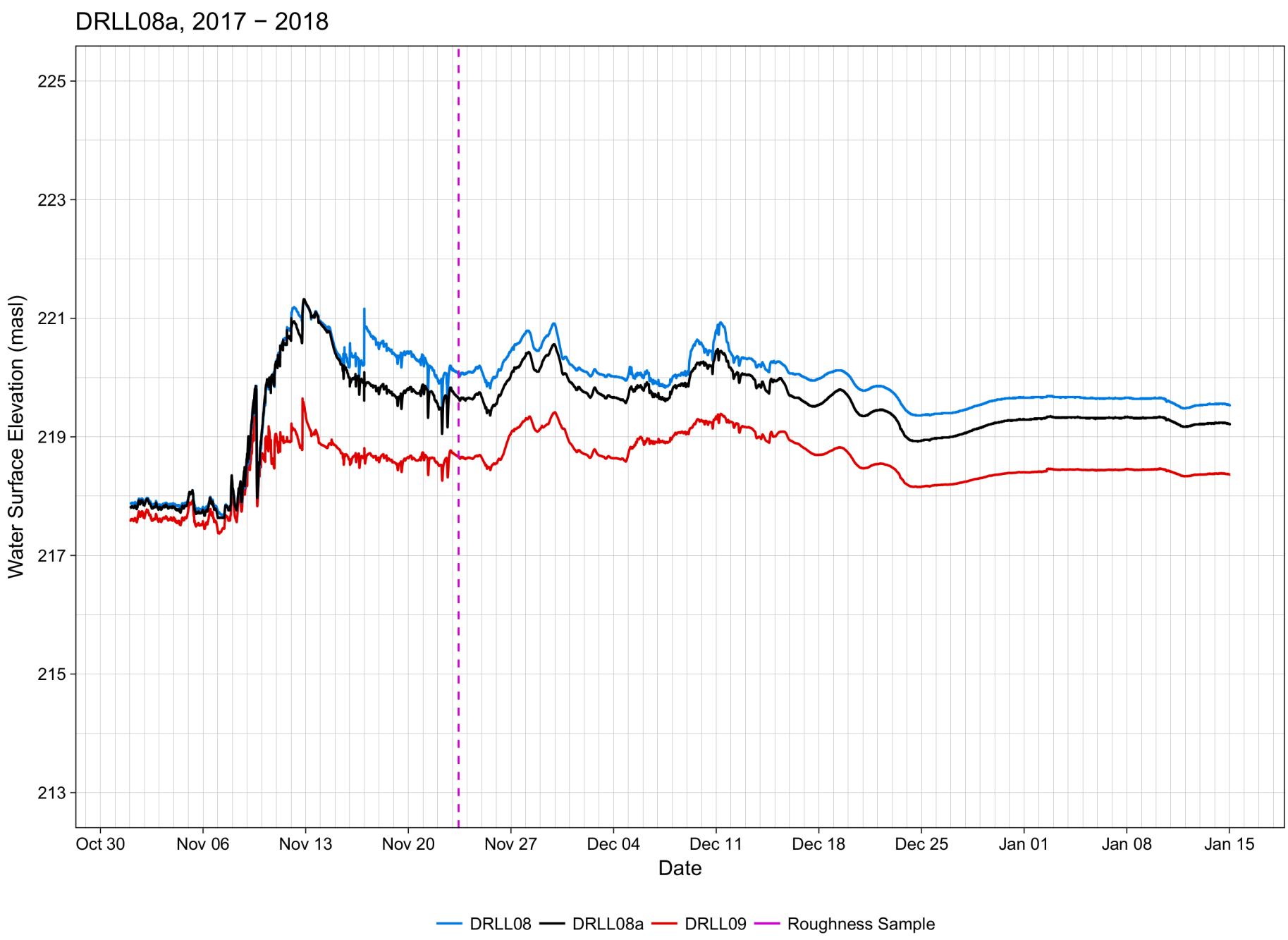
DRLL08a, 2017 − 2018
Water Surface Elevation (masl)
225
223
221
219
217
215
213
Oct 30
Nov 06
Nov 13
Nov 20
Nov 27
Dec 04
Dec 11
Dec 18
Dec 25
Jan 01
Jan 08
Jan 15
Date
DRLL08
DRLL08a
DRLL09
Roughness Sample

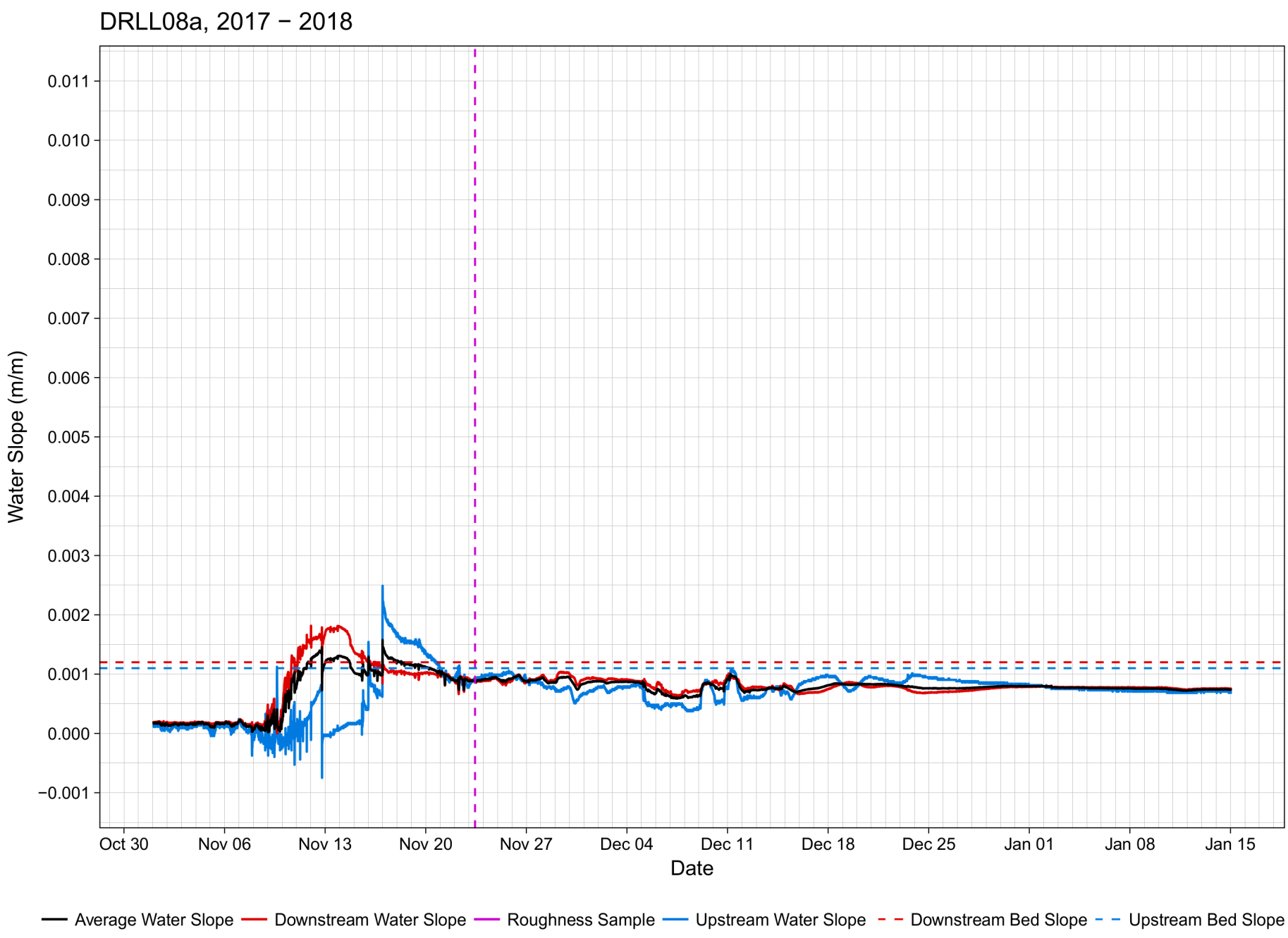
DRLL08a, 2017 − 2018
Water Slope (m/m)
0.011
0.010
0.009
0.008
0.007
0.006
0.005
0.004
0.003
0.002
0.001
0.000
−0.001
Oct 30
Nov 06
Nov 13
Nov 20
Nov 27
Dec 04
Dec 11
Dec 18
Dec 25
Jan 01
Jan 08
Jan 15
Date
Average Water Slope
Downstream Water Slope
Roughness Sample
Upstream Water Slope
Downstream Bed Slope
Upstream Bed Slope

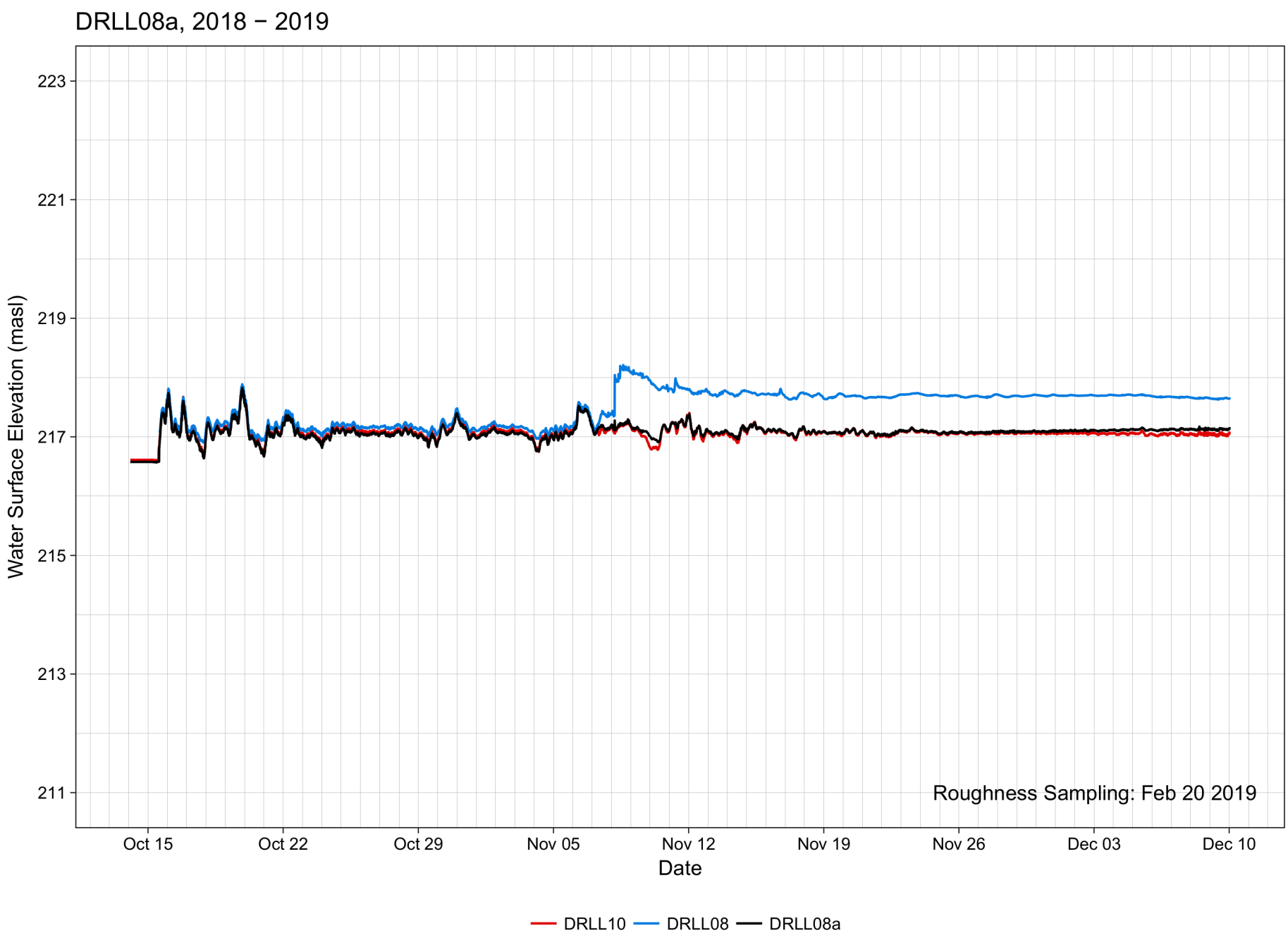
DRLL08a, 2018 − 2019
Water Surface Elevation (masl)
223
221
219
217
215
213
211
Roughness Sampling: Feb 20 2019
Oct 15
Oct 22
Oct 29
Nov 05
Nov 12
Nov 19
Nov 26
Dec 03
Dec 10
Date
DRLL10
DRLL08
DRLL08a

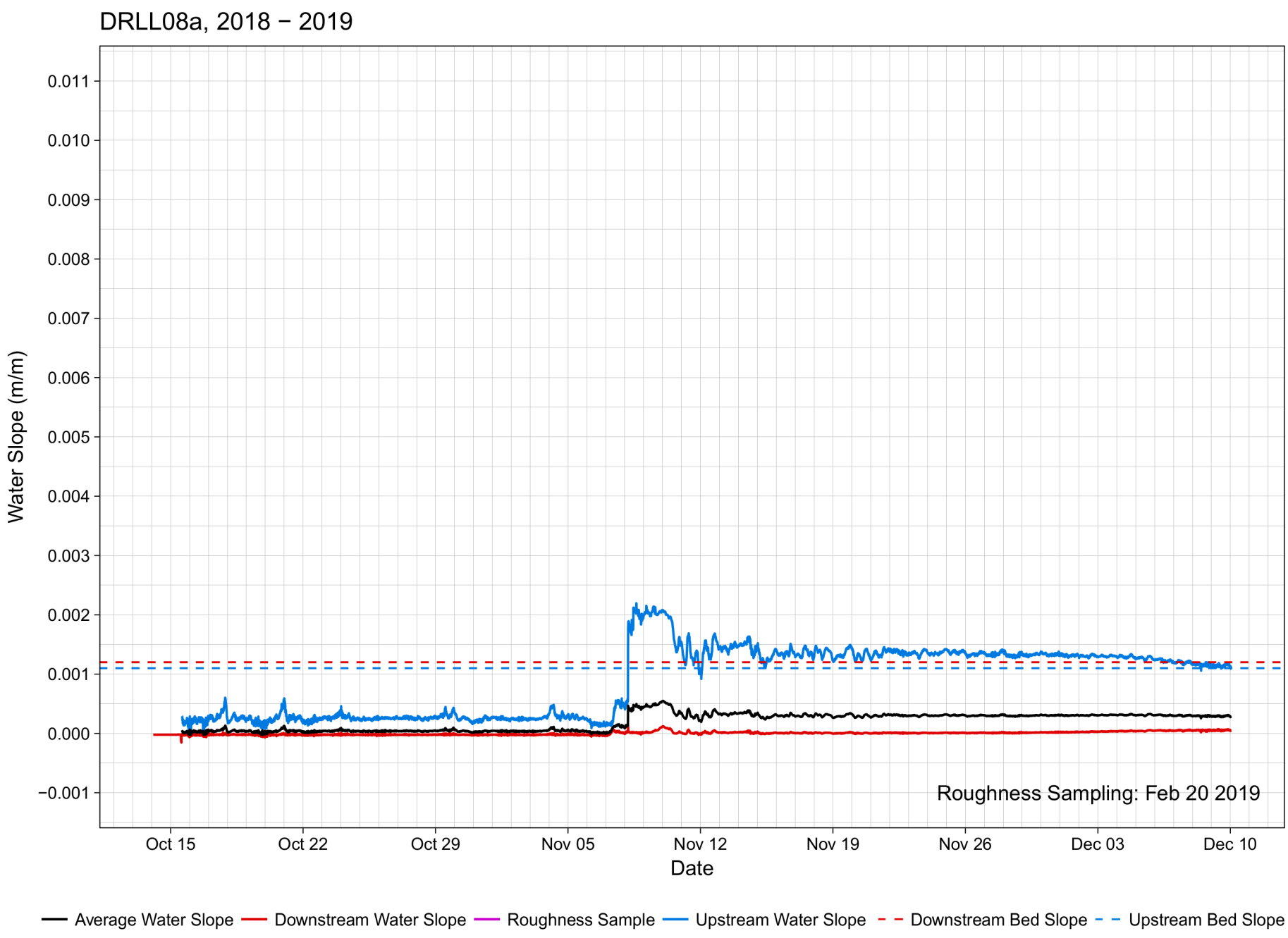
DRLL08a, 2018 − 2019
Water Slope (m/m)
0.011
0.010
0.009
0.008
0.007
0.006
0.005
0.004
0.003
0.002
0.001
0.000
−0.001
Roughness Sampling: Feb 20 2019
Oct 15
Oct 22
Oct 29
Nov 05
Nov 12
Nov 19
Nov 26
Dec 03
Dec 10
Date
Average Water Slope
Downstream Water Slope
Roughness Sample
Upstream Water Slope
Downstream Bed Slope
Upstream Bed Slope

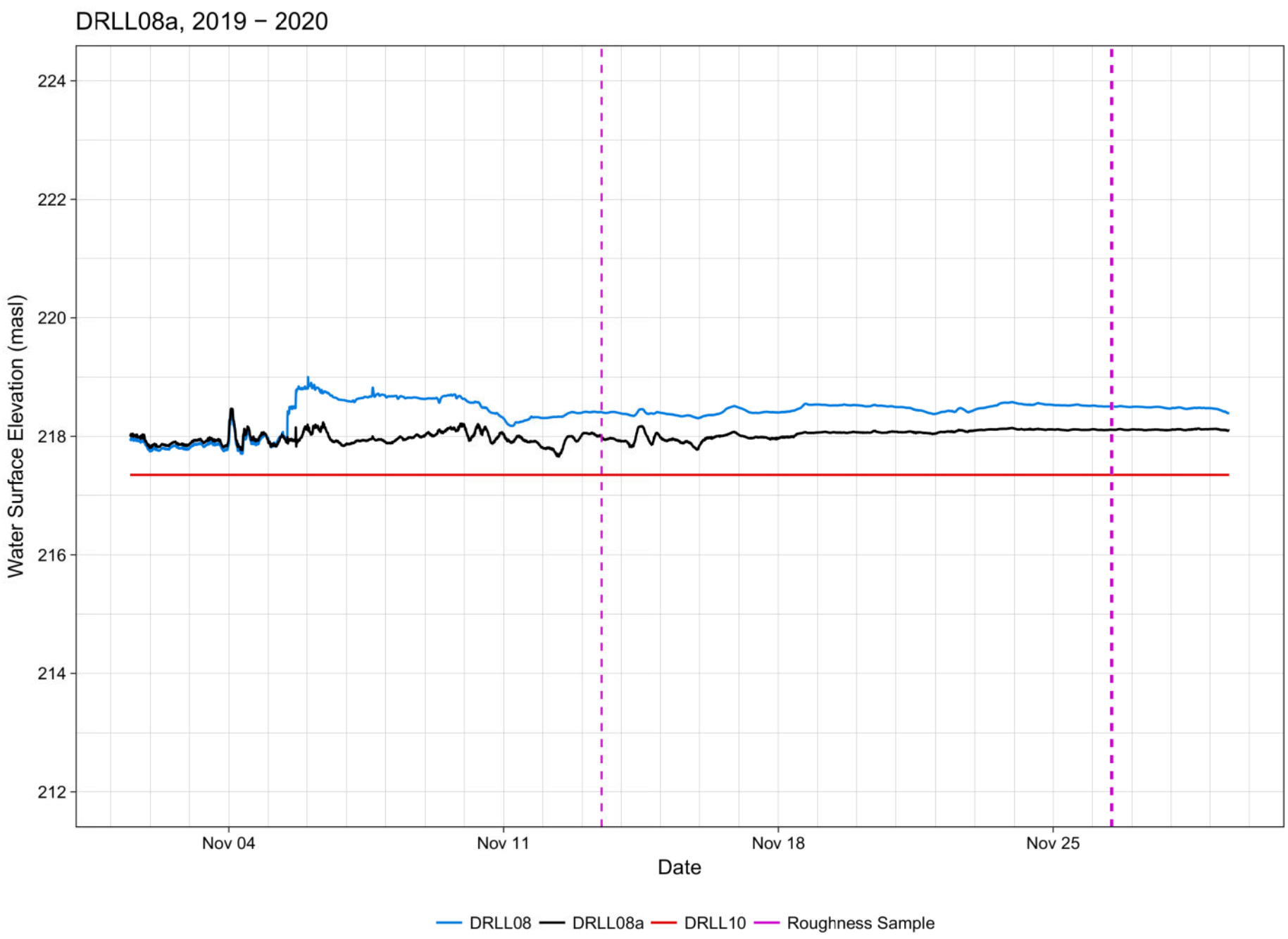
DRLL08a, 2019 − 2020
Water Surface Elevation (masl)
224
222
220
218
216
214
212
Nov 04
Nov 11
Nov 18
Nov 25
Date
DRLL08
DRLL08a
DRLL10
Roughness Sample

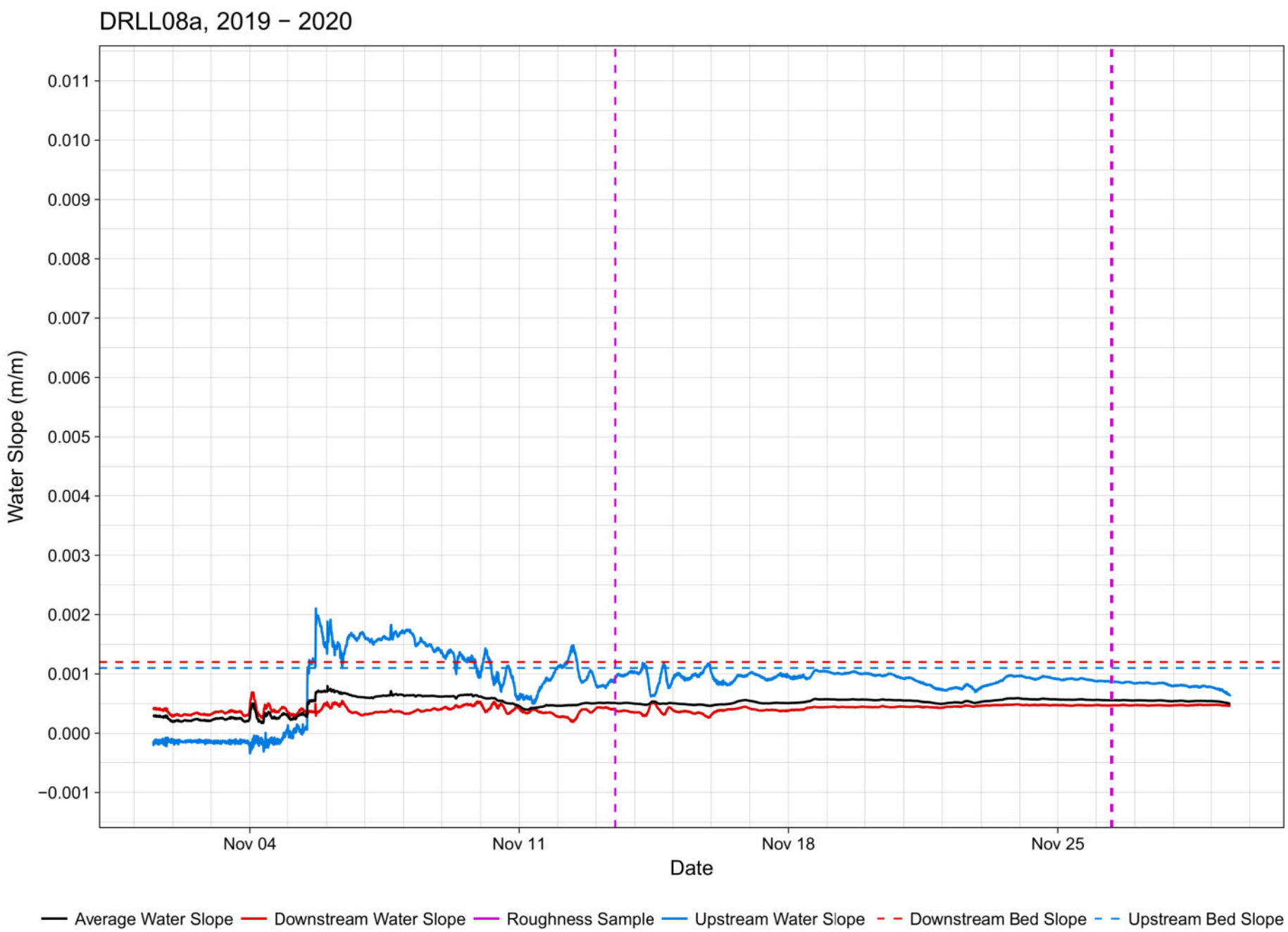
DRLL08a, 2019 − 2020
Water Slope (m/m)
0.011
0.010
0.009
0.008
0.007
0.006
0.005
0.004
0.003
0.002
0.001
0.000
−0.001
Nov 04
Nov 11
Nov 18
Nov 25
Date
Average Water Slope
Downstream Water Slope
Roughness Sample
Upstream Water Slope
Downstream Bed Slope
Upstream Bed Slope

Appendix B Histograms of Ice Roughness Heights Obtained Through RPA-Photogrammetry

DRLL03b 2019.11.14

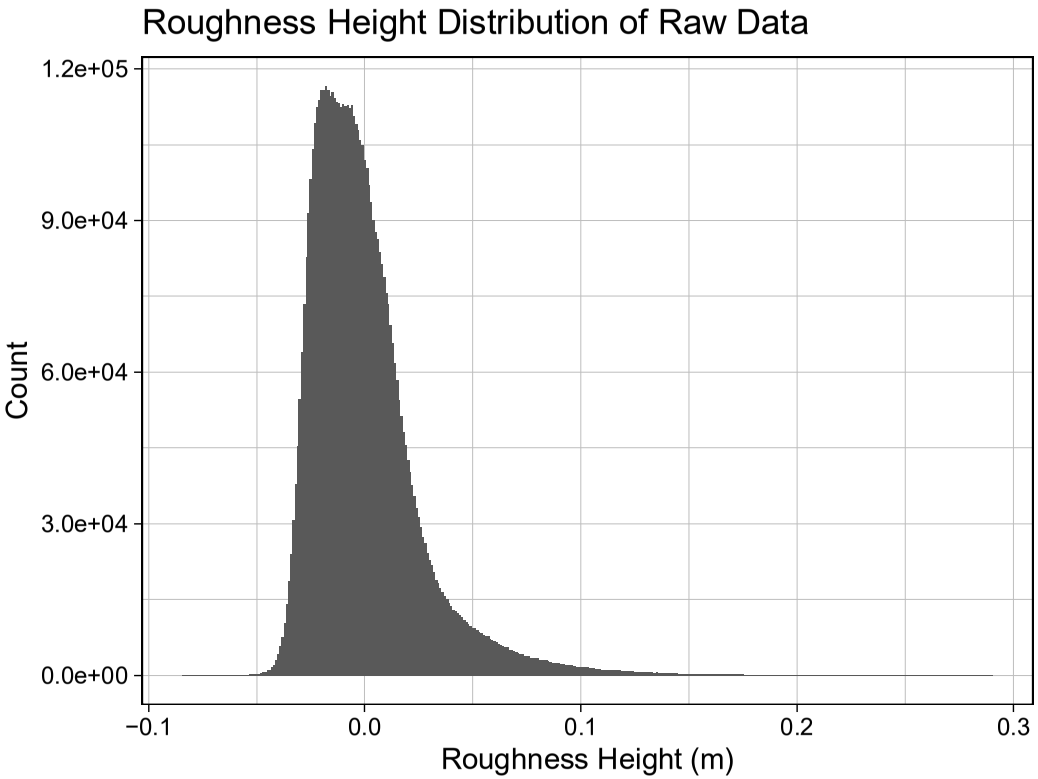

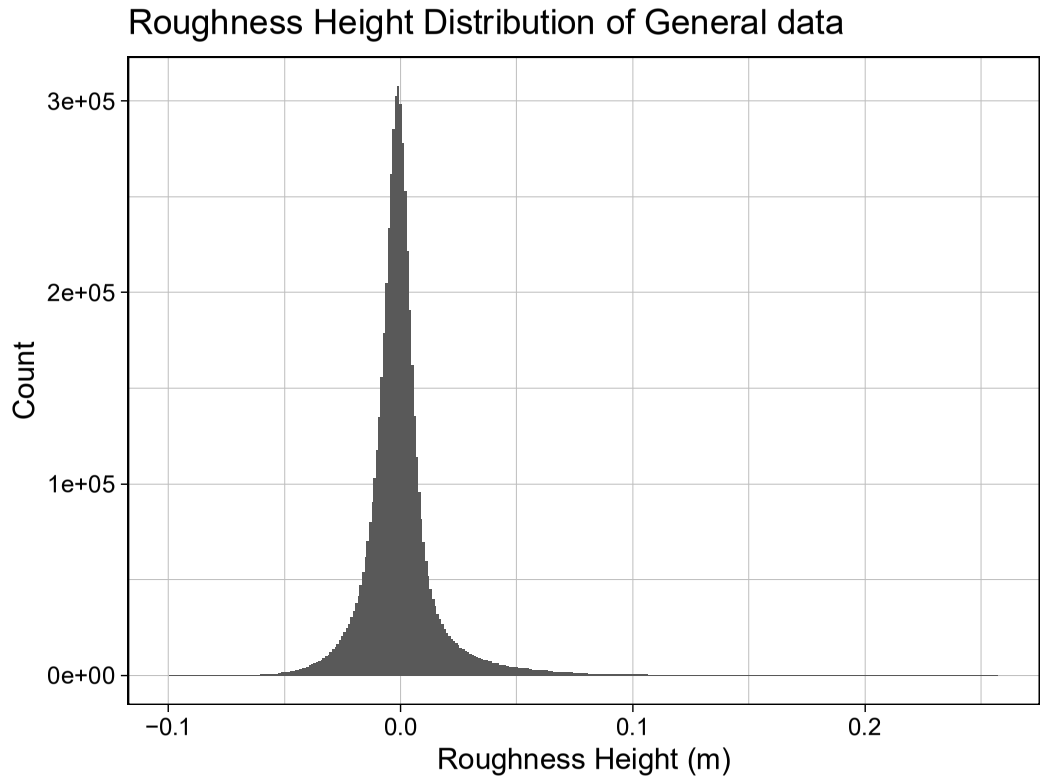

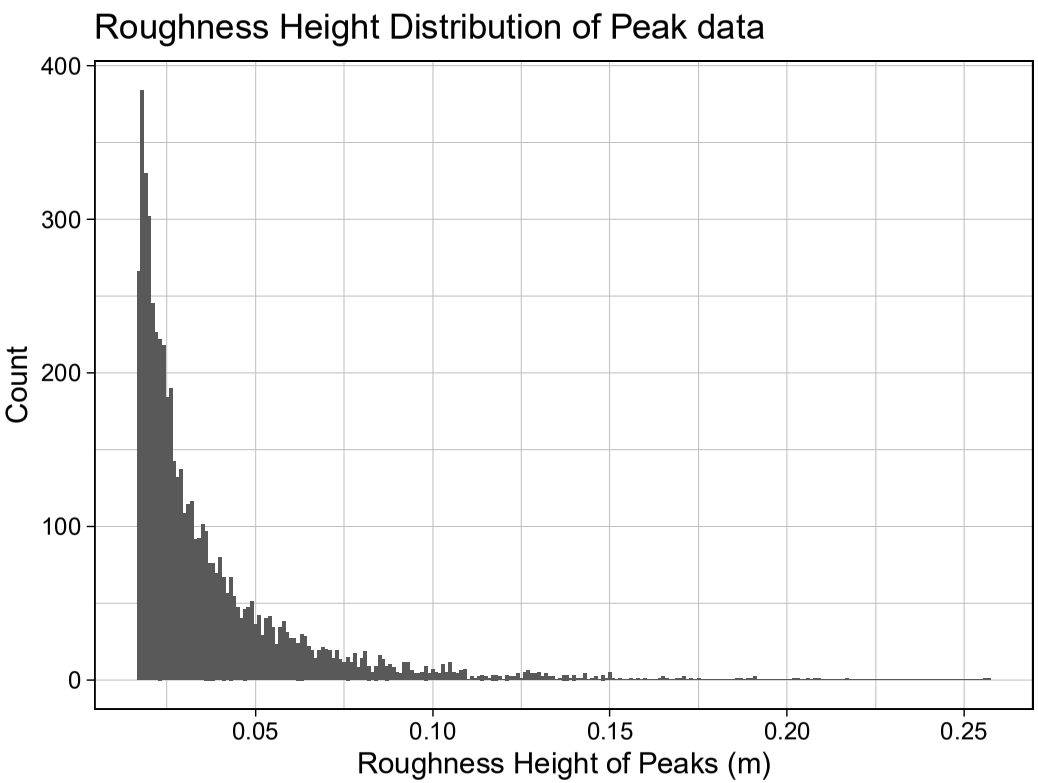

Representative RPA Photo of Surface Roughness

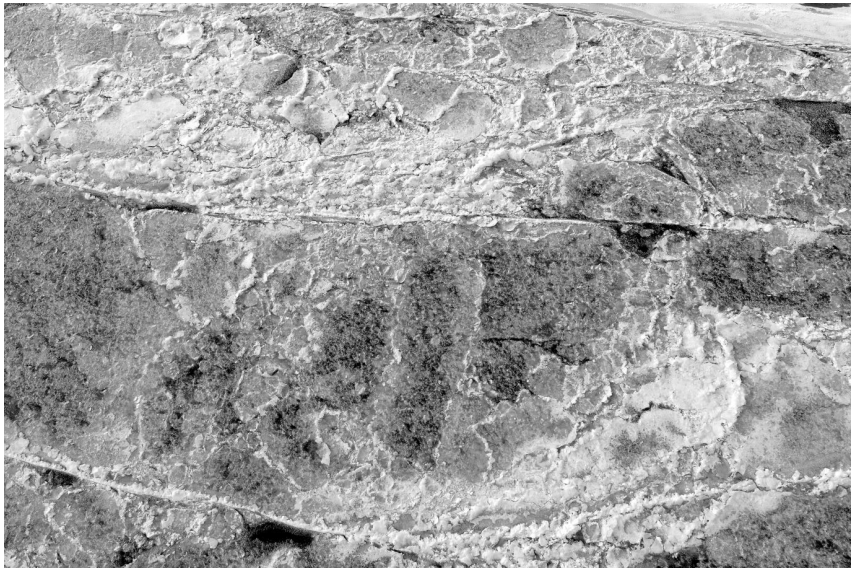

DRLL05 2019.11.12

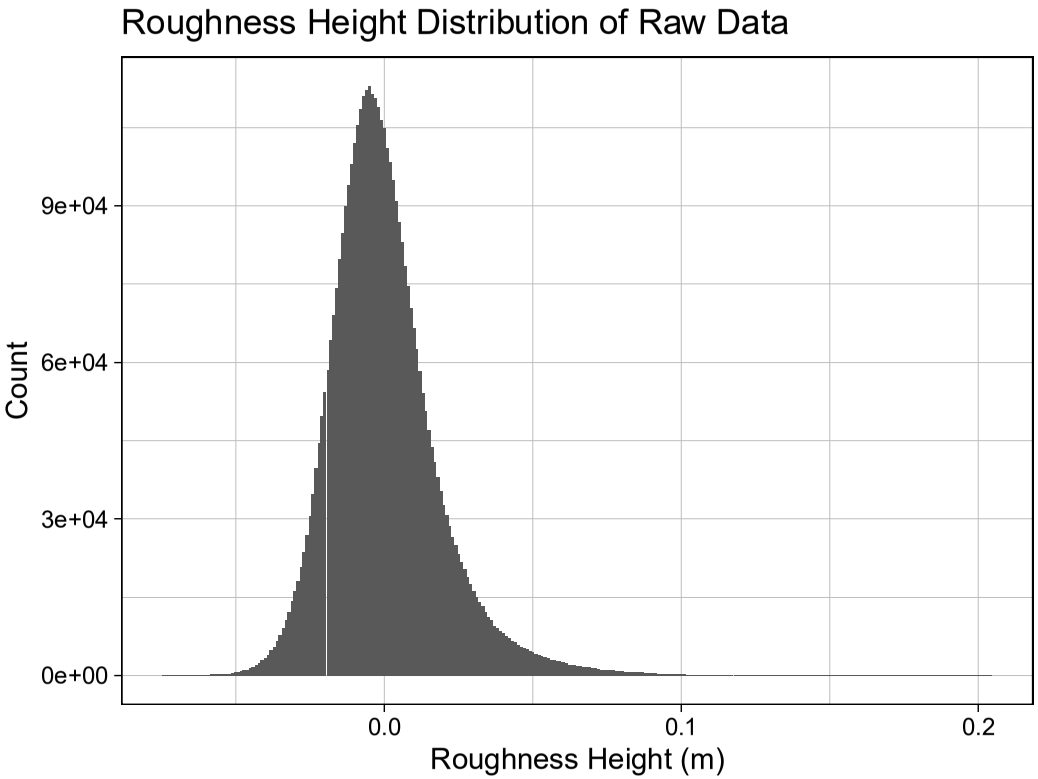

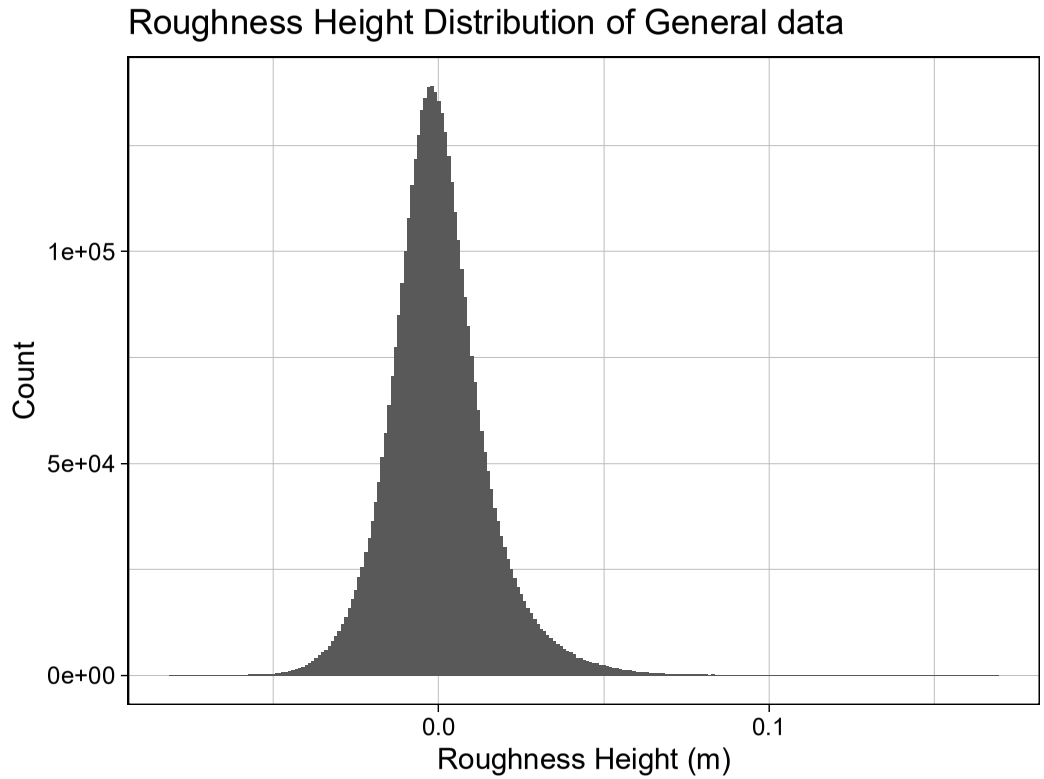

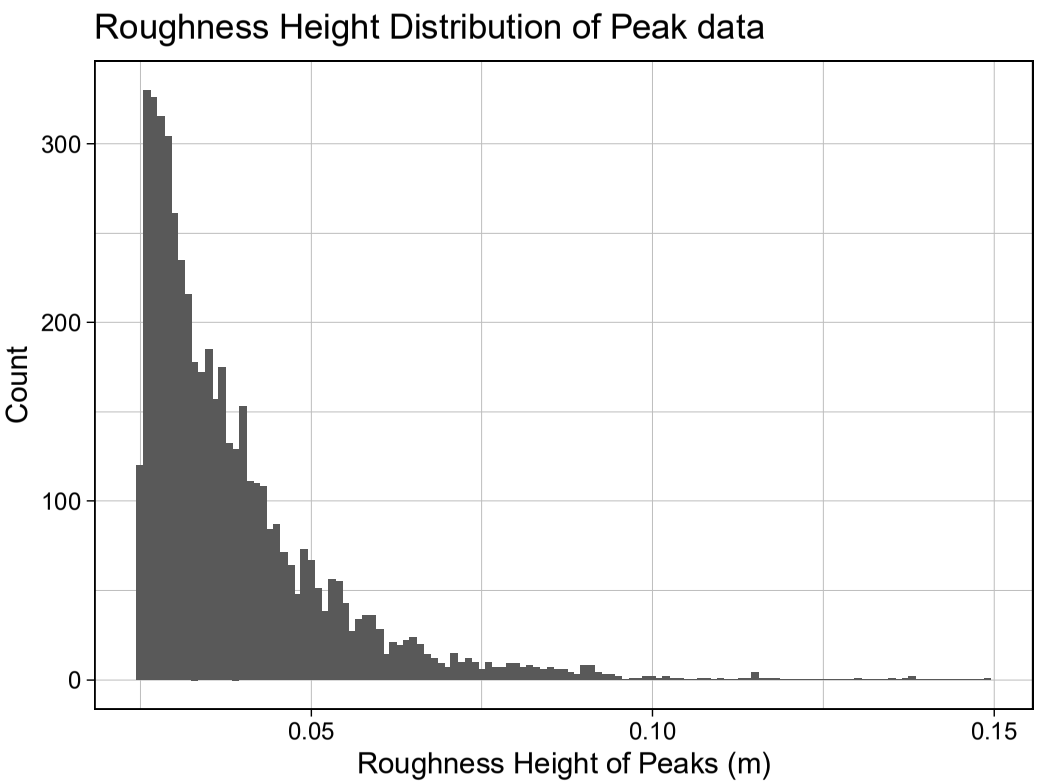

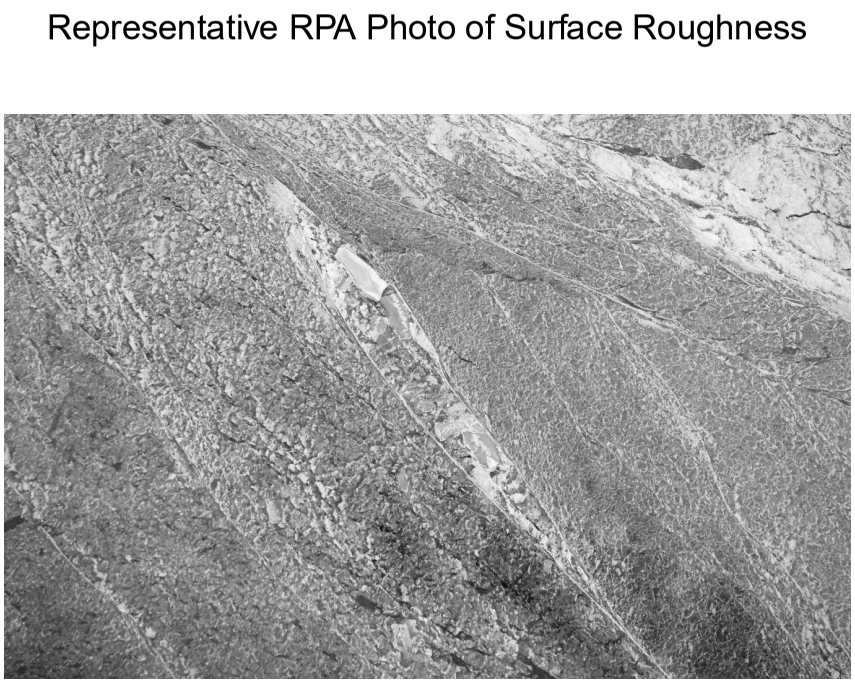

DRLL05 2019.11.13

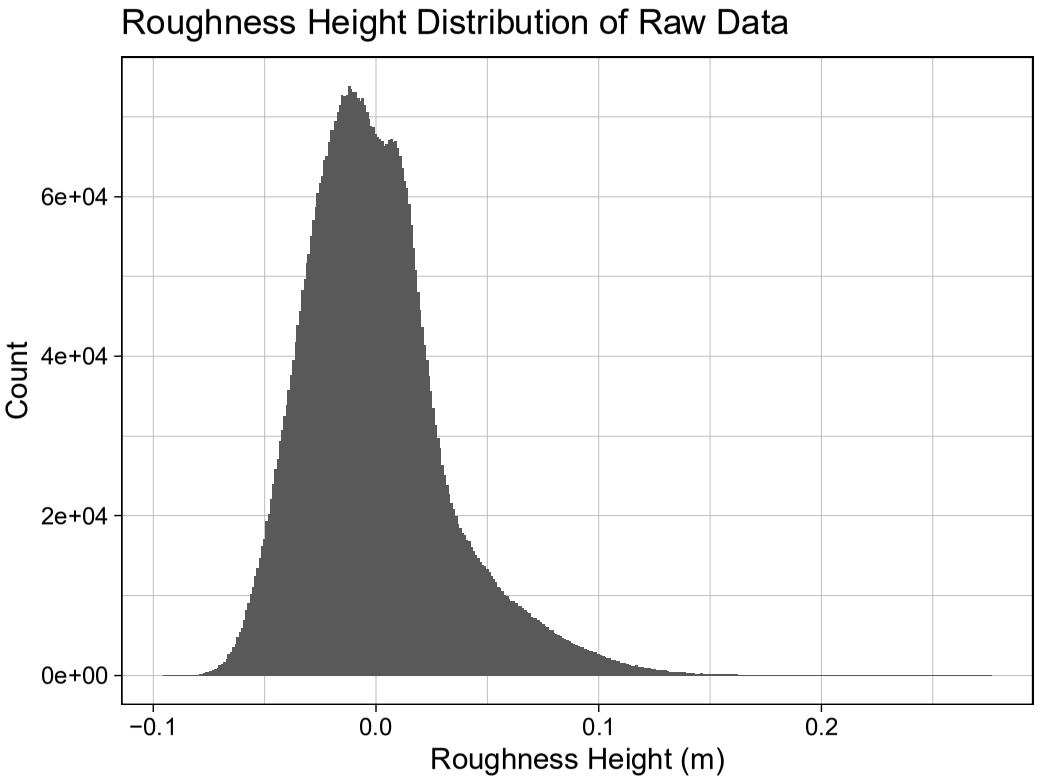

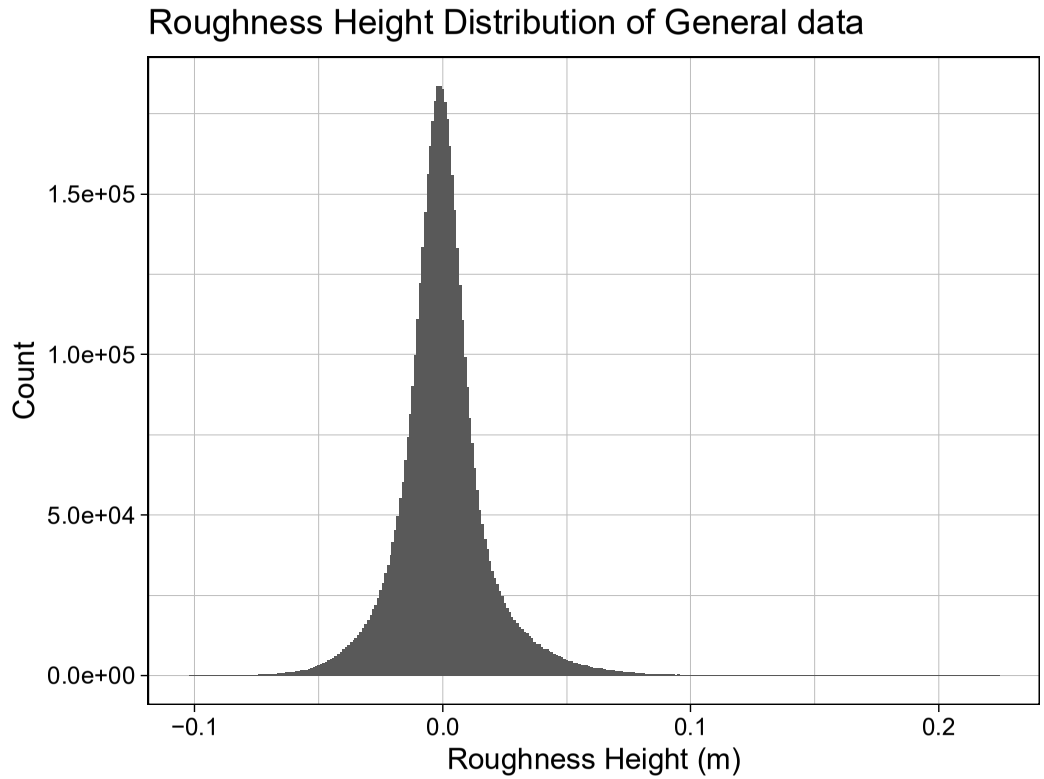

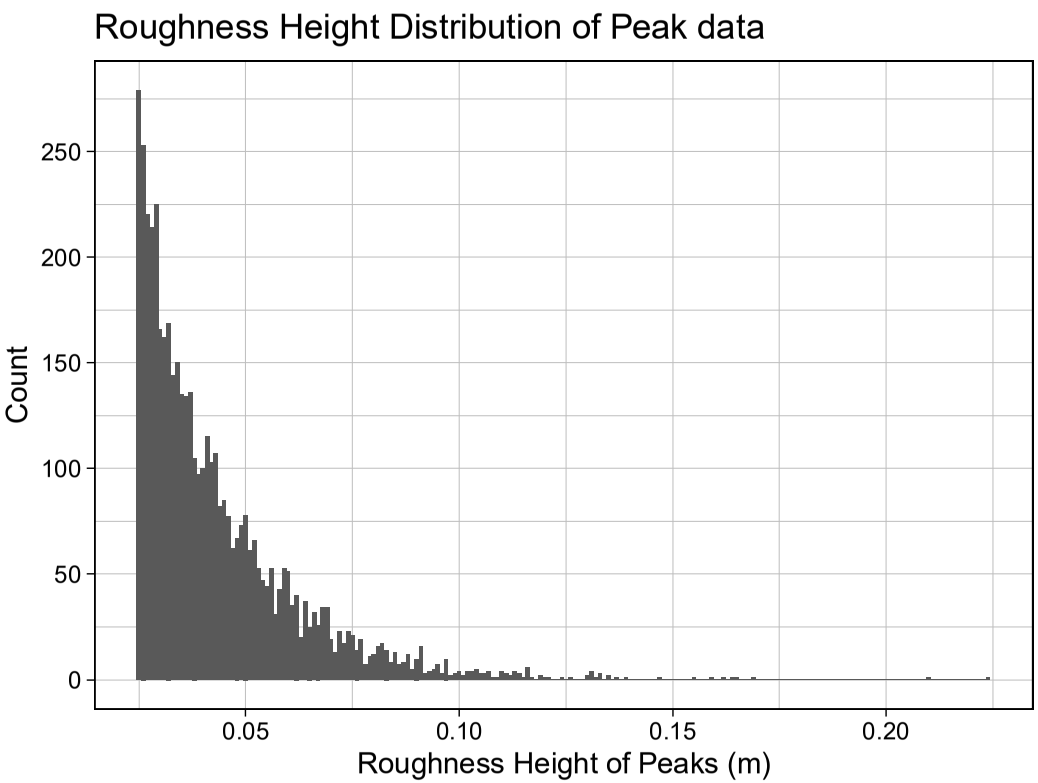

Representative RPA Photo of Surface Roughness

DRLL06 2018.11.21

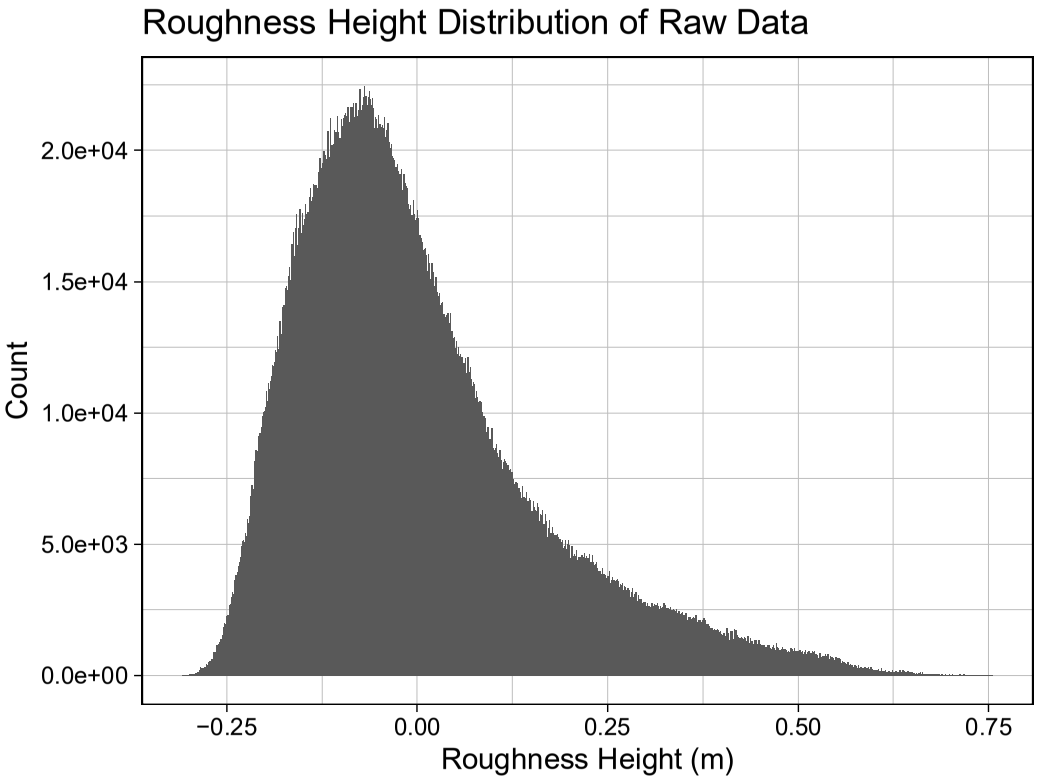

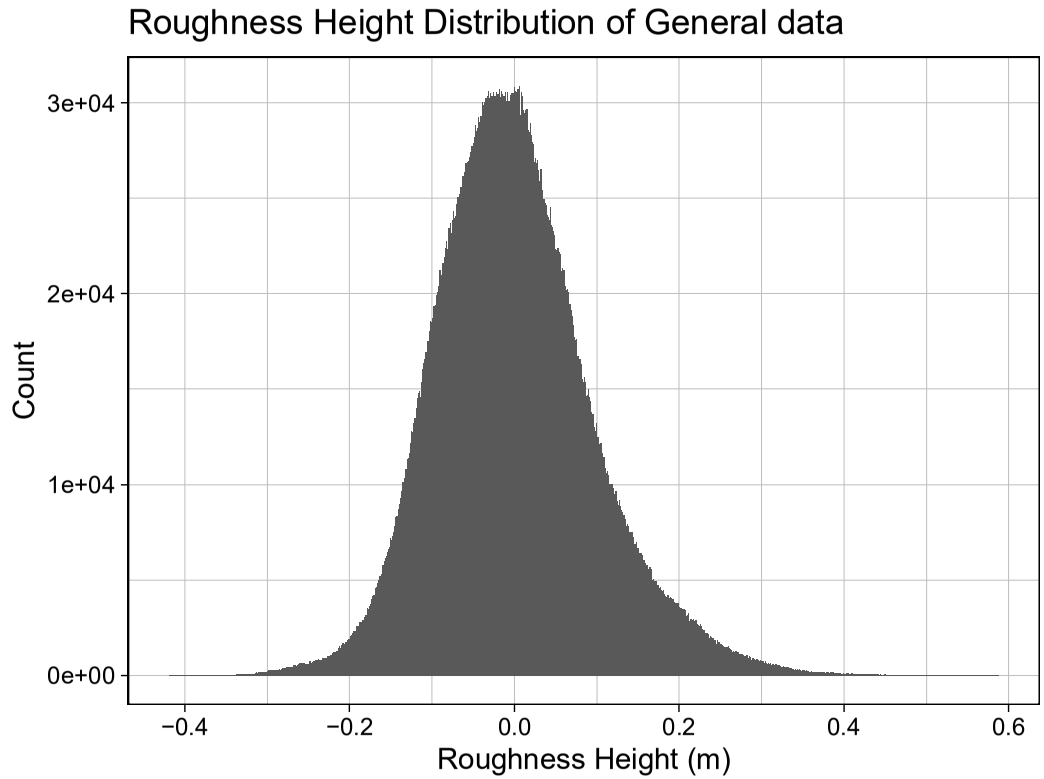

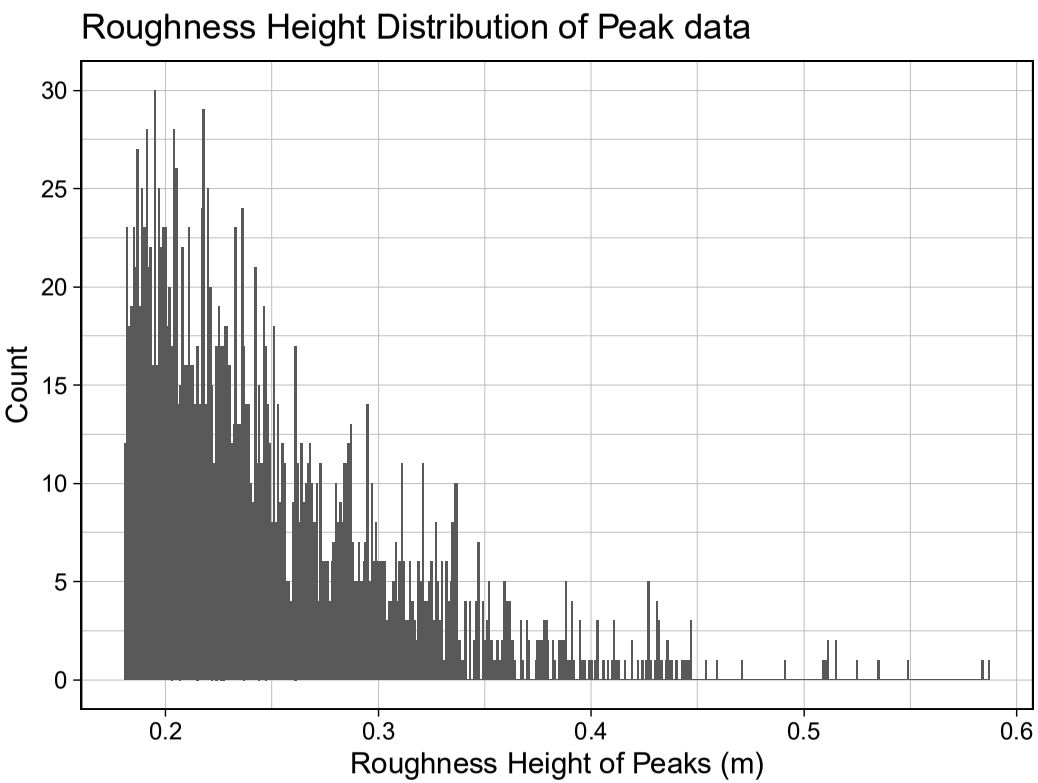

Representative RPA Photo of Surface Roughness

DRLL06 2019.02.20

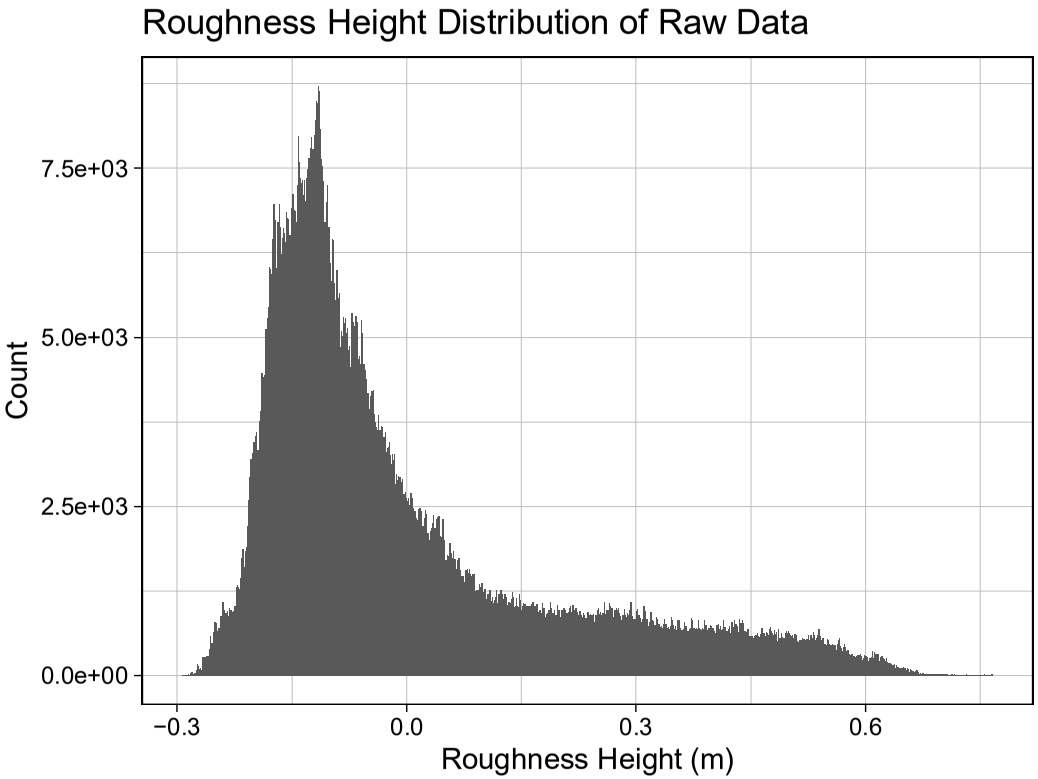

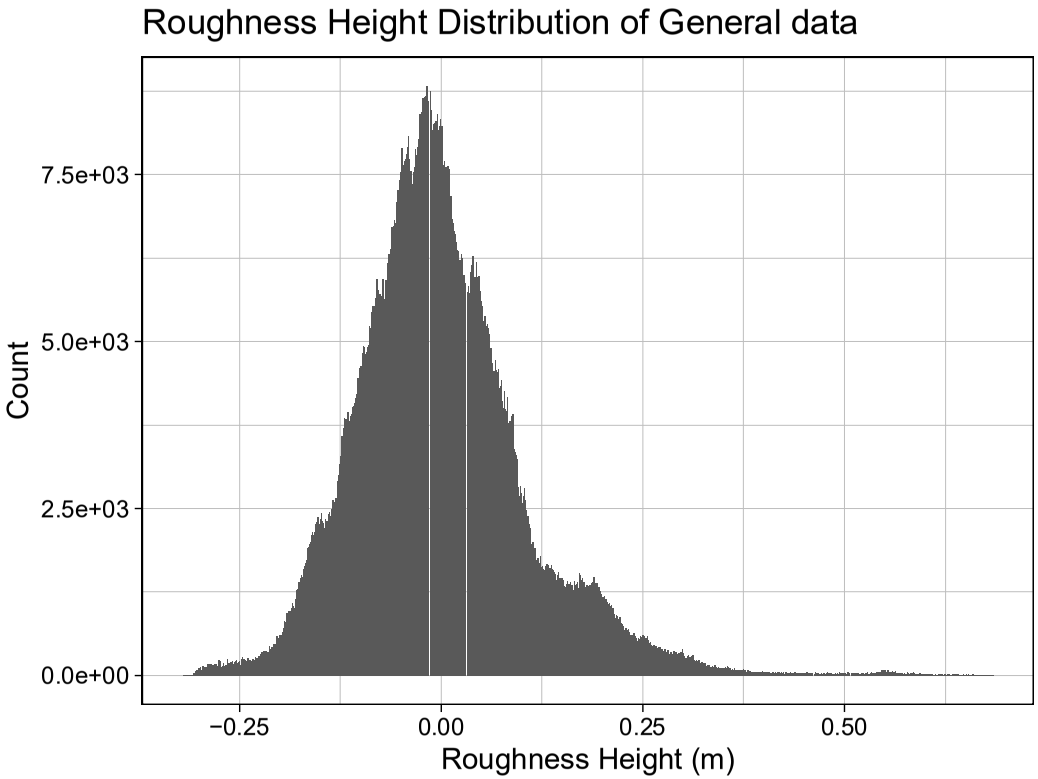

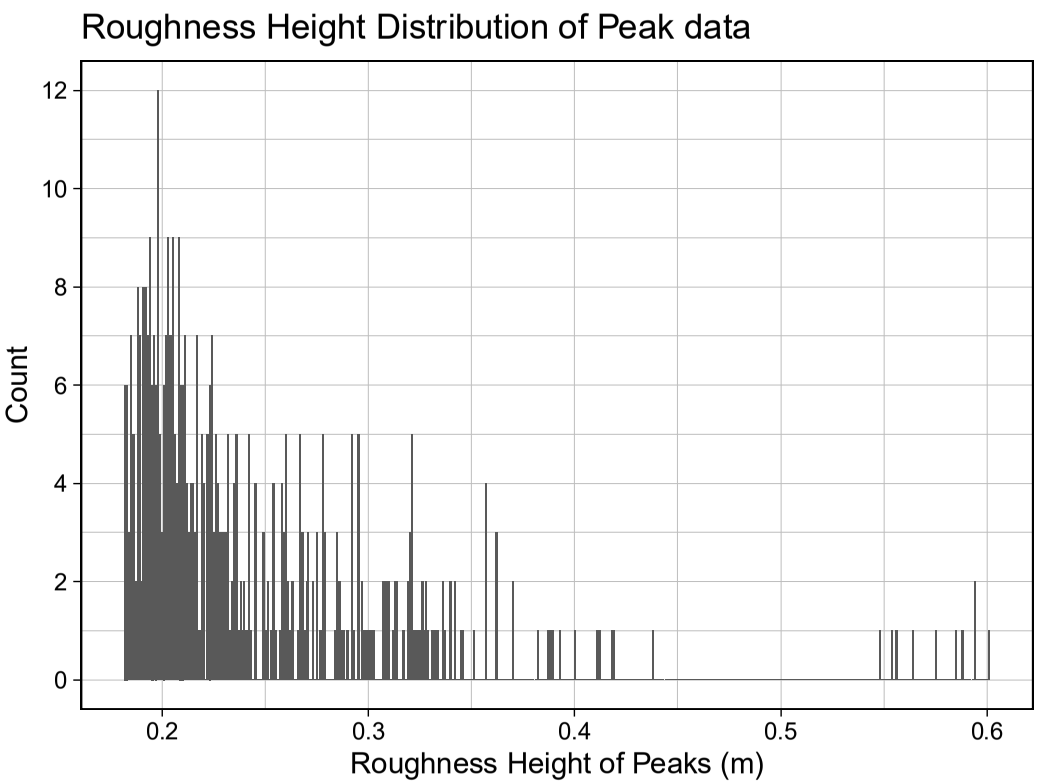

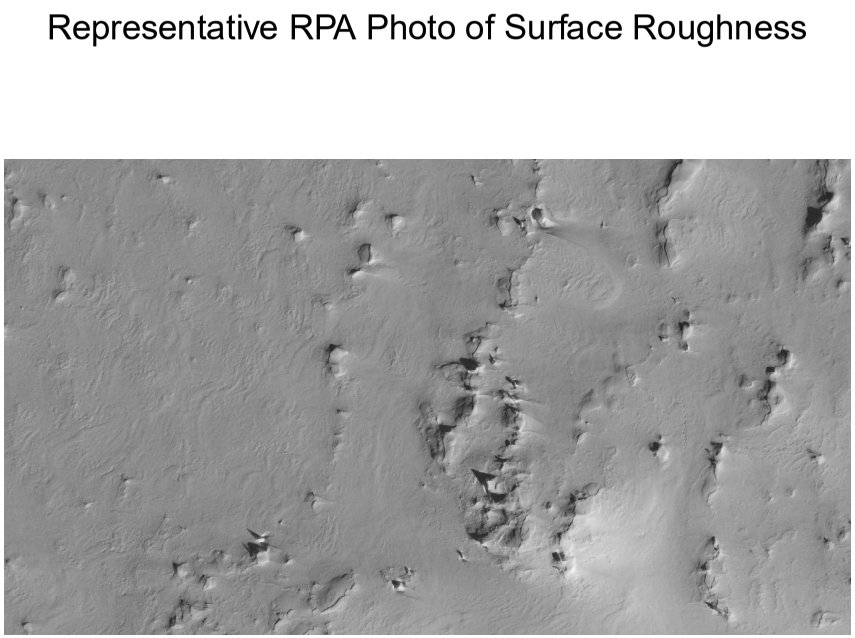

DRLL06 2019.11.12

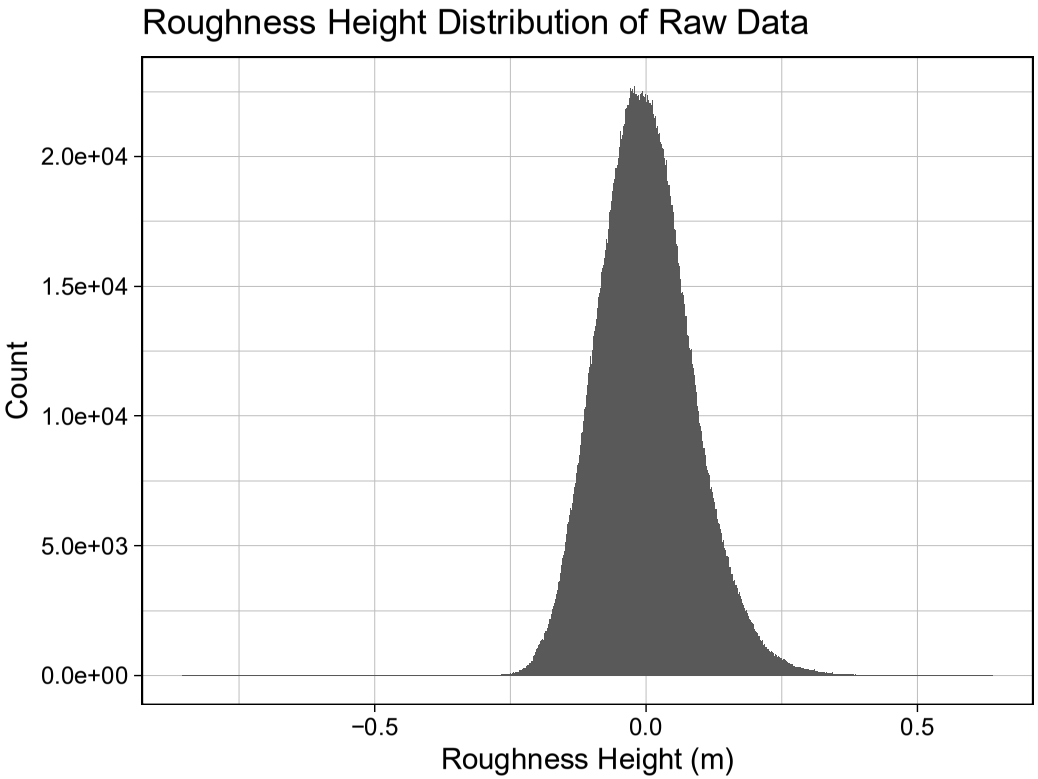

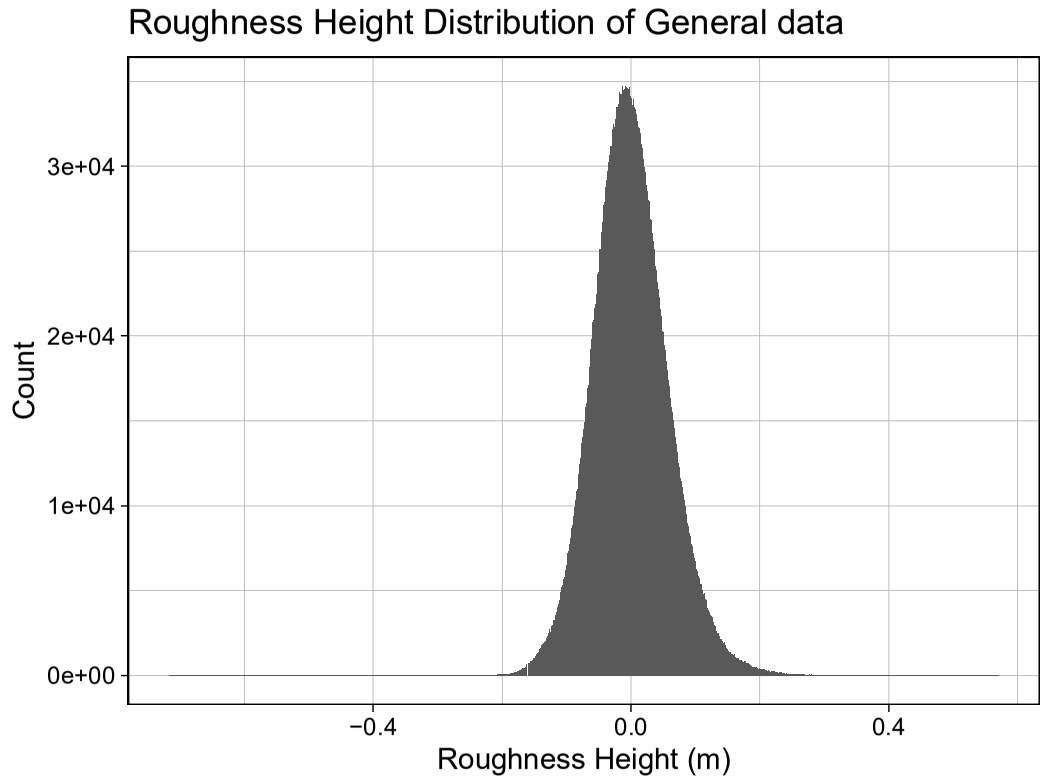

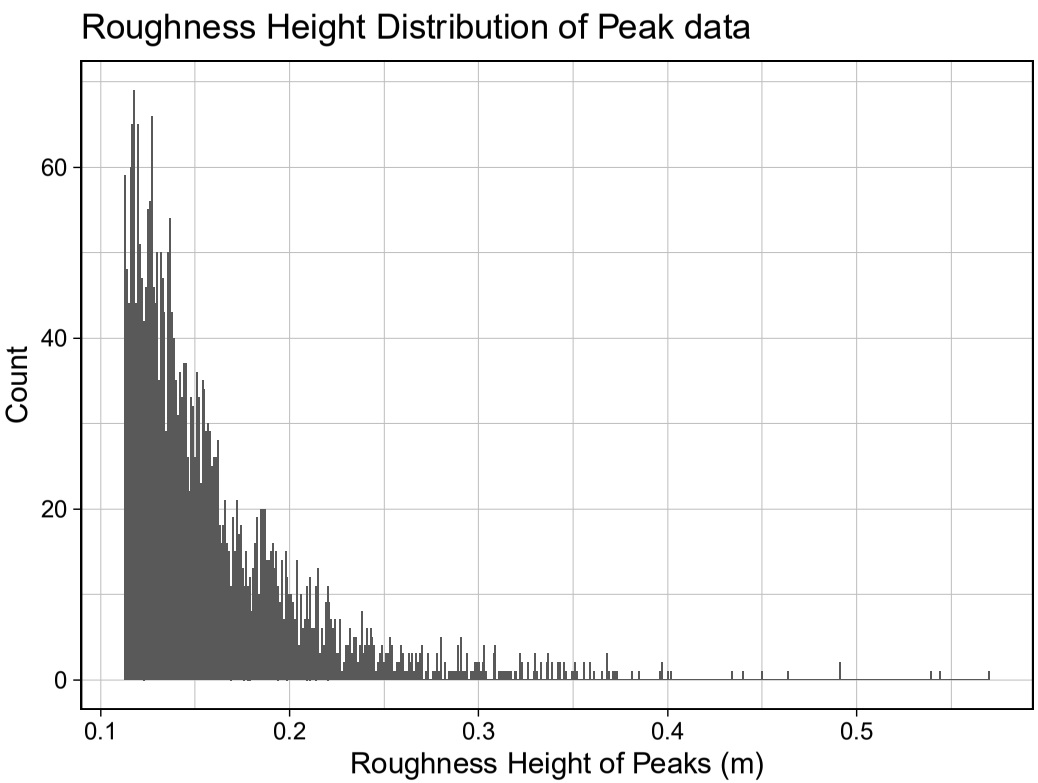

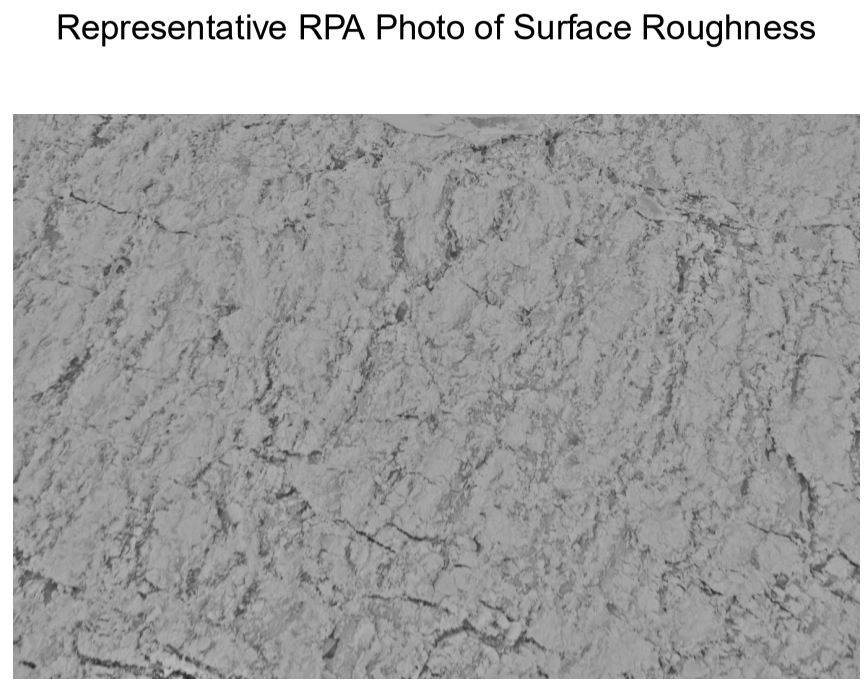

DRLL06 2019.11.13

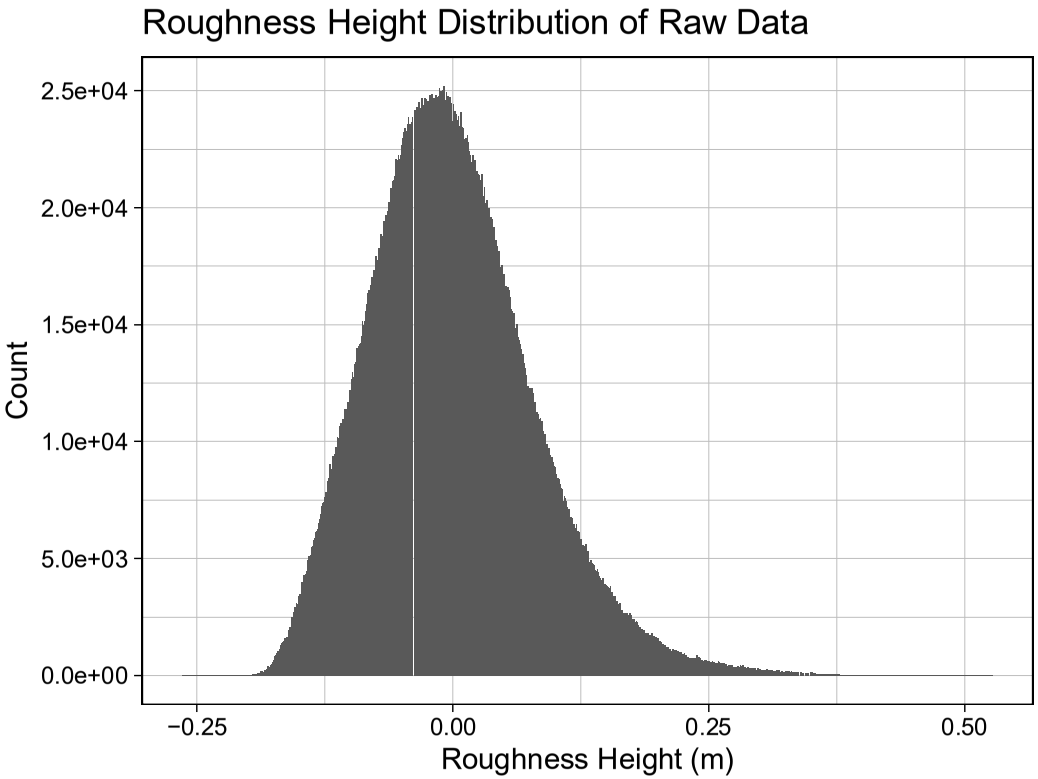

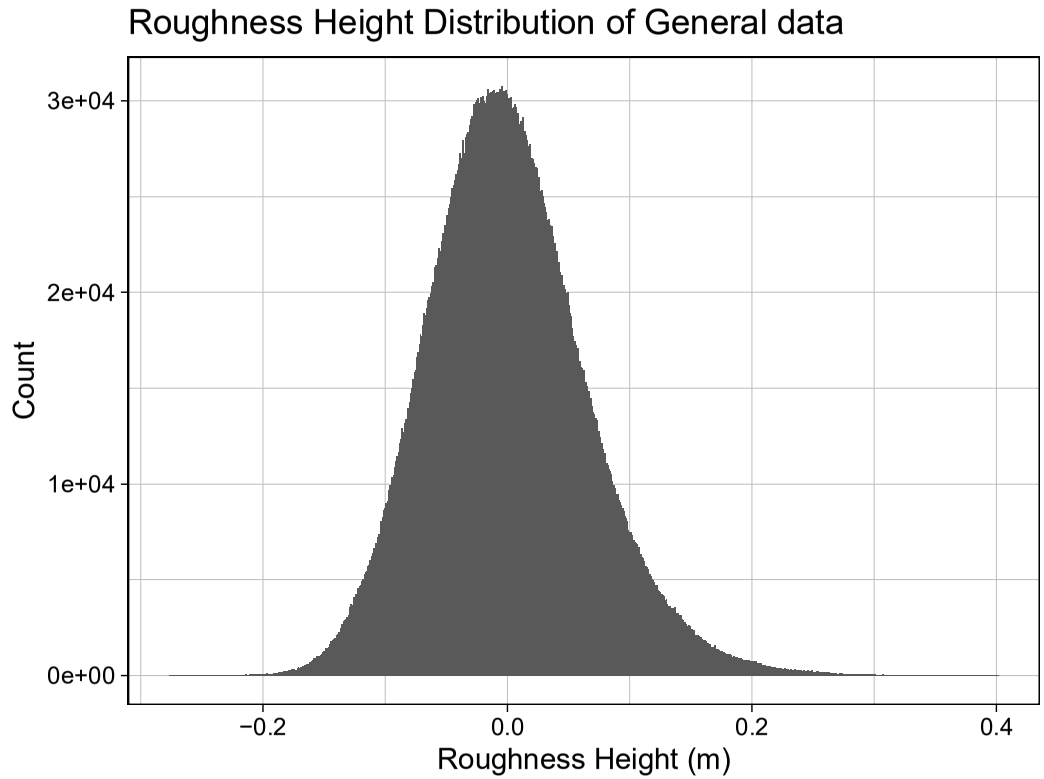

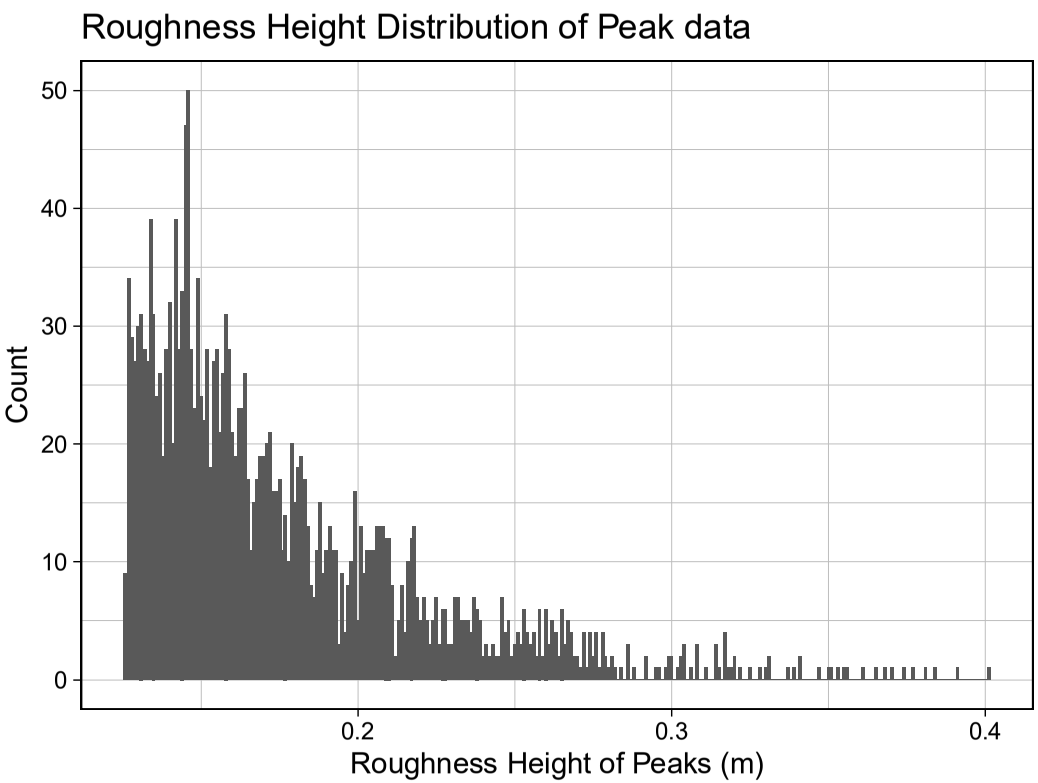

DRLL06 2019.11.26

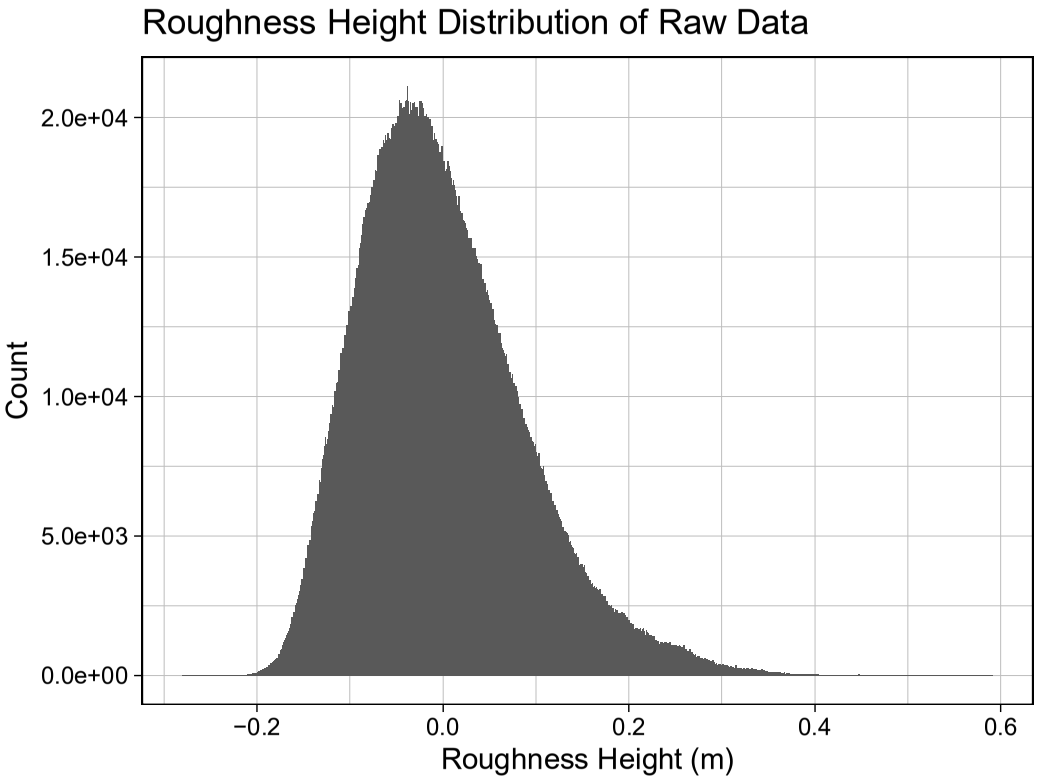

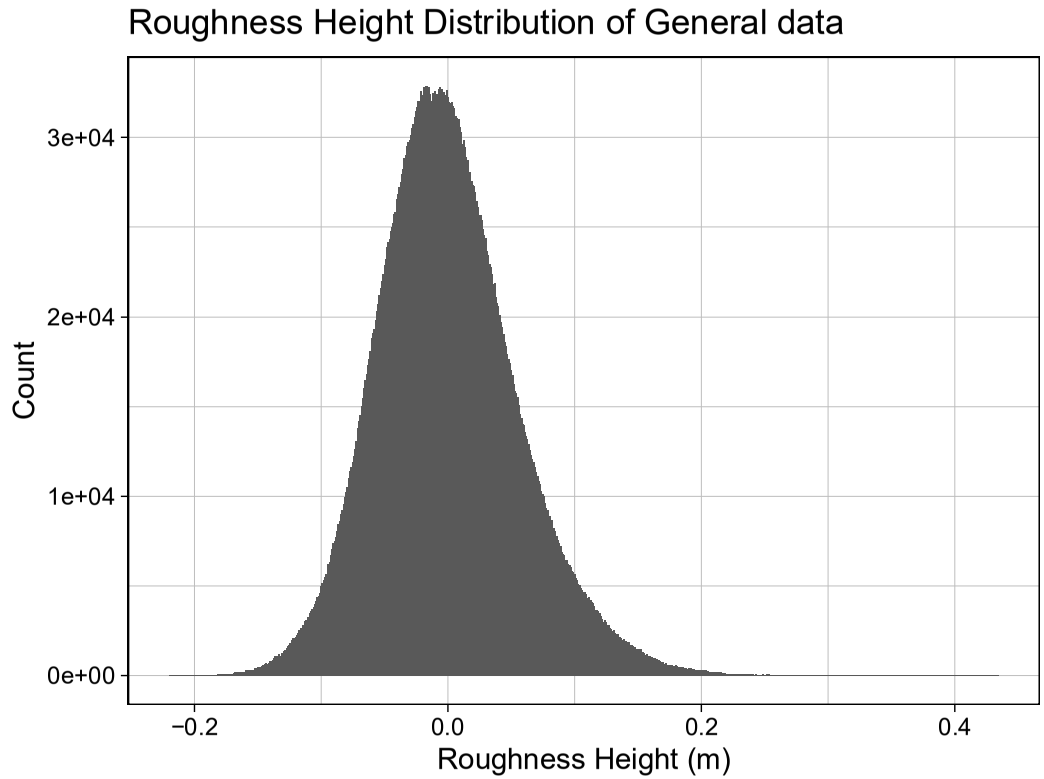

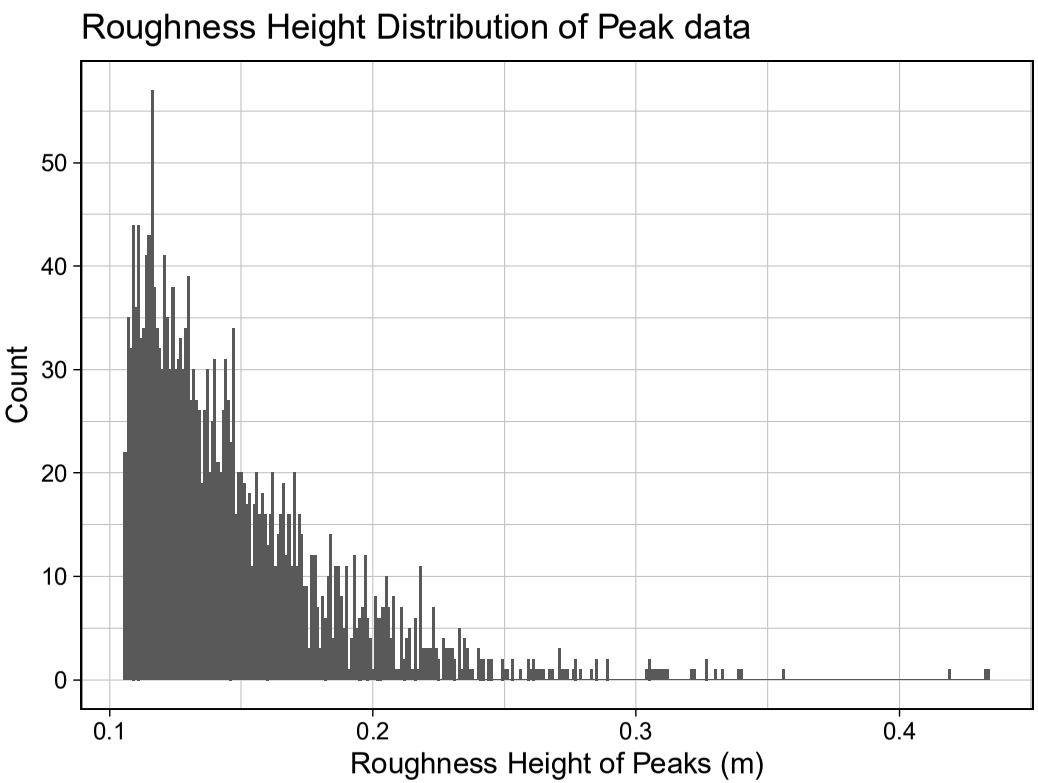

DRLL08 2019.11.13

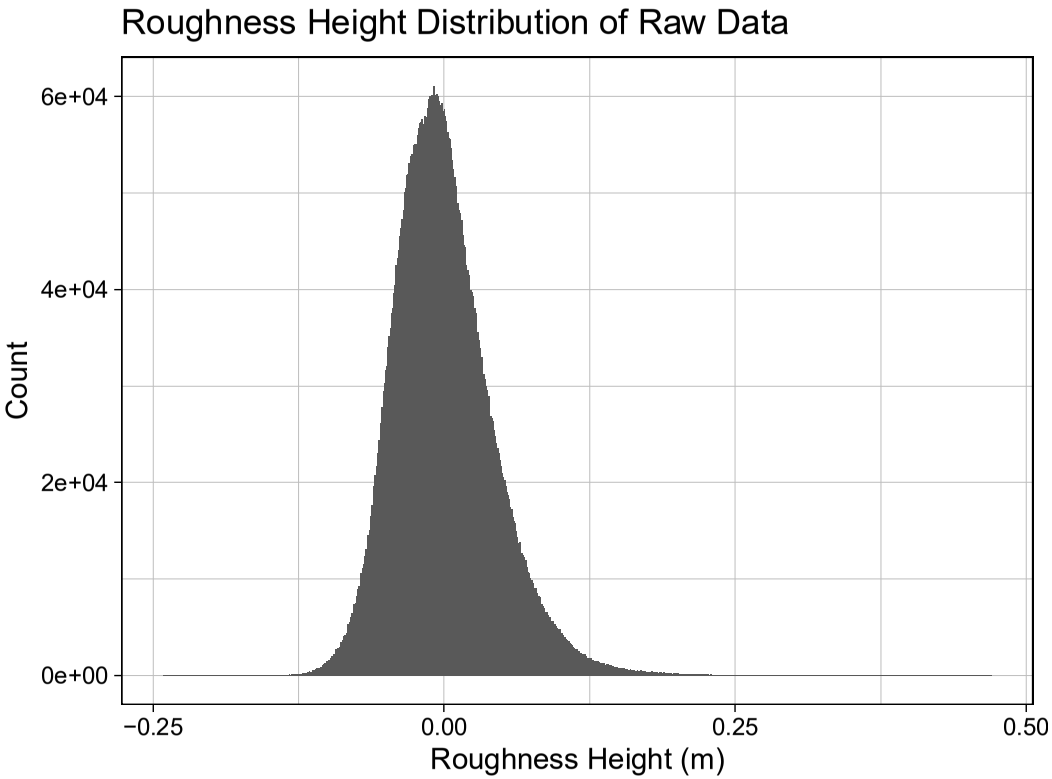

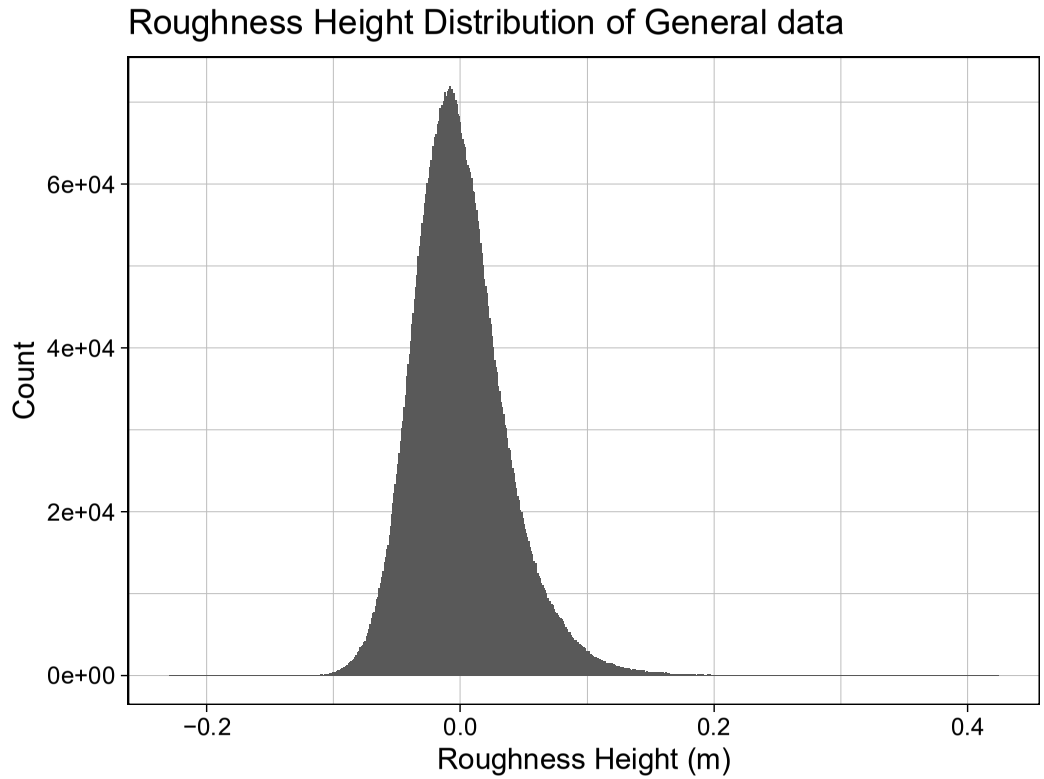

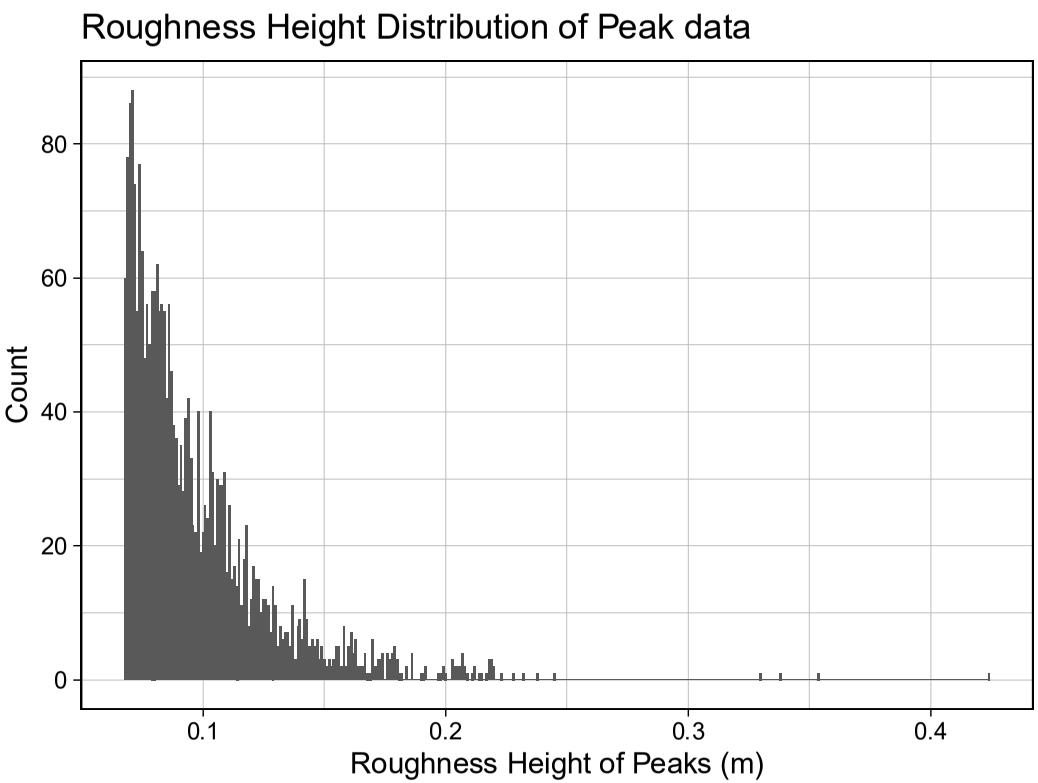

Representative RPA Photo of Surface Roughness

DRLL08a 2017.11.23

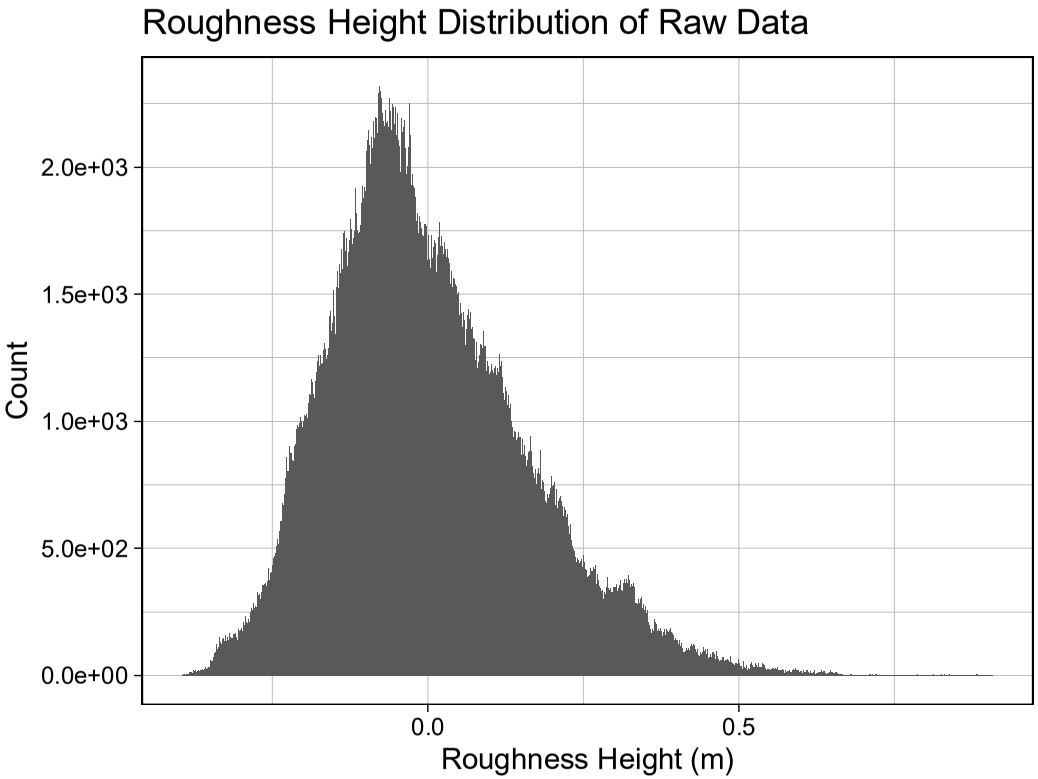

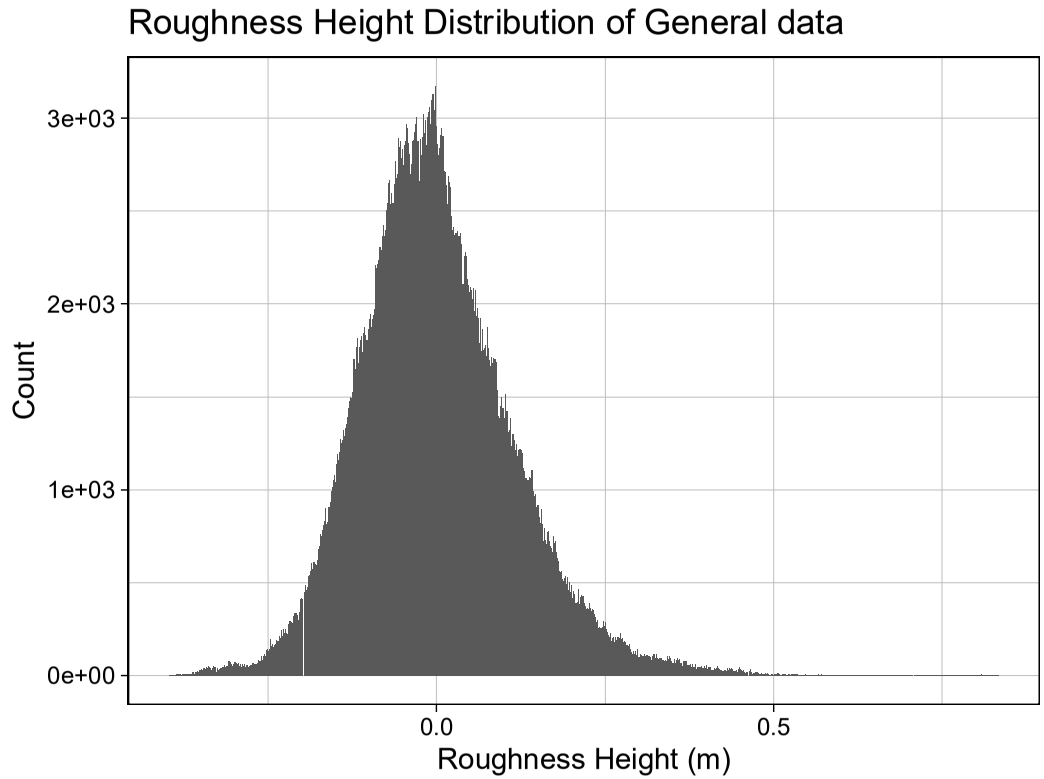

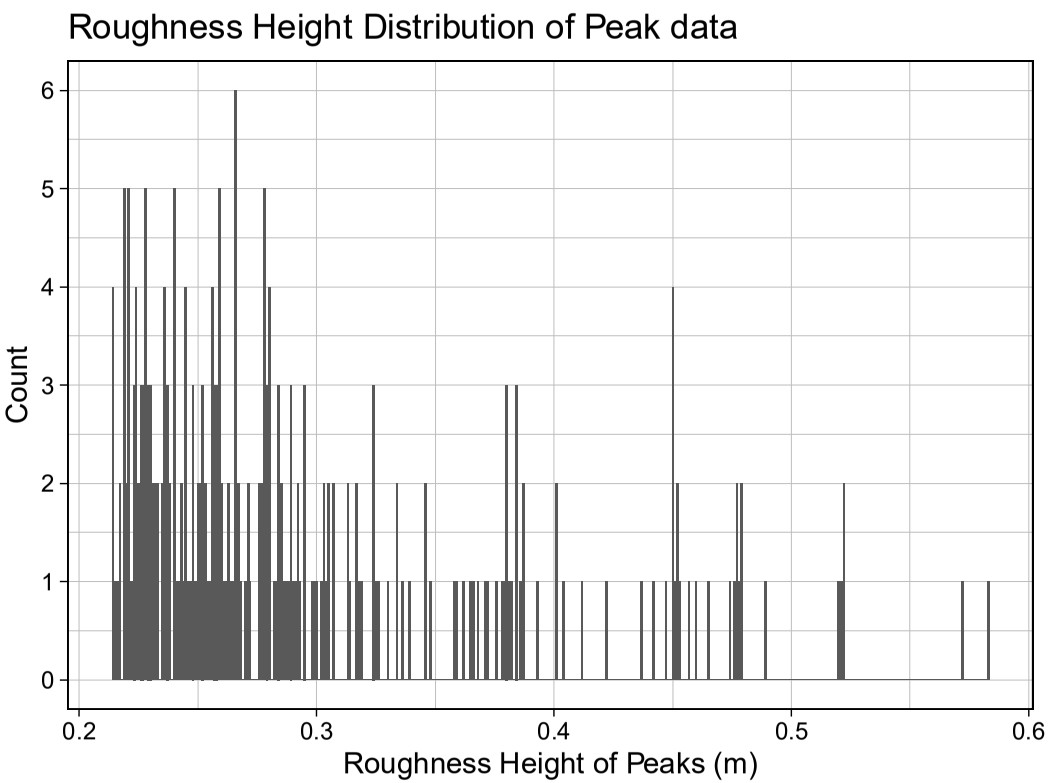

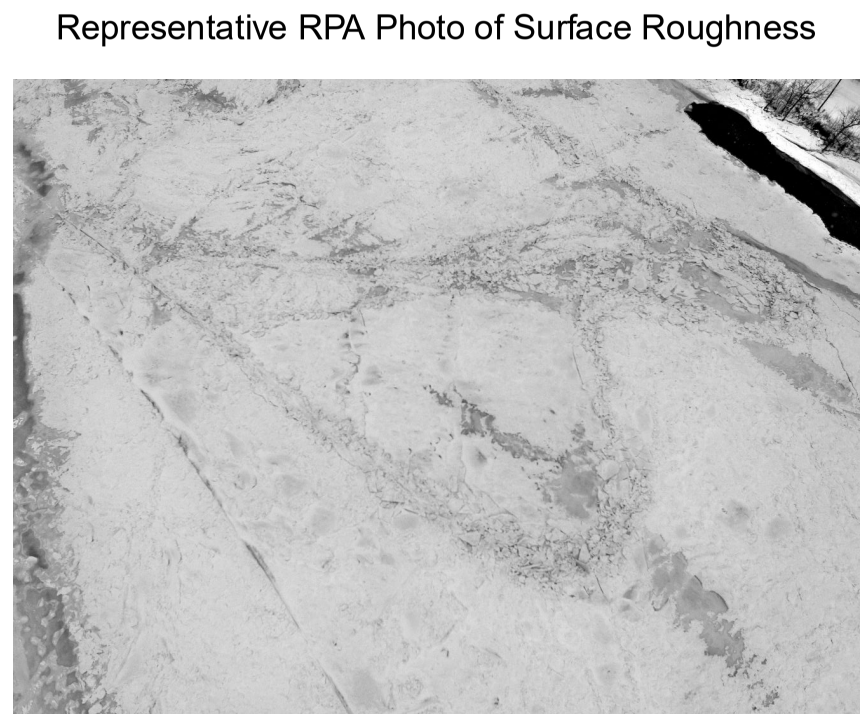

DRLL08a 2019.02.20

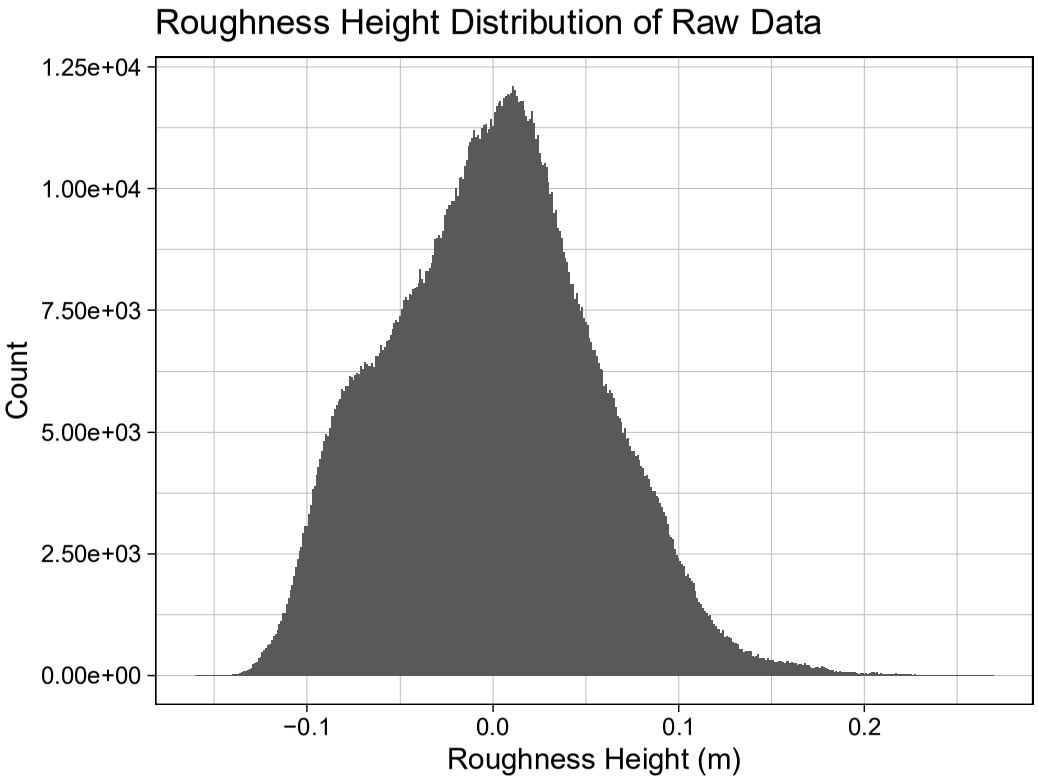

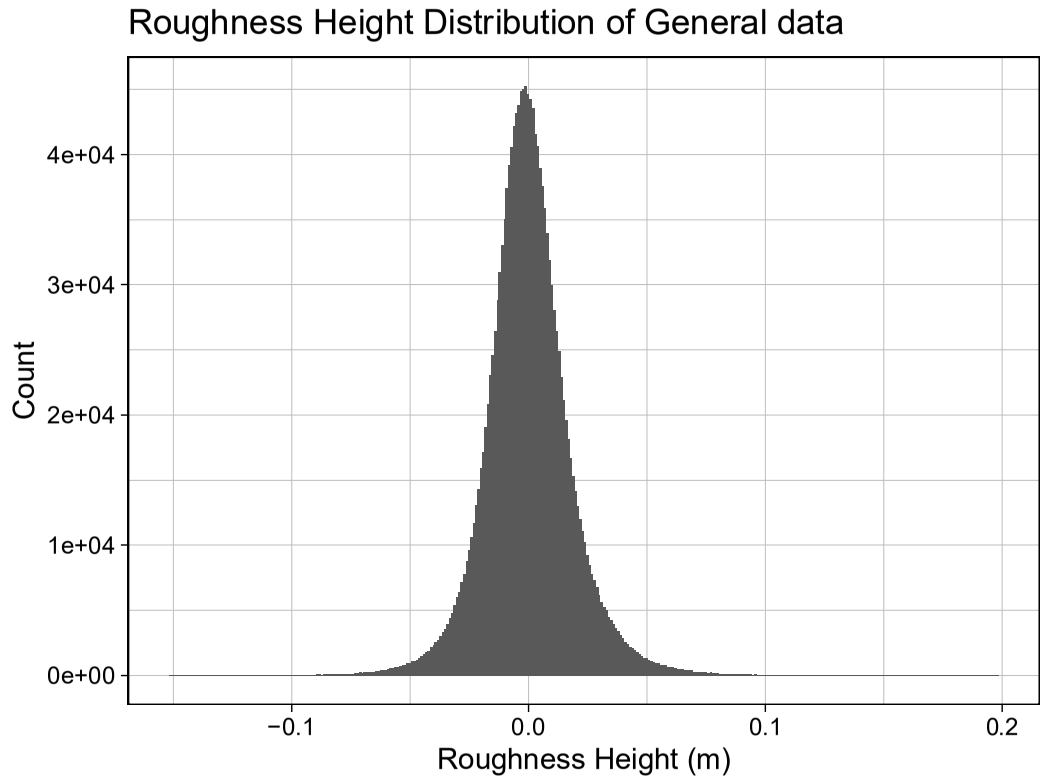

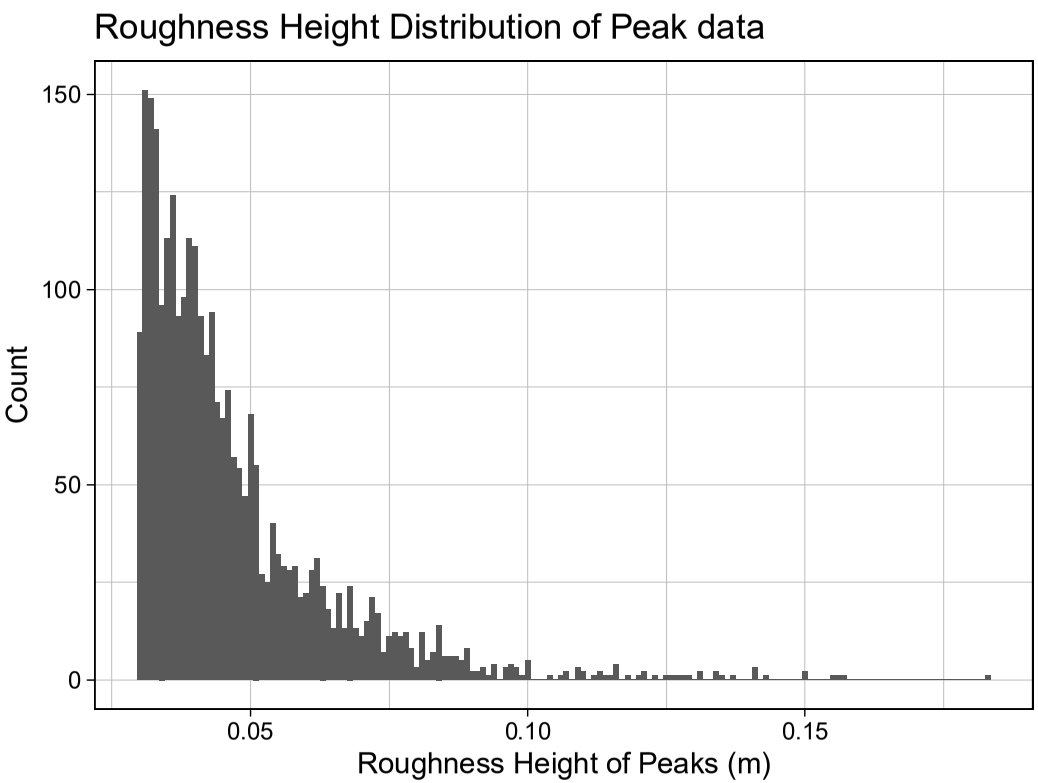

Representative RPA Photo of Surface Roughness

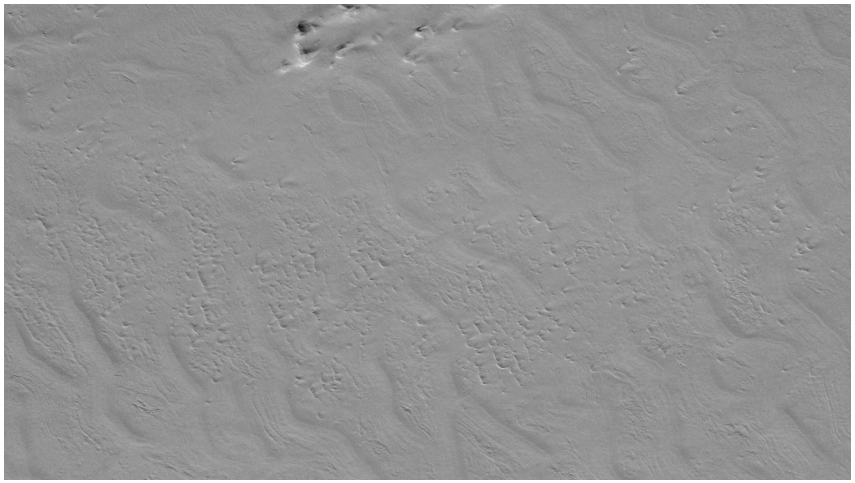

DRLL08a 2019.11.13

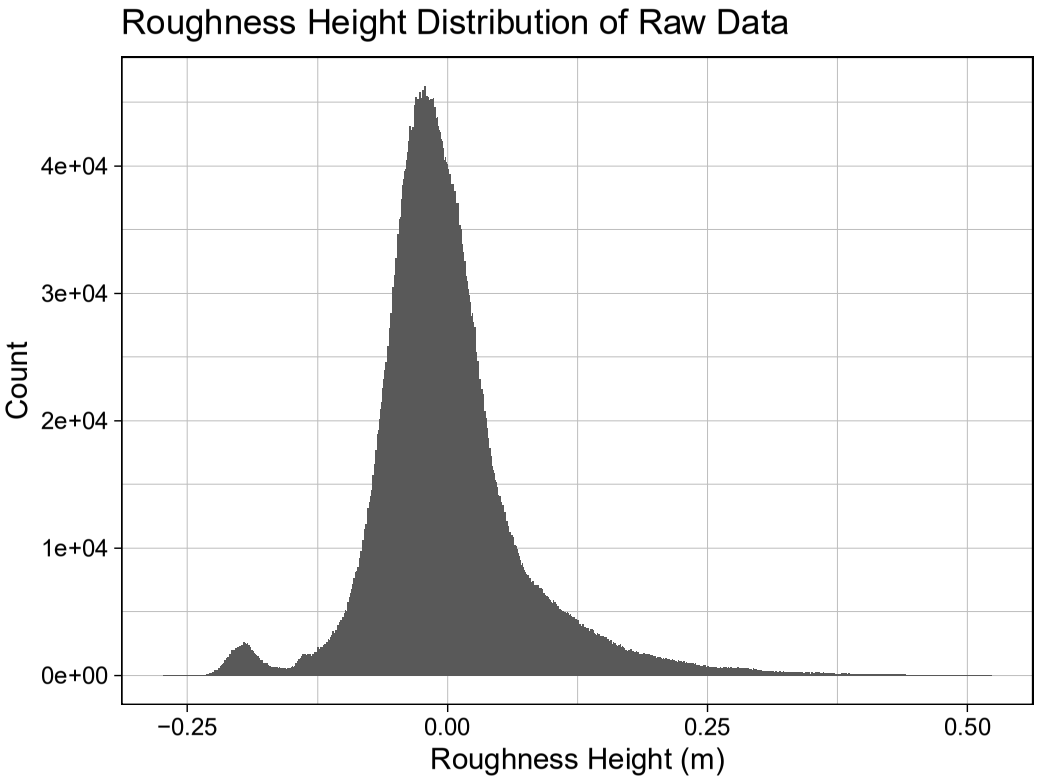

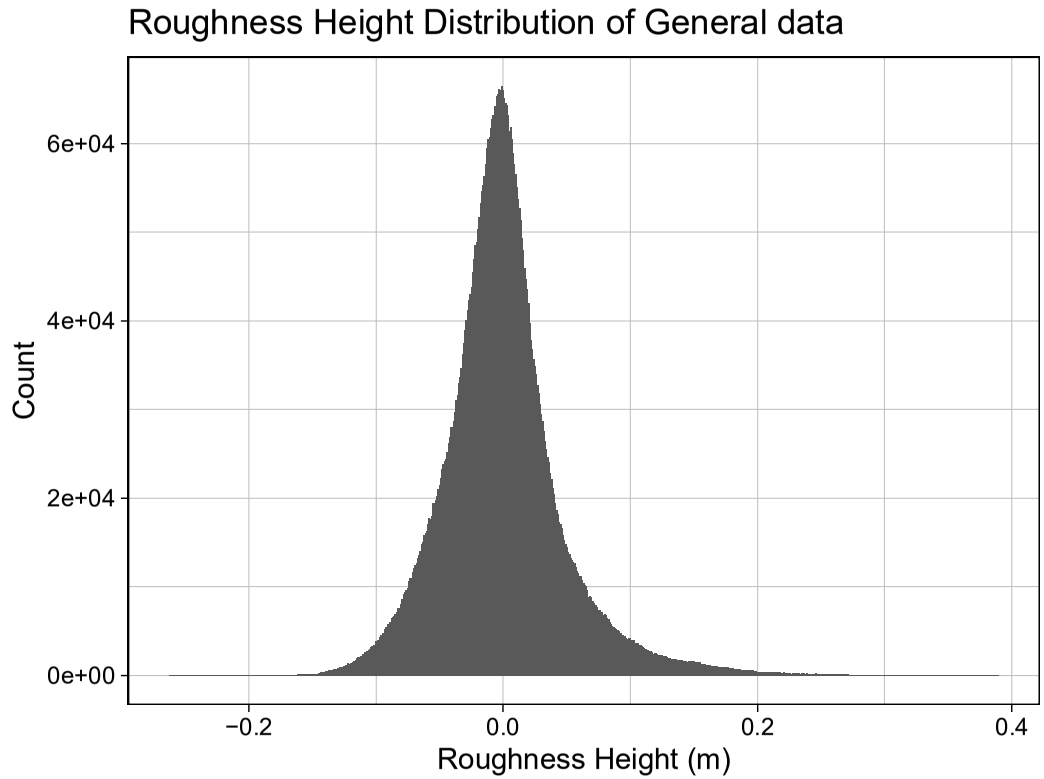

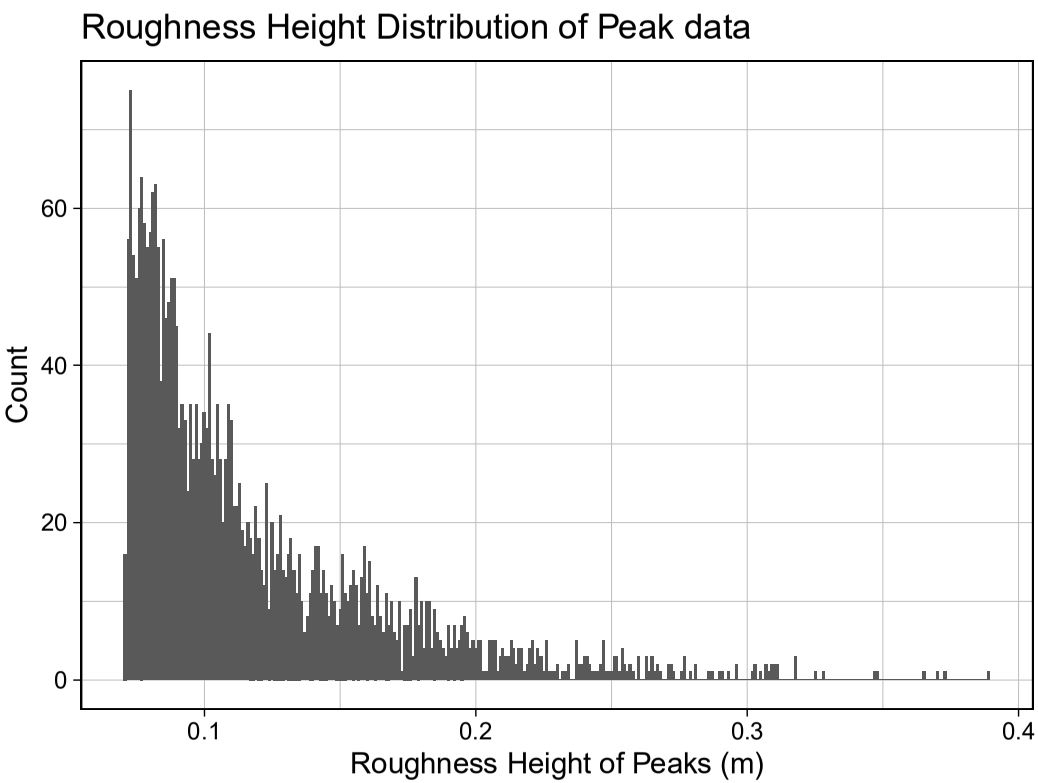

Representative RPA Photo of Surface Roughness

DRLL08a 2019.11.26